CdS Nanowires and CdSe/ZnS Quantum Dots Properties and Applications

BY

SHRIPRIYA PODURI
M.S. Electrical Engineering, University of Kentucky, Lexington, USA, 2010
B.E. Electronics, Electrical and Communications, Panjab University, India, 2008

THESIS

Submitted as partial fulfillment of the requirements
for the degree of Doctor of Philosophy in Electrical and Computer Engineering
in the Graduate College of the
University of Illinois at Chicago, 2015

Chicago, Illinois

Defense Committee:

Mitra Dutta, Chair and Advisor
Michael A. Stroscio
Danilo Erricolo
Junxia (Lucy) Shi
Alan Nicholls, Research Resources Center

This thesis is dedicated to my parents, Prof. P. Rama Rao and Mrs. P. Nalini and my sisters Aruna and Seetha.

ACKNOWLEDGEMENTS

No research is ever the outcome of individual's efforts. This work presented in the thesis would not have been possible without the helping hands of others.

First of all, I would like to thank my advisor, Prof. Mitra Dutta for giving me the opportunity and motivation to work with CdS nanowires and on the applications of CdSe/ZnS Quantum dots. I am very grateful to her for excellent guidance and support.

I am also thankful to Prof. Stroscio as he helped me and gave his excellent ideas about the experiments. I am very thankful to him for his guidance and ideas to do research. I would sincerely thank him a lot for his guidance and advice. I really appreciate and thank him for giving his time to hold technical discussions in his office and allowing me to work on detection of copper nanocavities.

I would also like to thank my committee Prof. Erricolo, Prof. Lucy Shi, Dr. Alan Nicholls, Prof. Stroscio and Prof. Mitra Dutta for serving their time to read my thesis.

I would take this opportunity to thank Dr. Seth Darling for motivating me and giving me the opportunity and guidance to work at Argonne National Laboratory and grow CdS nanowires at Argonne National Laboratory and has allowed me to work in Photovoltaics cells project using Block copolymer lithography and learnt a lot under his guidance. He also allowed me to work with AFM, SEM tools at Argonne that was very useful in my research. I am also thankful to Prof. Jimmy Xu at Brown University who allowed me to work in his lab to fabricate the AAO templates for a week. I am very thankful to his Postdoc Kin Jin Ho who gave me better fabrication tips for nanoporous templates and removal of barrier layer.

ACKNOWLEDGEMENTS (continued)

I also thank Dr. Ke-Bin Low, Dr. Alan Nicholls, Olivia and Kristina at the Research Resource Center at UIC, with whom I have collaborated so much and who was ever ready to help me in the data analysis with his expertise in Raman spectroscopy and SEM. I would also like to thank Nanotechnology staff Dr. An, Kasun Punchihewa and Khodr Mamaari for training me on some of the equipment and allowing me to use the equipment for my research.

I am very thankful to Dr. Suresh Rajaputra with whom I worked in University of Kentucky and he is the person who introduced me to the basic fabrication skills of developing nanoporous templates, many other deposition techniques and designing of experiments and research and has encouraged and motivated me to do PhD. I would also like to thank all my lab members especially Xenia, Robin, Min and Kimber who sometimes helped in some research experiments.

I would like to express my deepest thanks to Prof. Vijay Singh, my Master Thesis advisor for teaching me optoelectronics in Masters and allowing me to work in CENSE Laboratory where I worked with many fabrication skills.

This section would not be complete without acknowledging my parents and sisters. They have motivated and encouraged me throughout my life. Without their efforts, love and support this accomplishments wouldn't have been possible.

SP

TABLE OF CONTENTS

CHAPTER PAGE

1. INTRODUCTION 1
1.1 Introduction 1
1.2 Background on CdS nanostructure 4
1.2.1 Band structure of CdS material 5
1.2.2 Important parameters of CdS 6
1.3 Background on CdSe/ZnS Quantum Dots 7
1.4 Organization of Chapters 9

2. GROWTH OF CDS NANOWIRES 13
2.1 Introduction to the Fabrication of Nanowires 13
2.2 Growth of nanoporous templates 14
2.2.1 Experimental details of growth of anodized alumina template on ITO coated glass substrate 14
2.2.2 Experimental details of growth of nanoporous templates in aluminum sheet .. 15
2.3. Growth of Nanowires by DC electrodeposition 17
2.3.1 Experimental details for the growth of nanowires 17
2.3.2 Results and Discussion for the growth of nanowires 18
2.4 Growth of CdS nanowires using Vapor liquid Solid (VLS) Growth 19
2.4.1 Experimental Details for VLS growth of CdS nanowires 20
2.4.2 Results and Discussion of VLS growth of nanowires 21

3. PHOTOLUMINESCENCE CHARACTERIZATION OF CDS NANOWIRES 28
3.1 Introduction 28
3.2 The PL/Raman experimental set up 29
3.3 Photoluminescence of CdS nanowires grown using electrodeposition 30
3.3.1 PL of CdS nanowires grown on ITO coated glass substrate 30
3.3.2 Theoretical calculation of the nanowire diameter and depletion region width 32
3.4 PL characterization of the VLS grown CdS nanowires on ITO coated glass 35
3.5 Polarization studies of CdS nanowires 36
3.5.1 Introduction 36
3.5.2 Experimental Set up 38
3.5.3 Polarization experiment results 38

4. RAMAN SPECTRAL STUDIES OF CDS NANOWIRES 45
4.1 Introduction to Raman spectroscopy 46
4.2 Raman spectral studies of CdS nanowires grown using electrodeposition on ITO coated glass substrate 48
4.3 Raman scattering in CdS nanowires grown using electrodeposition in anodized aluminum sheet 49
4.4 Raman scattering in CdS nanowires grown via VLS growth and its comparison with electrodeposited growth of CdS nanowires 50

TABLE OF CONTENTS (continued)

4.5 Raman characteristics of CdS nanowire array grown in anodized alumina sheet in different orientations and polarizations 50
4.6 Exciton longitudinal optical (LO) phonon interaction in CdS nanowires 52

5. INVESTIGATION OF CDS/P3HT HETEROJUNCTION 64
5.1 Introduction 64
5.2 Experimental Details 65
5.3 Photoluminescence and Current Voltage Characterization of CdS/P3HT 66

6. USES OF CDSE/ZNS QUANTUM DOTS 73
6.1 Introduction 73
6.2 Experimental details 74
6.3 Results and Discussion 75
6.3.1 Carboxyl functionalized QDs on copper surface 75
6.3.2 Amine QDs on copper nanocavities 77
6.4 Partial anodization of copper surface with a mask 78

7. CONCLUSION AND FUTURE WORK 87
7.1 Conclusion 87
7.2 Future work 90

CITED LITERATURE 92

APPENDICES 100
APPENDIX A 101
APPENDIX B 104
APPENDIX C 106

VITA 112

LIST OF TABLES

TABLE PAGE

I: IMPORTANT PARAMETERS OF CDS. 7

II: OPTICAL PHONON MODES OF WURTZITE CDS CRYSTAL. ALL THE MODES ARE EXPRESSED IN CM^{-1}. 52

III: HUANG RHYS FACTOR VALUES COMPUTED FROM EXPERIMENTAL DATA GIVEN IN FIGURE 34. 56

LIST OF FIGURES

FIGURE PAGE

1. E-k plot illustrating a) direct band gap semiconductor undergoing photon absorption b) Indirect band gap semiconductor undergoing photon absorption c) Indirect band gap semiconductor undergoing photon absorption assisted with phonon emission. 11

2. Wurtzite unit cell lattice of CdS crystal.. 11

3. Electronic band structure of CdS. 12

4. Types of configurations of core shell QDs. 12

5. Steps involved in the anodization of aluminum. 21

6. SEM micrographs of the anodized alumina templates after the removal of barrier layer grown at (a) & (b) Brown university in 500 µm aluminum sheet, (c) & (d) UIC in 200-250 nm aluminum deposited on ITO coated glass substrate. 22

7. Flowchart for the fabrication of CdS nanowires (a) 200 nm of aluminum layer (yellow) deposited on ITO coated glass substrate (b) After anodization of Al layer leading to formation of nanopores of 10 -60 nm. (c) CdS nanowire array after the DC electrodeposition growth. 23

8. (a) top view (b) side view SEM micrograph of CdS nanowires of 30- 60 nm in diameter after annealing. 24

9. (a) top view (b) side view SEM micrograph of CdS nanowires grown in anodized aluminum oxide sheet. 24

10. EDS of the CdS nanowires grown on ITO coated glass substrate by electrodeposition... 25

11. EDS Spectra of CdS nanowires grown in anodized alumina metal sheet of 500 µm. 25

12. VLS growth mechanism. 26

13. SEM images after the VLS growth of CdS nanowires. 26

14. EDS result for VLS grown CdS nanowires. 27

15. Schematic explaining PL process. 40

LIST OF FIGURES (continued)

16. PL spectra of (a) as grown and (b) annealed CdS nanowires with peak at 506 nm (2.44 eV) and 514 nm (2.41 eV), respectively. 40

17. (a) PL spectra of CdS nanowires with different laser excitation power using neutral density filters before annealing (b) PL intensity area variation vs. different laser excitation power using neutral density filters before annealing. 41

18. (a) PL spectra of CdS nanowires with different laser excitation power using neutral density filters after annealing (b) PL intensity area variation vs. different laser excitation power using neutral density filters after annealing. 41

19. (a) Cross section of nanowire (b) band diagram of CdS nanowire with depletion region of width w due to surface states. 42

20. PL spectra of VLS grown nanowires on ITO coated glass substrate at room temperature. 42

21. Parallel and perpendicular polarization with light propagating parallel to the nanowire axis. 43

22. Parallel and perpendicular polarization with light propagating perpendicular to the nanowire axis. 43

23. (a) PL peak intensity variation measured when light is propagating along Z but perpendicular to the length of the nanowire. (b) PL peak intensity variation measured when light is propagating along the length of the nanowire along Z. The measured PL ratio is 0.80. 44

24. Types of Raman scattering. 57

25. Raman peaks observed at 302, 603, 906 cm^{-1} corresponding to 1 LO, 2 LO and 3 LO respectively of CdS nanowires grown in AAO templates fabricated on ITO coated glass substrate. 57

26. Raman peaks observed at 305, 606, 909 cm^{-1} corresponding to 1 LO, 2 LO and 3 LO of CdS nanowires respectively grown in anodized alumina sheet. 58

27. Raman spectra of VLS grown CdS nanowires with peaks at 302 cm^{-1}, 603 cm^{-1} and 906 cm^{-1} corresponding to the longitudinal optical phonon (LO) modes 1 LO, 2 LO and 3 LO, respectively. 58

28. Comparison of Raman spectra of VLS grown and electrodeposited growth of CdS nanowires. 59

LIST OF FIGURES (continued)

29. Raman using the polarization filter with peak at A1 (TO) at 235 cm^{-1} for parallel polarization in (a) and at E2 at 258 cm^{-1} for perpendicular polarization in (b) along with 1 LO, 2 LO at 309 and 607 cm^{-1} respectively when light is propagating along the length of the wire along Z. 60

30. Raman using the polarization filter with peak at E1 (transverse) at 247 cm^{-1} for parallel polarization in (a) and at quasi A1 (transverse) at 240 cm^{-1} for perpendicular polarization in (b) along with 1 LO, 2 LO at 309 and 607 cm^{-1} respectively when light is propagating along Z but perpendicular to the length of the wire.....60

31. Plot of electron phonon coupling constant for CdS nanowires for different laser polarization angles $\boldsymbol{\theta}$ against wavenumber. Highlighted regions (a) and (b) are zoomed out in Figures 32 and 33 respectively as shown below. 61

32. Zoomed version of highlighted region (b) of Figure 31 shows the minima at 233 and 243 cm^{-1}. 62

33. Zoomed version of highlighted region (b) of Figure 31 shows the magnitudes of electron coupling constant decreasing with increasing angle $\boldsymbol{\theta}$.....62

34. Experimental data of Raman spectrum with different angles. $\boldsymbol{\theta}$ denotes the angle between the long axis of nanowire (z axis) and the laser polarization. 63

35. Monomer unit of conductive polymer P3HT.....69

36. HOMO and LUMO level of P3HT along with E_c and E_v level of CdS. 69

37. (a) Before contact, energy levels expressed with respect to E_{vac}. (b) Band diagram of CdS/P3HT heterojunction……70

38. (a) PL spectrum of P3HT solution with peak at 650 nm (b) PL spectra of CdS/P3HT heterojunction with CdS peak at 510 nm and P3HT peak at 650 nm.....71

39. (a) I-V curve of CdS/P3HT. (b) Schematic of CdS/P3HT measurement circuit. 71

40. (a) Comparison of simulated and experimental I-V curve, (b) Region I zoomed to show the experimental current value.....72

41. (a) 5 minute anodization, sample A (b) 10 minute anodization, sample B (c) 15 minute anodization, sample C (d) 20 minute anodization time, sample D. 79

LIST OF FIGURES (continued)

42. (Clockwise from left): (a) White light image of 2 mm drop of 650 NC QDs under 4X Magnification. (b) Red fluorescence image of the same area under 4X magnification with 655 nm filter. (c) 50 X magnification of the same area in red fluorescence using 655 nm filter. (d) 50 X magnification of the same area in white light. 80

43. 50 X magnification image after the fourth wash with DI water (a) under white light (b) red fluorescence under 655 nm filter. 81

44. AFM micrograph of the copper surface with the QDs on it. 81

45. 4X magnification image of the Kimwipe (a) under white light (b) red fluorescence with 655 nm filter. 82

46. 50 X magnification image after heating the copper surface (a) under white light (b) red fluorescence under 655 nm filter. 82

47. (a) White light image of anodized copper surface with drop cast amine functionalized CdSe/ZnS QDs after washing four times. b) Red fluorescence image of the same area under 50X magnification with 655 nm filter. Positively charged amino QDs were not seen under fluorescence microscope, therefore these QDs did not bind to the anodic like nanopores of copper surface (c) 50 X magnification image of carboxyl functionalized binding after the fourth wash with DI water under white light (d) red fluorescence under 655 nm filter. 83

48. (a) SEM image showing both the regions where the right side region of the sample which was anodized and left hand side region of the sample was masked with scotch tape and was not anodized. (b) Higher magnification of unanodized left side region image where we could see only the copper surface without pores since it was not anodized. (c) SEM image showing the right region of anodized area of copper. 84

49. Left hand side region of sample was anodized for 5 minutes and right hand side region of the sample was masked with scotch tape resulting in 20 nm pores as seen in sample A. Quantum dots were observed only in nanoporous side.....85

50. Left hand side region of the sample was anodized for 10 minutes and right hand side region of the sample was masked with scotch tape resulting in 40 nm pores as seen in sample B. Quantum dots were observed only in nanoporous side. 85

LIST OF FIGURES (continued)

51. Left hand side is anodized for 15 minutes and right hand side of the sample was masked with scotch tape resulting in 100 nm pores as seen in sample C. Quantum dots were observed only in nanoporous side. 86

52. Left hand side region of the sample was anodized for 20 minutes and right hand side region of the sample was masked with scotch tape resulting in 400 nm pores as seen in sample D. Quantum dots were observed only in nanoporous side. 86

LIST OF ABBREVIATIONS

CdS NWs	Cadmium sulphide Nanowires
CdSe/ZnS	Cadmium selenide/Zinc sulphide
AAO	Anodized Aluminum Oxide (AAO)
QDs	Quantum Dots.
NW	Nanowire
CB	Conduction Band
VB	Valence Band
1D	1-Diemnsional
VLS	Vapor Liquid Solid
PL	Photoluminescence
sccm	Standard Cubic Centimeter per minute
SEM	Scanning Electron Microscope
EDS	Energy Dispersive Spectroscopy
HeCd	Helium Cadmium
Ar^+	Argon Ion
UV	Ultraviolet
IPA	Isopropyl Alcohol
CCD	Charge Coupled Detector
P3HT	Poly (3-hexylthiophene-2, 5-diyl)
IR	Infrared
I-V	Current-Voltage
DI water	Deionized water
NaOH	Sodium Hydroxide

SUMMARY

With the increase in demand for nanoscale devices and rapid development of semiconductor devices, nanostructures such as nanowires (NWs) and quantum dots (QDs) can be used in future applications. These may include a wide range of optoelectronic applications such as photo-detectors, sensors, lasers, transistors and optical switches, etc. Recent research in the field of semiconductor nanowires has revealed lot of interesting properties such as polarization anisotropy, and size-dependent photoluminescence, among others. Optimization of these properties to improve the efficiency of these devices is necessary. Cadmium sulphide (CdS) is a II-IV direct band gap semiconductor which is well suited for many optoelectronic devices such as solar cells, optical switches, photodetectors and polarizers. In this thesis, CdS nanowires were grown and their properties were characterized for its possible use in optoelectronic applications. Another interesting nanostructure is Cadmium selenide/Zinc sulphide (CdSe/ZnS) core shell quantum dots (QDs) which can be used for detection purposes due to its unique surface chemistry, broadly tunable excitation and emission properties. In this thesis, we have optimized these properties of nanowires for its possible use in optoelectronic applications. Also, emission properties QDs were used to detect the nanocavities on copper surfaces.

Template having periodic arrays of nanoporous structure to grow nanowires of high aspect ratio was fabricated. One such template having nanoporous structure is anodic aluminum oxide (AAO) template is suitable for growing nanowires by electrochemical deposition since this nanoporous structure is uniform and has vertically directed grown nanopores. Cadmium sulphide (CdS) was selected because it’s a direct

band gap semiconductor and is suitable for optoelectronic applications. CdS nanowires were grown using DC electrodeposition method and vapor liquid solid growth for their comparison. Two substrates were used to grow CdS nanowires via DC electrodeposition. One of the substrate was Indium Tin Oxide (ITO) coated glass substrate and growth of nanoporous template was performed at Nanoengineering Laboratory at UIC. On the other hand, the other substrate used was 500 μm 99.9 % pure Al sheet and the anodization was performed at Brown University. Both optical and characterization results were compared to get the best optimization results for its use in optoelectronic devices.

Photoluminescence (PL) and Raman spectral studies were performed to investigate the electronic properties and vibrational properties. Furthermore, intensity dependent PL measurements were performed to study the defects before and after annealing. Electron phonon coupling strength was studied and computed with respect to the laser polarization. Polarization studies were performed to study the polarization anisotropy of these CdS nanowires for its potential use as polarizers.

The potential applications of CdSe/ZnS quantum dots were explored and a novel strategy to detect nanocavities was discussed in the thesis. It is desirable to detect voids of nanoscale dimensions on copper surfaces; indeed such a capability may be of use in detecting voids in copper interconnects and contacts for system reliability. The recent use of quantum-dots (QDs) for sensing applications due to surface chemistry of luminescent quantum dots has encouraged the development of multiple probes for sensing or detecting a wide range of analytes. These QDs have band gap energies that vary as a function of size and have highly tunable excitation frequencies and unique surface chemistry causing

dangling bonds, or adsorbates at the surface. The binding of QDs due to the dangling bonds created by the negatively charged functionalized groups of QDs with the anodic like nanopores structures of copper surface aids in finding the location of the nanopore on the copper surface.

Chapter 1 Introduction

1.1 Introduction

With the advent and rapid development of nanotechnology, semiconductor nanowires (NWs), nanostructures such as nanowires (NWs) and quantum dots (QDs) can be used in future applications. Semiconductor nanoscale structures have generated a great deal of interest owing to their strong confining potentials for electrons and holes and the associated quantum effects [1-3]. Semiconductor nanowire devices are being used as photo-detectors [4, 5], sensors [6], lasers [7, 8], transistors [9, 10], optical switches [11], etc. Recent research in the field of semiconductor nanowires have revealed lot of interesting properties such as polarization sensitivity, [12-14] size-dependent photoluminescence [15], quantum dots in nanowires for light emitting diodes (LEDs) [16, 17], etc. These interesting properties of semiconductor nanowire devices are of great interest and are being employed in both scientific and industrial applications.

As some of these nanowire devices are required to grow freestanding nanowire arrays for which a template having periodic arrays of nanoporous structure needs to be fabricated. One such template having nanoporous structure is anodic aluminum oxide (AAO) template. This template is ideal for growing nanowires by electrochemical deposition since this nanoporous structure is uniform and has vertically directed grown nanopores. Changing the experimental parameters of anodization can easily vary the diameters of these nanopores. The AAO template consists of a nanoporous structure that can be grown and has the following attractive attributes:

(i) Flexibility to vary the size and composition,

(ii) Flexibility of substrate materials, and

(iii) Compatible with various fabrication processes.

Porous alumina templates have the potential to grow vertically directed uniform arrays of nanowires or nanotubes of high aspect ratio. The templates are durable and can withstand high temperatures (up to 800 or 1000 ° C) and changing the experimental conditions can be controlled by the diameter of the pores [18-22].

Other advantages of using a nanoporous insulating alumina matrix template are as follows:

(i) Uniform regular distribution of nanopores of the order of a few nanometers,

(ii) Nanopores which allow vertically directed nanowire growth with high aspect ratio,

(iii) Diameter of cells and pores controlled by changing electrolyte composition and electrochemical processing parameters,

(iv) High reproducibility of the film structure, and

(v) Annealing can be easily performed without losing the structure of the template as it can withstand high temperatures of about 800 or 1000 ° C.

One of the most important II-IV semiconductor compounds, cadmium sulphide (CdS) was selected because it is widely studied and used in optical devices due to its direct band gap and excellent semiconducting properties. Cadmium sulphide nanowires provide a great number of advantages such as high aspect ratio, large surface to volume ratio leading to the formation of strong excitons with large binding energy and excellent light emission and absorption property for optoelectronic applications. Although, there are number of ways to grow CdS nanowires such as chemical vapor deposition (CVD), vapor liquid solid (VLS), metal-organic chemical vapor deposition (MOCVD),

electrodeposition fabrication processes [23, 24], but the two easy and economical ways of growing CdS nanowires are VLS and electrochemical fabrication process. Confinement of energy levels of CdS nanowires grown through these templates have a unique advantage of increased band gap energy due to quantum confinement [25].

The large difference in the dielectric constant of the surrounding media of the nanowires and the free standing nanowires leads to polarization anisotropy. This polarization anisotropy is employed here to demonstrate the possibility of polarization sensitive nanoscale photo detectors that can be useful in optical switches, polarizers, and high resolution detectors [26]. Therefore, investigating the optical, vibrational and electronic properties of the fabricated nanowire array is very important for its use in optoelectronic devices leading to the optimization of these nanowire devices. In this work, the templates were deposited; the pores were formed to grow CdS nanowires via DC electrodeposition and VLS growth. The optical and electronic properties of the grown CdS nanowires were investigated and studied for its use in optoelectronic applications such as solar cells, optical switches, polarizers and other optoelectronic applications. Optical characterization of the grown CdS nanowires was performed using Raman and photoluminescence (PL).

Also, with the discovery of conductive organic polymer, remarkable progress has been made in the field of optoelectronic applications such as solar cells, lasers and light emitting diodes etc [27]. These conductive polymers are preferred for optoelectronic applications because of their lower cost and they are easy to synthesize [28] using solution based processing steps. Recently, large area polymer solar cells are being researched for cost-effective solutions [29]. These conductive polymers are also widely

being used for applications such as disposable sensors [30], microfluidics circuits [31] and lab-on-a-chip systems [32]. CdS/P3HT polymer heterojunction was optically and electrically characterized for its potential use in photovoltaic cells.

Also, other nanostructures such as quantum dots (QDs) and its use in many applications were investigated. QDs are semiconductor nanocrystals, which possess unique quantum mechanical properties. The charge carriers in nanocrystalline QDs are confined in all three spatial dimensions. As a result, the optical and electronic properties are dramatically different than bulk material. QDs have optical properties that can be employed for the development of novel sensors. The surface chemistry of luminescent quantum dots has encouraged the development of multiple probes based on it's binding to molecules such as peptides, nucleic acids or small-molecule ligands. QDs also bind to the surfaces of some metals, which can be useful in detecting the surface properties of metals. We have employed this property of Cadmium Selenide/Zinc Sulphide (CdSe/ZnS) QDs binding to the copper surface to detect the nanopores on the surface if present.

1.2 Background on CdS nanostructure

One of the prototypical II-IV semiconductor compounds, CdS was selected because of its possible use in optical devices due to its direct band gap in the visible spectral range and the excellent semiconducting properties. It is well studied that for hybrid solar cells, CdS would be compatible with conducting polymers such as P3HT [33].

1.2.1 Band structure of CdS material

The electronic band structure plays a vital role in choosing semiconductor devices for electronic applications. Electronic band structure is explained in Figure 1 where the energy of electron *E* is plotted as a function of its wave-vector *k*. The wave-vector can take any value but is always restricted to the first Brillouin zone. The gap between maxima of the valence band (VB) and minima of the conduction band (CB) is referred to as the band gap of the material. A semiconductor that has both extrema of the VB and the CB at the same value of wave-vector *k* is a direct band gap semiconductor. A direct band gap semiconductor has higher quantum efficiency than that of an indirect band gap semiconductor and has higher absorption coefficient whereas in indirect band gap semiconductors, the extrema of conduction and valence band does not occur at the same wave-vector. They have a smaller absorption coefficient and are rarely used for optoelectronic devices. Based on the energy and momentum conservation required in the electron-photon interaction, in a direct band gap semiconductor due to the vertical alignment conduction and valence band, photon absorption is achieved if an empty state in the conduction band is available equals to the energy and momentum of electron in the valence band and the photon. Therefore, the electron easily makes a vertical transition on the *E-k* diagram as shown in Figure 1(a).

In an indirect band gap semiconductor, the minimum of the conduction band and the maximum of the valence band are not at the same wave-vector *k* as shown in Figure 1(b). Therefore, conservation of both energy and momentum during a photon absorption process is achieved if a phonon is absorbed or emitted as illustrated in Figure 1(b) and (c). The probability of having an optical transition is lower in an indirect semiconductor

since it involves a phonon in addition to the electron and photon, than a simple electron-photon interaction in a direct band gap semiconductor. As a result, probability of absorption or the absorption coefficient is much higher in a direct band gap material.

CdS is a semiconductor belonging to II-VI group and has either hexagonal or cubic crystal structure. The CdS nanowires samples investigated and studied in this thesis have hexagonal wurtzite structure. A unit cell lattice of the hexagonal wurtzite CdS is shown in Figure 2.

Hexagonal CdS has a direct band gap with the lowest band gap located at the center (Γ point) of Brillouin zone [34]. The highest valence band Γ_{15} is split into three different band Γ_9, Γ_7, and Γ_7 due to the crystal field and spin-orbit coupling in hexagonal CdS as shown in Figure 3 [35].

The direct band gap of CdS is 2.42 eV at room temperature. CdS has higher absorption coefficient since it has direct band gap and is widely used for optoelectronic applications.

1.2.2 Important parameters of CdS

CdS has high dielectric constants (~10) and small effective masses (~1/10 of effective mass of electron), the exciton binding energy *E* is 27 meV, and also exciton Bohr radius is 23 Å. Dielectric constant at low frequencies along z ($\varepsilon_{0||}$) and perpendicular to z ($\varepsilon_{0\perp}$) of hexagonal CdS are 9.25 and 8.7, respectively. This dielectric constant difference with that of its surrounding and the anisotropy inherent in the material causes a change in polarization sensitivity and electron-phonon interaction along the *z* and perpendicular to *z* axes in the bulk material. In the nanowires this behavior may be different. Some other parameters of hexagonal CdS are listed in Table

Table I: Important parameters of CdS.

Parameter	Value
Band gap (eV)	2.42
Dielectric constant at low frequency along z ($\boldsymbol{\varepsilon_{0\|\|}}$)	9.25
Dielectric constant at low frequency perpendicular to z ($\boldsymbol{\varepsilon_{0\perp}}$)	8.7
Dielectric constant at high frequency along z ($\boldsymbol{\varepsilon_{\infty\|\|}}$)	5.5
Dielectric constant at low frequency perpendicular to z ($\boldsymbol{\varepsilon_{\infty\perp}}$)	5.53
Lattice constant along z ($\mathbf{a}_{\|\|}$)	4.14
Lattice constant perpendicular to z ($\mathbf{a}_{\perp}$)	6.7
Thermal conductivity (W/cm.K)	0.2
Bulk modulus (GPa)	61.5

1.3 Background on CdSe/ZnS Quantum Dots

CdSe/ZnS Quantum dots (QDs) are core shell semiconducting nanocrystals with ZnS as the shell to the core of CdSe. Their properties are unique and intermediate between those of individual molecules and those of bulk, crystalline semiconductors. They have modular properties because these properties can be modulated with respect to their size and shape. This allows a wide range of highly tunable emission and excitation wavelengths of these QDs. These core shell semiconducting nanocrystals consist of semiconductor core material and shell of a semiconductor. The core and the shell are typically of type II–VI, IV–VI, and III–V semiconductors. Usually, quantum dots without the shell have low fluorescence quantum yield due to surface related trap states. On the

other hand, core shell QDs have higher quantum yield as the shell passivates the surface trap states present [36]. The other advantages of having the shell with core quantum dot is that it provides protection from environmental changes, degradation, increased longevity [37]. The emission wavelength can be further tuned to a wider range of wavelengths than with individual semiconductor by controlling the size, shape, and composition of the core and shell. The core shell semiconducting nanocrystals or QDs can be of the following types:

(i) Type I

(ii) Reverse Type I

(iii) Type II

(iv) Doped Core Shell Semiconductor Nanocrystals

Type I

In Type I the band gap of the core is smaller than the shell band gap. This can be seen in Figure 4, CdSe having a band gap of 1.74 eV, which is higher than, ZnS band gap of 3.54 eV due to which both the valence and conduction band of the core are within the band gap of the shell semiconducting material. Other examples of Type I QDs are CdSe/CdS, and InAs/CdSe.

Reverse Type I

In reverse type I, the core has larger band gap than the shell. As shown in Figure 4 (b) the conduction and valence band edge of the shell are within the core band gap and by changing the core and shell thickness varies the emission wavelength. Some examples of this type are CdS/HgS, CdS/CdSe, and ZnSe/CdSe [36].

Type II

In type II, the band edges of the shell are both either higher or lower than the conduction and valence bands of the core as shown in Figure 4 (c). Some examples of this type are ZnTe/CdSe, CdTe/CdSe, and CdS/ZnSe.

Doped Core Shell Semiconductor Nanocrystals

The optical properties of semiconductor nanocrystals are strongly influenced by doping levels of a semiconductor [38]. Sometimes, doping the shell of CdSe/ZnS with manganese changes the magnetic properties of the QDs and introduces another option of tuning the nanostructure for many applications such as imaging and memory devices [39].

These core shell QDs fluoresce and imaging these QDs is easy under fluorescence microscope and therefore this property of QDs is employed in many applications for detecting, labeling biological cells and also other optical applications. This property of these QDs has been used in this thesis for detecting nanopores on copper surface. Also, in this thesis, QDs have been used for detecting heavy metal ions in fluids.

1.4 Organization of Chapters

Chapter 2 discusses the growth of nanowires by both the mechanisms i.e. DC electrodeposition in anodized alumina templates and vapor liquid solid (VLS) growth. It also highlights the bottlenecks during growth of the CdS nanowires. The material and composition of the grown nanowires were investigated using Energy Dispersive Spectroscopy (EDS). For the growth of the nanowires, some of the anodized nanoporous templates were grown in aluminum sheet at Brown University and some of the anodized templates were grown on ITO coated glass substrate at UIC Nanoengineering Laboratory.

Growth of nanowires using DC electrodeposition is discussed. Comparison of VLS grown and electrodeposited growth is also discussed in this chapter. Chapter 3 focuses on the experimental results of Photoluminescence (PL) studies of these grown nanowires before and after annealing investigating more its structural properties. The depletion layer width of the CdS nanowire was calculated and the depletion layer width calculation results were in accordance with the PL. Also, the polarization anisotropy of these nanowires was investigated using polarization filter and PL results in different configurations have also been discussed. In Chapter 4, Raman of the CdS nanowires before and after annealing is discussed. Also, Raman in different orientations was performed to investigate the wurtzite crystal properties of CdS nanowires. Also, electron-phonon coupling constant was calculated to study its variation with the orientation angle. Chapter 5 discusses the electrical characterization and I-V characteristics of the grown CdS nanowires together with conductive polymer P3HT. Furthermore, PL measurements were performed on these CdS/P3HT heterojunctions for its optical characterization study. In Chapter 6, a novel strategy of using CdSe/ZnS QDs for the detection of nanopores on copper surface has been discussed. Chapter 7 gives the conclusion of this study and future work.

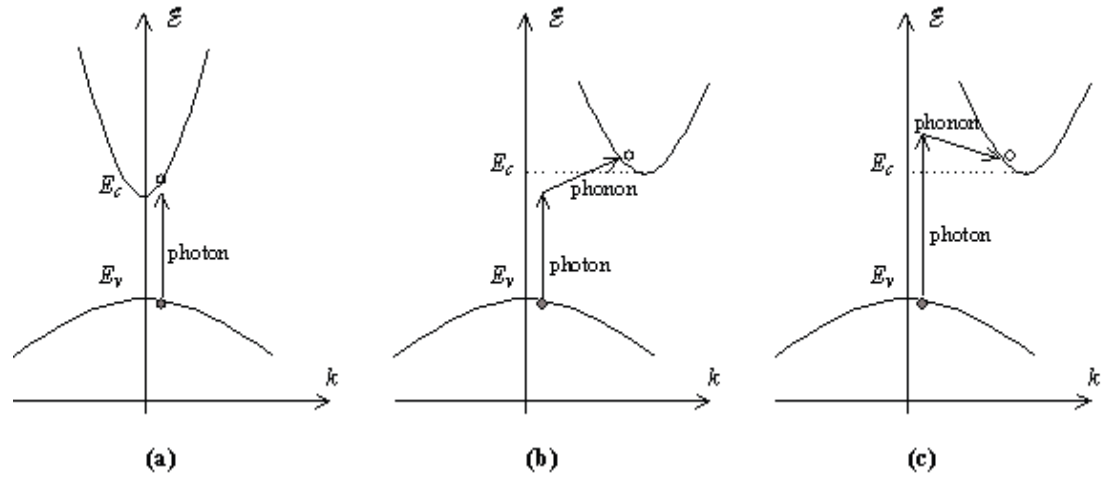

Figure 1: E-k plot illustrating a) direct band gap semiconductor undergoing photon absorption b) Indirect band gap semiconductor undergoing photon absorption c) Indirect band gap semiconductor undergoing photon absorption assisted with phonon emission [40].

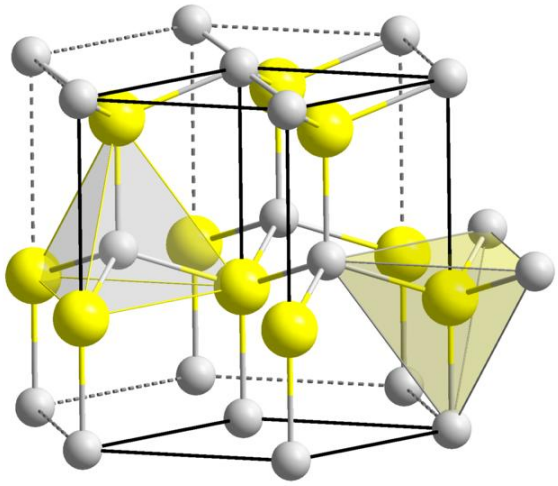

Figure 2: Wurtzite unit cell lattice of CdS crystal [41].

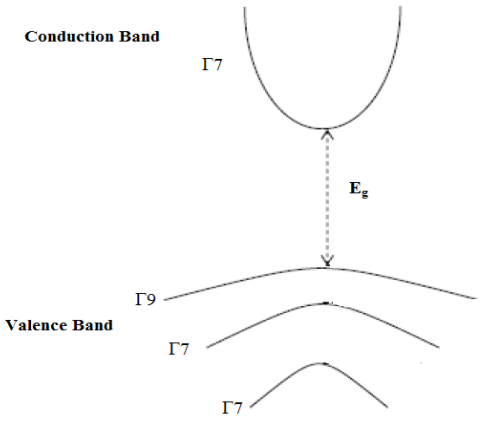

Figure 3: Electronic band structure of CdS.

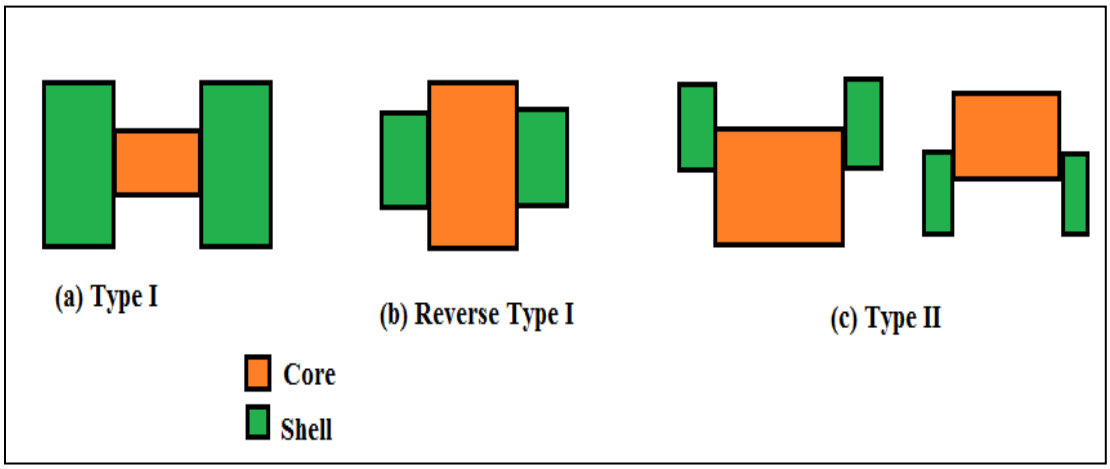

Figure 4: Types of configurations of core shell QDs.

Chapter 2 Growth of CdS Nanowires

In this chapter, introduction to the fabrication of nanowires is discussed in Section 2.1. The growth of nanoporous templates to grow nanowires is given in Section 2.2. The Section 2.2.1 discusses the growth of the nanoporous templates on ITO coated glass substrate performed at UIC. The Section 2.2.2 gives the experimental details of the growth of nanoporous templates in 500 μm thick aluminum sheet performed at Brown University by us. The Section 2.2.3 discusses about the results of the growth of the templates. The Section 2.3.1 discusses the self-assembly and growth of CdS nanowires in both of these templates i.e. on ITO coated glass substrate and in an anodized aluminum sheet of higher thickness of 500 μm. The results discussed are about the characterization of these grown nanowires in both the templates.

2.1 Introduction to the Fabrication of Nanowires

CdS nanowires can be grown using other processes such as chemical vapor deposition, metal-organic chemical vapor deposition (MOCVD), physical vapor deposition, sol-gel synthesis, solvothermal synthesis, electrodeposition and vapor- liquid solid growth. The two most economical, efficient and easy techniques of fabricating CdS nanowires are electrodeposition and VLS growth.

Growth of nanowires of semiconductor materials of II–IV group such as CdS has been demonstrated using a vapor–liquid–solid (VLS) technique [42]. In Section 2.4, experimental details and results are discussed for the growth of CdS nanowires using vapor-liquid solid growth on ITO coated glass substrate. The topographical features of these CdS nanowires were also studied using field emission scanning electron

microscopy. Also, these grown CdS nanowires were characterized by Energy Dispersive Spectroscopy (EDS) to investigate its composition.

2.2 Growth of nanoporous templates

2.2.1 Experimental details of growth of anodized alumina template on ITO coated glass substrate [43]

Commercially available ITO-coated 1”×1” glass substrate (1mm thick) were ultrasonicated for 1 hour in acetone and isopropanol to clean the substrate to remove the organic residues, followed by the deionized water rinse and air gun blow dry. A thin layer of aluminum of 200 nm thickness was deposited at a rate of 0.1 nm/s using e-beam evaporation. Prior to the deposition of aluminum, an interlayer of titanium of 5 nm thickness was deposited between the Al and ITO. This was to prevent the poor connectivity and delamination of aluminum during anodization from the ITO-coated glass [44, 45]. The interlayer of Ti layer was deposited using e-beam evaporation without any vacuum break between Ti and Al layer [46]. The template was anodized at a potential of 40 V and current of 0.2 A to develop the nanopores in a weak acid of 0.3 M oxalic acid. The anodized template was heated in a mixture of phosphoric acid (5 wt. %) and chromic acid (10 wt. %) at 60 °C to remove the aluminum oxide layer and excess of aluminum. Since the pores formed after the first anodization step were poor and non uniform, the anodized template was again anodized at the same conditions of first anodization at a potential of 40V and 0.2 A in 0.3 M oxalic acid at 2-8 °C. The nanopores produced were of 10-60 nm in diameter. The diameters of the pores was controlled by varying the anodization parameters such as temperature and also with the pH of the acid used according to the protocol given in Ref. [47].

After the two-step anodization, very uniform pores of 10-60 nm developed but it also grew with a barrier layer of oxide at the interface of the Al and Al_2O_3. This aluminum oxide barrier layer and non-uniformity in barrier layer thickness causes some problems in the growth and quality of the nanowires electrodeposited in the pores resulting in much lower filling of nanowires in these pores. The barrier layer can be removed by immersing the substrate in 5% by weight phosphoric acid (H_3PO_4) for 3-4 minutes. The barrier layer formed at the bottom of the template can be removed by either by 5 % by wt. phosphoric acid or dry etch with chlorine based gases [46-48], but as shown in the referenced work, the barrier layer can be removed with the phosphoric acid etch without damaging the template.

2.2.2 Experimental details of growth of nanoporous templates in aluminum sheet

CdS nanowires were grown in anodized aluminum sheet metal of thickness of 500 µm. The anodized template was prepared using the protocol given in Ref [47]. The aluminum (Al) metal sheet (99.9 % purity) of 2” × 0.5” × 0.020” dimensions was cleaned by ultrasonication in acetone for 1 h followed by ultrasonication in methanol for 1 hour. These Al metal sheets were then electropolished in perchloric acid and ethanol solution having volume ratio of 1: 5 at 0 °C for 15 minutes. Then these templates were anodized at a potential of 40 V for a minimum of 16 hours and the temperature was maintained at 10 °C throughout the process. After the first anodization step, the oxide layer was removed by immersing the sample in a solution of 1.8 % wt. chromic acid and 6 % wt. phosphoric acid at 60 °C for 4-5 hours. The second anodization was performed with the same conditions as that of the first anodization step but the time of the

anodization this time was only 20 minutes. Chemical Reactions at anode, cathode and in the electrolyte solution are as follows:

- At anode:

$$2Al + 3\,H_2O \rightarrow Al_2O_3 + 6H^+ + 6e^-$$

- At cathode:

$$6H^+ + 6e^- \rightarrow 3\,H_2$$

- Dissolution of alumina:

$$Al_2O_3 + 6H^+ \rightarrow 2Al^{3+} + 3\,H_2O.$$

The barrier layer was removed by dipping the anodized template in 0.5 M phosphoric acid for 75 minutes at room temperature. The steps for anodization are shown in Figure 5. The growth of nanoporous templates on anodized alumina template involved the step of electropolishing the aluminum at a very low temperature of 0 °C in perchloric acid and ethanol solution 1: 5 vol. ratio which resulted in better nanoporous structure and did not involve the step of annealing the template to improve crystallinity.

2.3.2 Results and Discussion

The aluminum sheet metal templates after the two-step anodization were examined under JEOL Scanning electron microscope. The SEM images of the anodized templates after the removal of barrier layer are shown in Figure 6. The barrier layer was not seen in any of the templates in the following SEM micrographs.

The thin film of aluminum of 200 nm was susceptibility to crack after anodization and therefore annealing was done for one hour at 200 °C to improve the crystallinity of these templates. On the other hand, the nanoporous template in aluminum sheet of 500 µm was more stable since electropolishing was performed before anodization.

2.3. Growth of Nanowires by DC electrodeposition

AC electrodeposition in an AAO template is the best process to fabricate vertically aligned CdS nanowires [47-50]. However, in this work CdS nanowires were deposited via DC electrodeposition. DC electrodeposition of CdS nanowires is normally not preferred over AC electrodeposition commonly for samples with very narrow pore diameters [47]. However, in our work using a simple DC electrodeposition process into the narrow pores of 10-60 nm diameters grew CdS nanowires. It has been reported in [47] that DC electrodeposition was not an easy process for growing nanowires in narrow pores, but we were able to achieve the growth of CdS nanowires and decent quality wires.

2.3.1 Experimental details for the growth of nanowires

The experimental conditions for growth of nanowires was same for both type templates grown at UIC and Brown except for the deposition time changing with respect to the thickness of template. The electrolyte for CdS electrodeposition was a solution of dimethyl sulfoxide (DMSO) comprising of 0.055 M $CdCl_2$ and 0.19 M elemental sulfur [51, 52]. The temperature of the electrolyte was 120-150 °C during the electrodeposition growth and current density of 15 mA/cm^2 was applied for 7-10 s for the templates on ITO coated glass and for 1 hour for aluminum sheet. After the electrodeposition, the sample

was rinsed in hot DMSO followed by acetone and cleaned in deionized water. The AAO template was dissolved in 1 M NaOH solution at room temperature for 8 minutes to liberate the CdS nanowires. These nanowires were annealed at 500 °C for 1 hour for improving the crystallinity of these nanowires. The flowchart for the growth of CdS nanowires is shown in Figure 7.

2.3.2 Results and Discussion for the growth of nanowires

Self-assembling and growing CdS nanowires in an AAO template is not easy due to the presence of a barrier layer of aluminum oxide, which is difficult to etch out completely, thus causing non-uniformities in the growth of nanowires. The template should be free of cracks and defects [53, 54]. The electrodeposition of CdS nanowires involves the following three steps.

1) Elemental sulfur dissociates into S^{2-} ions in the solution.
2) $CdCl_2$ also dissociates into Cd^{2+} ions.
3) The present S^{2-} ions react with Cd^{2+} ions to form CdS crystallites in the nanopores of the template, thus forming the nanowires [55]. These crystallites nucleate on the walls of pores initially forming nanotubes and gradually these nanotubes get filled up with CdS crystallites forming nanowires [56].

The surface morphology of these CdS nanowires grown in the AAO template on ITO coated glass substrate were investigated using the JEOL 7500 Field Emission Scanning Electron microscope (FESEM) after the dissolution of the AAO template in 1 M NaOH solution for 5-8 minutes. The top view and side view SEM micrograph is shown in Figure 8 (a) and (b) which confirms the growth of nanowires of average

diameter approximately 30-60 nm. Also, for comparison the CdS nanowires grown in the aluminum sheet templates are shown in Figure 9 (a) and (b).

Energy Dispersive X-ray Spectroscopy EDS studies were performed on these electrodeposited CdS nanowires and results are shown in Figures 10 and 11.

Peaks of Cd and S in Figure 10 confirm the growth of CdS nanowires. Also, there were peaks of indium (In), oxygen (O) and silicon (Si) due to the ITO coated glass substrate. aluminum (Al) was also detected because there were some traces of aluminum left after the dissolution of alumina template in NaOH solution. Furthermore, to study the elemental composition of CdS nanowires grown in anodized alumina template of thickness 500 μm, EDS was performed. The results of the EDS are shown in Figure 11, which confirms the presence of CdS nanowires. There were other peaks of Al, O, and Si due to the presence of aluminum oxide template and Si can be present due to some dust particles.

2.4 Growth of CdS nanowires using Vapor liquid Solid (VLS) Growth

Vapor liquid solid growth is a popular bottom up approach method technique to grow semiconductor nanowires of group III–V (InP, GaAs, and GaN), II–VI (ZnSe, CdS, and ZnO), IV (Si, Ge) since its flexible and a controlled growth of nanowires is possible. This VLS growth method was developed in 1960s by Wagner and Ellis for the growth of silicon whiskers [57]. A schematic showing VLS growth has been shown in Figure 12. In case of VLS growth, a metal particle of small size on substrate is heated to form a liquid/solid interface, thus forming a local liquid phase epitaxial system. So far gold has been mostly used as catalyst metal particle for the growth of nanowires even though a number of other metals can be employed [58]. The VLS nanowire growth is a process

which initiates with the dissolution of gaseous reactants resulting in nano-sized liquid droplets of the catalyst metal followed by nucleation and growth of single-crystalline wires or rods. The size of the alloy droplet determines the diameter of the nanowires, which is dependent on the size of the starting metal seed.

2.4.1 Experimental Details for VLS growth of CdS nanowires

For VLS growth of the nanowires, the ITO coated glass substrates were cleaned by soap water. These cleaned substrates were then ultrasonicated in acetone for 30 minutes followed by another 30 minutes ultrasonication in isopropanol and dried in nitrogen. Gold of 5 nm thickness was sputtered on these cleaned ITO glass substrate to catalyze the growth of nanowires. The CdS nanowires were synthesized in a quartz tube furnace with dual zone furnace heating instrument. For VLS growth of CdS nanowires, CdS powder (~0.8 g, 99.999% pure, purchased from Sigma Aldrich) was placed in one heating zone and the ITO glass substrate with the sputtered gold nanoclusters in the second heating zone. 5% Hydrogen with 95 % Argon was used as the transport gas with a flow rate of 100 sccm. The source and sample were heated to 900 and 580 °C, respectively for 1 hour. Field emission scanning electron microscopy imaging was performed using JEOL 7500 FESEM to study the morphology and ascertain the growth of nanowires. Raman scattering and photoluminescence spectral studies were employed to investigate the longitudinal optical phonon modes and the electronic states of the CdS nanowires.

2.4.2 Results and Discussion of VLS growth of nanowires

CdS nanowires were grown by VLS technique. The ITO coated glass substrates were cleaned and sputtered with 5nm of thickness of gold, which served as a catalyst for the growth of nanowire. CdS nanowires were grown in dual zone tube furnace having CdS powder (~1g, 99.9% Sigma Aldrich) as source in one zone at 900 °C and the ITO coated glass with gold nanoclusters in the second zone at 580 °C for one hour and transport gas was 5% Hydrogen with 95% Argon. The SEM images of these CdS nanowires by VLS growth are shown in Figure 13.

To know the elemental composition of these samples Energy Dispersive X-ray Spectroscopy (EDS) were performed.The EDS result for the VLS grown nanowires are shown in Figure 14. Figure 14 shows that the Cd, S are present in the sample confirming the growth of CdS nanowires. In and O are due to the ITO coating on the glass. Si is probably present because of the glass substrate or due to dust particles. Furthermore, studies like Photoluminescence and Raman spectral studies were performed to probe the electronic, optical and vibrational properties of these nanowires which are discussed in detail in Chapter 3 and Chapter 4.

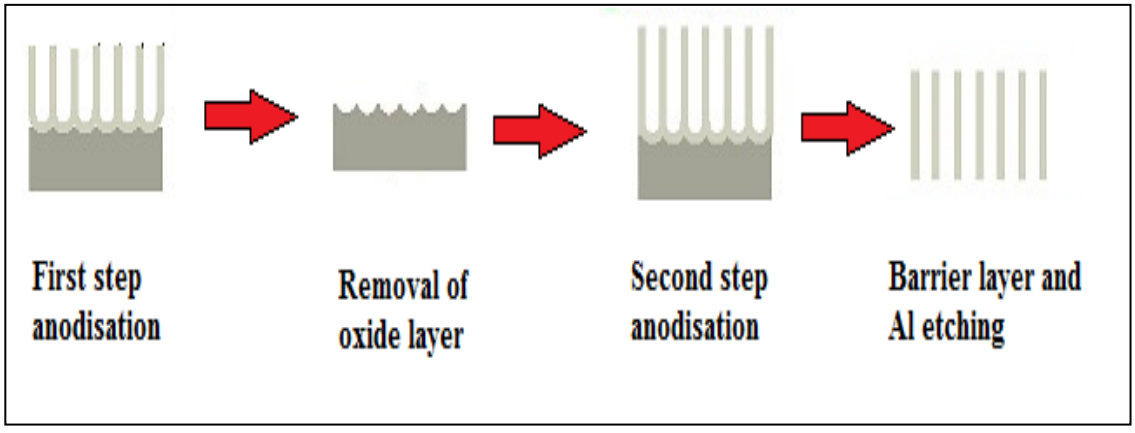

Figure 5: Steps involved in the anodization of aluminum.

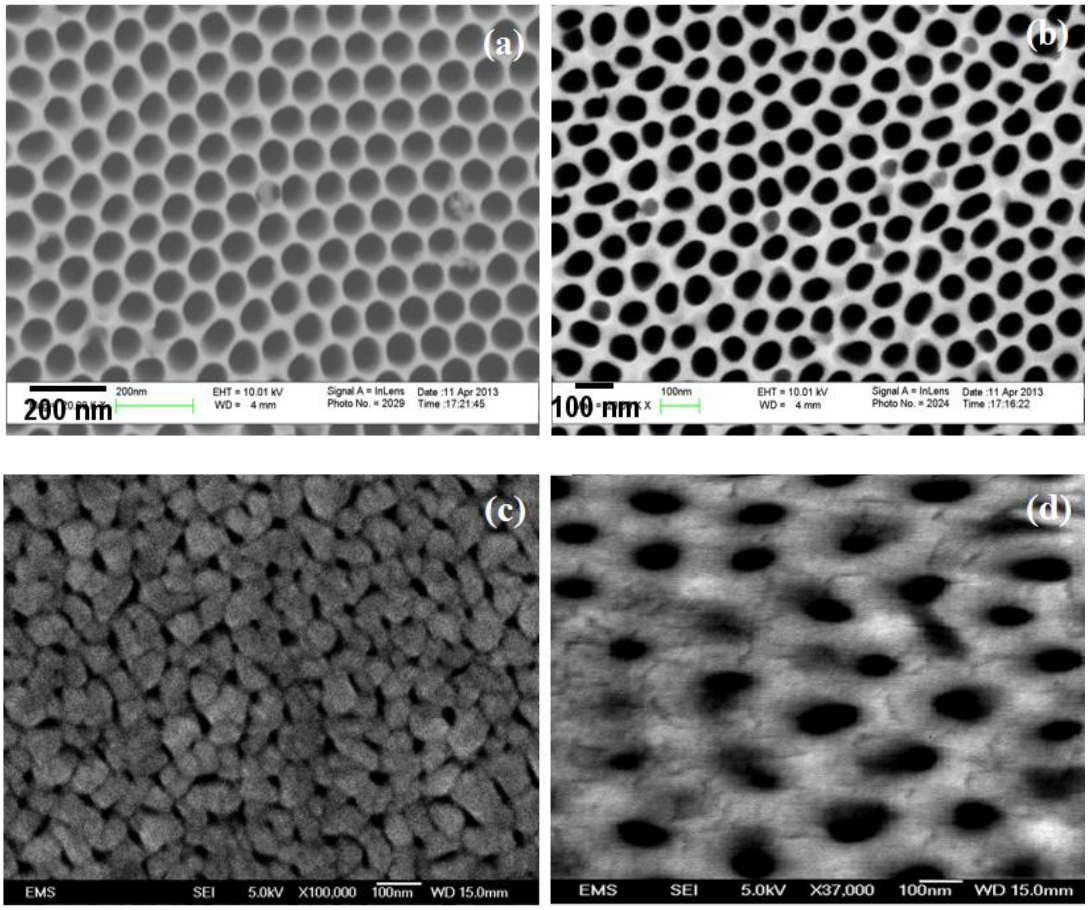

Figure 6: SEM micrographs of the anodized alumina templates after the removal of barrier layer grown at (a) & (b) Brown university in 500 µm aluminum sheet, (c) & (d) UIC in 200-250 nm aluminum deposited on ITO coated glass substrate.

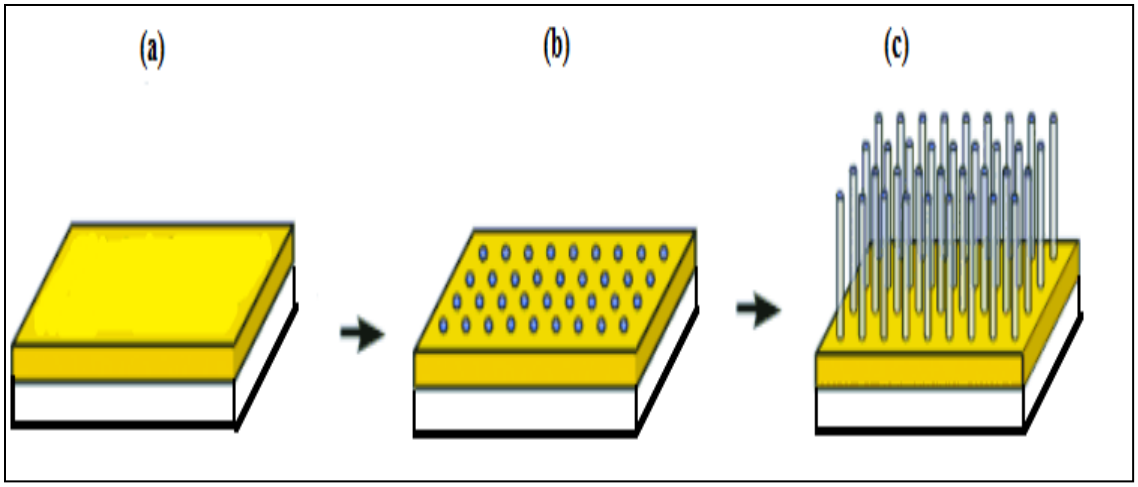

Figure 7: Flowchart for the fabrication of CdS nanowires (a) 200 nm of aluminum layer (yellow) deposited on ITO coated glass substrate (b) After anodization of Al layer leading to formation of nanopores of 10 -60 nm. (c) CdS nanowire array after the DC electrodeposition growth.

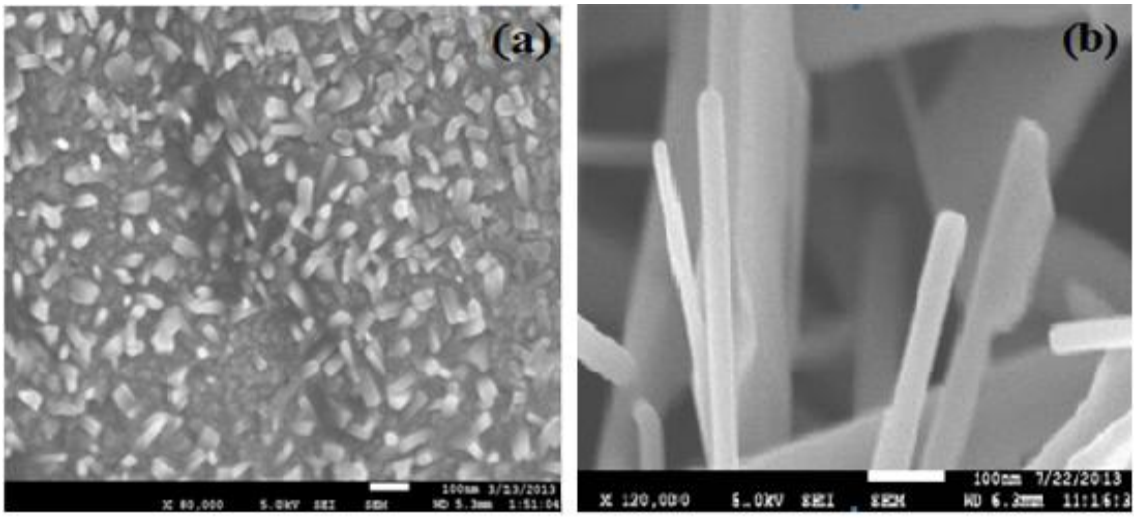

Figure 8: (a) top view (b) side view SEM micrograph of CdS nanowires of 30- 60 nm in diameter after annealing [43].

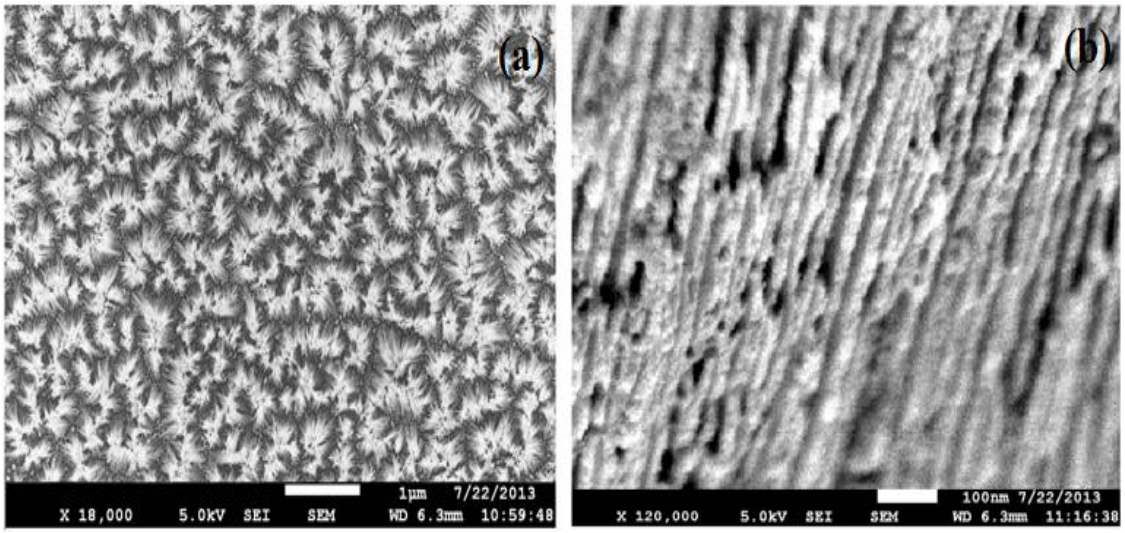

Figure 9: (a) top view (b) side view SEM micrograph of CdS nanowires grown in anodized aluminum oxide sheet.

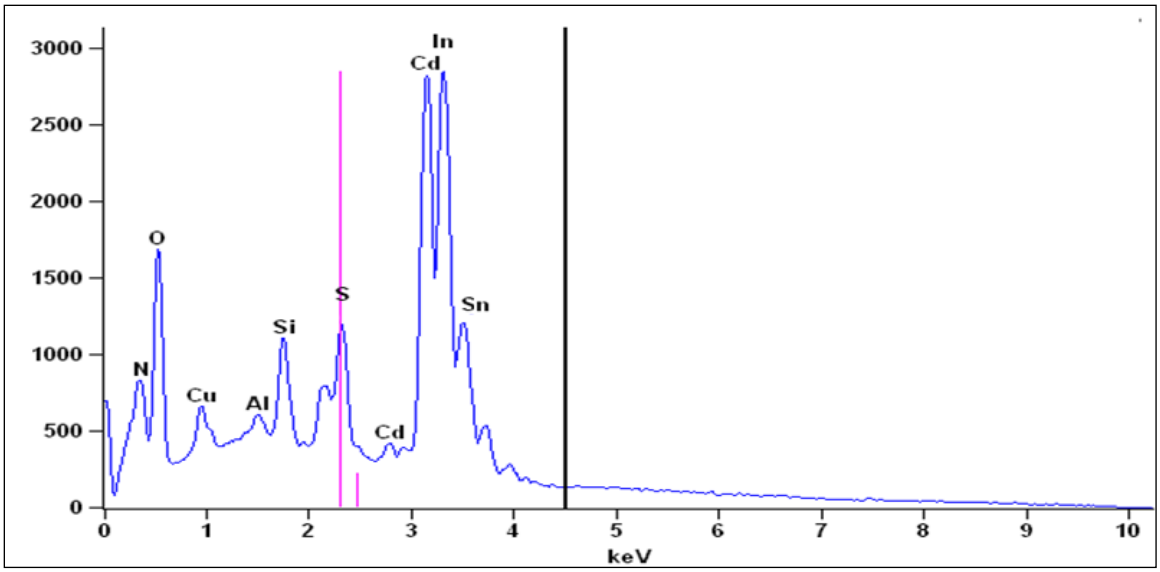

Figure 10: EDS of the CdS nanowires grown on ITO coated glass substrate by electrodeposition.

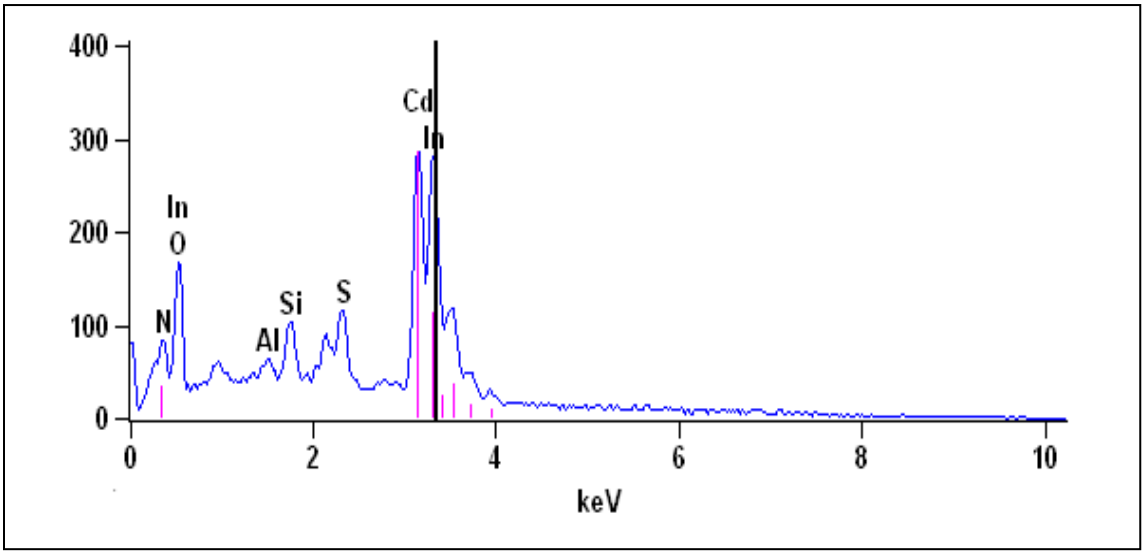

Figure 11: EDS Spectra of CdS nanowires grown in anodized alumina metal sheet of 500 µm.

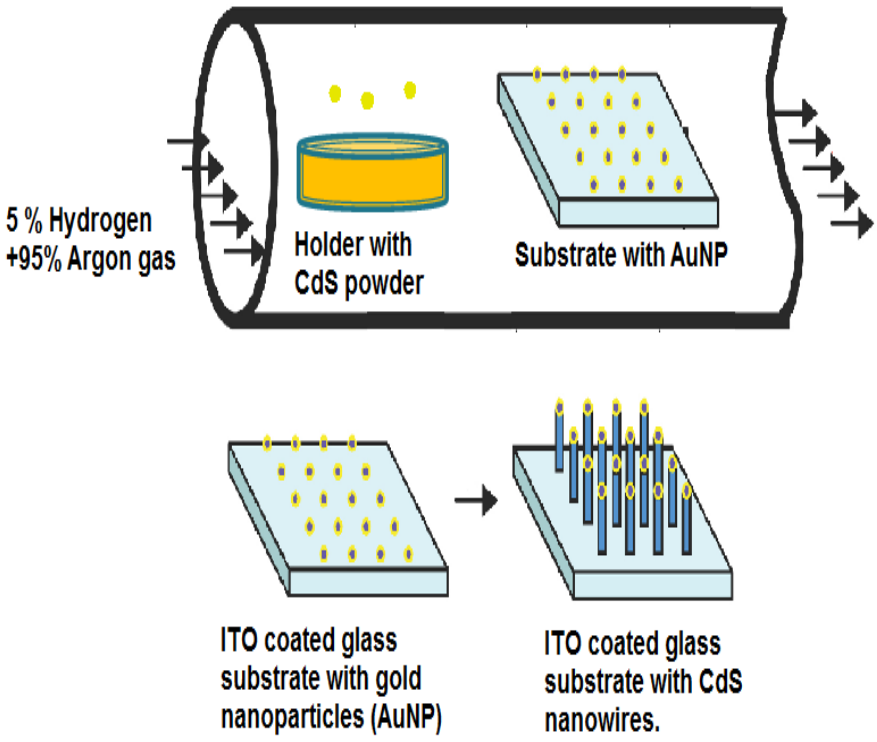

Figure 12: VLS growth mechanism.

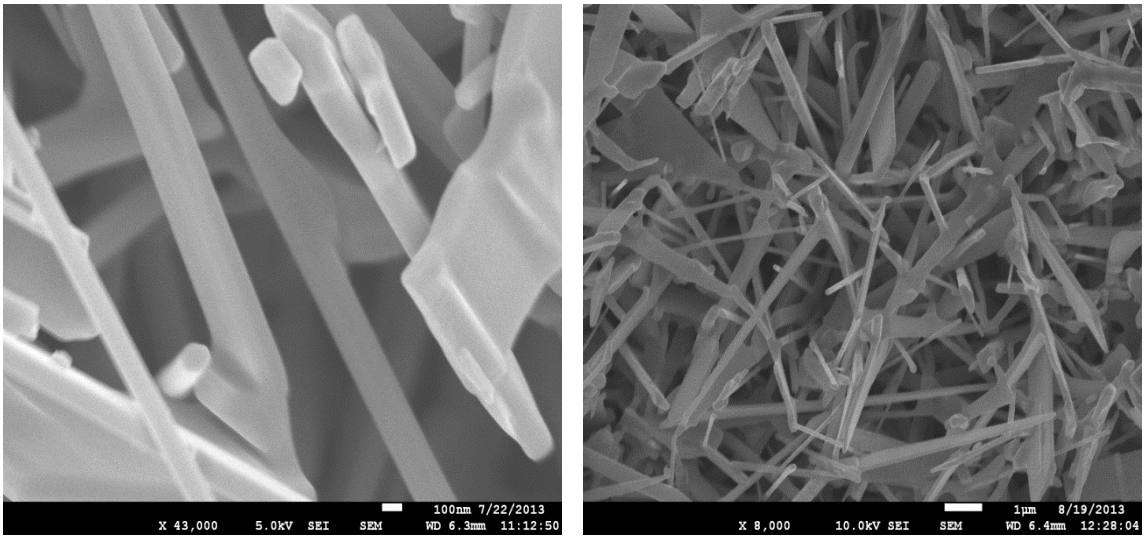

Figure 13: SEM images after the VLS growth of CdS nanowires.

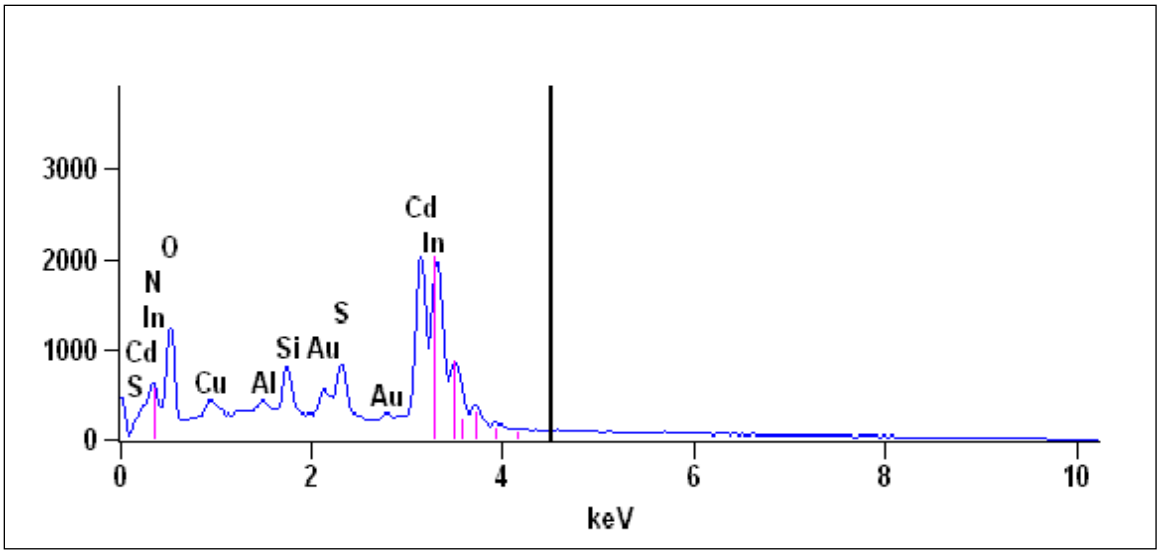

Figure 14: EDS result for VLS grown CdS nanowires.

Chapter 3 Photoluminescence characterization of CdS nanowires

The photoluminescence (PL) is a powerful tool to investigate the electronic structure of the material. In this chapter, the characterization of these grown nanowires is explained in this chapter. Introduction to the PL process and PL/Raman set up is discussed in Section 3.1 and 3.2, respectively. The PL characterization of these nanowires has been explained in Section 3.3.1. Also, the intensity based PL measurements were performed to further investigate the underlying recombination processes in these PL experiments and the defect states present before and after annealing. Section 3.3.2 discusses the analysis and theoretical calculation of the nanowire diameter and depletion width. The PL characterization of the VLS grown CdS nanowires are discussed in Section 3.4. PL based polarization measurements were performed to study the polarization anisotropy of the vertically directed grown nanowires via DC electrodeposition in Section 3.5. Polarization based studies were performed on these grown nanowires for its use in polarization sensitive nanoscale devices.

3.1 Introduction

Optical spectroscopy is very useful for material characterization and to investigate the electronic structure of the material. This is a very important technique to study the properties of a semiconductor. In optical spectroscopy, photons having energies greater than the band gap of the semiconductor are used to excite electrons to the conduction band, leaving holes in the valence band. There are many methods of optical characterization of materials and one such method of characterization is PL, which is

widely used in research to probe the electronic structure and properties of the desired material.

PL is a powerful method to study the electronic properties and dynamic processes of variety of materials and is a contactless method. As explained in Figure 15 in PL, the incident photon energy has to be larger than the band gap of the semiconductor so that the electrons can be activated from the valence band to the conduction band. Then, the electrons will scatter to the ground state in the conduction band non-radiatively. When these electrons recombine with the holes in the valence band, they will emit lights.

An electron and a hole can either recombine non-radiatively or radiatively by emitting phonons or photons respectively. Therefore, photoluminescence spectroscopy can be used for semiconductor band gap determination, impurity levels, defect detection, and phonon-carrier interactions estimation.

3.2 The PL/Raman experimental set up

The spectrometer used for the PL and Raman measurements is the Acton SpectroPro-2500i 0.500-meter focal length, which has three grating imaging monochromator (manufactured by Princeton Instruments). The three gratings available for use in PL/Raman system are as follows:

(a) 1200 grooves/mm,

(b) 2400 grooves/mm, and

(c) 3600 grooves/mm.

The three gratings are on a rotating turret where any one of the three gratings present in the system can be used. The spectrum is obtained with the help of liquid nitrogen cooled charge coupled detector (CCD). The working temperature for the CCD is

-120 °C (manufactured by Roper Industries, Inc.). The laser used was a continuous wave He-Cd laser purchased from KIMMON Koha Co., Ltd., which provides two output wavelengths: 325 nm and 441.6 nm.

3.3 Photoluminescence of CdS nanowires grown using electrodeposition

3.3.1 PL of CdS nanowires grown on ITO coated glass substrate

The CdS nanowires were self-assembled in AAO template on an ITO coated glass substrate using DC electrodeposition. The photoluminescence (PL) spectrum of the grown CdS nanowires was investigated using a He–Cd laser of wavelength 441 nm for excitation at room temperature. The PL spectrum for the as grown CdS nanowires is shown in Fig. 16 (a). An emission peak at 506 nm was observed and is due to attributes of the CdS nanowires and the emission was somewhat weak. However, the emission became broader and peak moved to 514 nm closer to the bulk value of 2.42 eV after annealing in nitrogen gas for 1 hour at 500 °C, as shown in Figure 16 (b). The intensity of the emission (the area under the PL peak) increased by a factor of 4.36 after annealing. The narrow peak observed at higher energy of 506 nm, before the annealing is due to the confinement in the few narrow wires of better quality. Somehow, after annealing, the total intensity of the PL peak increased but the line width is broader and encompasses both narrow and wider wires which were likely not luminescent earlier due to defects which were annealed out. Thus, after annealing the peak moved to a higher wavelength where the PL is centered at the value for wider wires. It is also possible that some of the increased signal can be from partially from the bulk region where there are no wires, but mainly the luminescence must still be from nanowires since the feature is broad and the SEM pictures show distinct nanowires.

The same behavior of emission peak shifting to higher wavelength, after annealing the sample at 500 °C for 1 hour in nitrogen has also been observed in [55]. This change in luminescence emission indicates that the array has a distribution of different diameters of nanowire. There is a possibility that there are more nanowires of wider diameters becoming involved in the emission process after annealing. Also, by looking at the SEM image in Figures 8 (a) and 8 (b), it was observed that the nanowires grown were not all of the same diameter, some were narrow and wide having a range of diameter of 20-60 nm.

Also, the photoluminescence experiments with respect to laser power were performed for the investigation of underlying recombination methods. PL was performed before and after annealing with different neutral density filters (purchased from Thorlabs Inc.) to evaluate the crystal quality. It has been reported in [59] that the luminescence intensity I of PL emission lines is proportional to P^k, where P is the power of the exciting laser radiation with k having value of $1 \leq k \leq 2$ is for band to band transition and $k < 1$ is for transitions due to defects and acceptors/donors. The PL spectral intensity for various transmission laser power densities before and after annealing has been shown in Figures 17(a) and 17 (b) and the plot for the PL intensity with respect to various transmission laser power density percentages is in Figure 18. The plot of PL intensity area under the curve with respect to different excitation power is a near linear plot with a positive slope, which improves in linearity on annealing thus showing that the recombination was mainly band-to-band. From the plots, one can see that there were some defect states prior to annealing but after the annealing the linearity with intensity improved.

3.3.2 Theoretical calculation of the nanowire diameter and depletion region width

Considering the CdS nanowire to be a cylindrical quantum well of radius *R*, which is the radius of the nanowire, the Hamiltonian operator for free electrons [60] in the cylindrical well will be given by the equation

$$\widehat{H} = -\frac{\hbar^2\nabla^2}{2m} + V(r) \tag{3.1}$$

where V(r) is the potential and is given by the following equation

$$V(r) = 0 \text{ for } r < R \text{ and } \infty \text{ for } r > R \tag{3.2}$$

where R is the radius of the CdS nanowire.

The Schrodinger equation in polar coordinates which defines the corresponding energy eigenvalues of the states occupied by free electrons is given by

$$(\nabla^2 + \rho^2)\psi(r,\theta) = 0 \tag{3.3}$$

where $\rho^2 = \frac{2mE}{\hbar^2}$ with boundary condition $\psi(R,\theta) = 0$ at the walls of the cylindrical well.

The resulting radial solution [60] for Schrodinger equation (3.3) is given by

$$0 = \frac{\mathrm{d}^2R(r)}{dr^2} + \frac{dR(r)}{rdr} + \frac{(\rho^2r^2 - m^2)R(r)}{r^2} \tag{3.4}$$

The resulting radial solution can be considered as a Bessel's differential equation of variable $z = \rho r$ and has cylindrical Bessel solution $J_m(\rho r)$. Since boundary condition $\psi(R,\theta) = 0$ results in having $J_m(\rho r) = 0$.

The solutions are cylindrical Bessel function $J_{(l,n),}$ which is the zero of the nth Bessel function where n is number of radial nodes. The state of lowest energy has zero angular momentum (l =0).

Therefore the zeros are the eigenstates of the energy with eigen energy values given by

$$E_{g_{CdS}} = \frac{\hbar^2 j_{l,n}^2}{2m_e^* R^2} + \frac{\hbar^2 j_{l,n}^2}{2m_h^* R^2} + E_{g_{bulk}} \quad (3.5)$$

The lowest confined energy level of nanowires corresponds to the zero of Bessel function $j_{(0,1)}$ at 2.4. After solving for E_{gCdS} =2.45 $\pm$ 0.005 eV (Peak at 506 nm) and E_{gbulk} = 2.401 eV $m_e = 0.2\ m_o$ and $m_h = 0.7m_o$ as reported in [61] we get R or r_{core} = 5.23 $\mp$ 0.25 nm and with E = 2.412 $\pm$ 0.005 eV (peak at 514 nm after annealing) we get R or r_{core}= 15.38$\mp$ 3.61 nm.

However, the average diameter measured before and after annealing from the SEM micrographs in Figures 6 (a) and (b) were 55 nm. The diameters measured from the SEM images of Figures 6 (a) and (b), however were greater than the calculated diameters of the nanowires due to the presence of the surface induced depletion region.

Surface-state charges in a nanowires leads to a depleted region on the outer shell of CdS nanowires. The depleted region and conductive inner core of the CdS nanowire are shown in the cross section schematic of the nanowire in Figure 19 (a) and the resulting band diagram is shown in Figure 19 (b). The depletion of semiconducting NW can be treated analytically with Poisson's equation in cylindrical coordinates explained in [62] as given in the equation (3.6).

$$\frac{\delta^2 \varphi}{\delta r^2} + \frac{\delta \varphi}{\delta r} + \frac{qN_d}{\varepsilon \varepsilon_0} = 0 \quad (3.6)$$

The general solution of the Poisson equation (3.6) in cylindrical coordinates is given by the following equation (3.7)

$$\varphi(r) = \frac{-qN_d}{4\varepsilon\varepsilon_0} r^2 + C_1 \ln(r) + C_2 \quad (3.7)$$

where φ is the potential measured with respect to the conduction band energy, r is the distance measured in radial direction, q is the electronic charge, N_d is the ionized dopant density, ε is the dielectric constant of the CdS nanowires which is 5.6, ε_0 is the permittivity of free space, C_1 and C_2 are arbitrary constants.

The constants C_1 and C_2 may be found by applying the boundary conditions

$$\frac{\delta\varphi(r_{core})}{\delta r} = 0 \text{ and } \varphi(r_{core}) = 0 \tag{3.8}$$

where r_{core} is the radius of the CdS nanowire inner core and w is the depletion depth, as illustrated in Figure. 19.

Substituting these boundary conditions stated in equation (3.8) in equation (3.7) that the electric field and potential is both equal to zero at the depletion region edge will yield

$$C_1 = \frac{qN_d}{2\varepsilon\varepsilon_0}(r_{core})^2 \tag{3.9}$$

$$\text{And } C_2 = \frac{qN_d}{4\varepsilon\varepsilon_0}(r_{core})^2[1 - 2\,ln(r_{core})]\,. \tag{3.10}$$

Substituting the constants C_1 and C_2 in equation (3.9) and (3.10) yields equation (3.11) which defines the potential [63] as a function of radius,

$$\varphi(r) = \frac{qN_d}{2\varepsilon\varepsilon_0}(r_{core})^2\left[ln\left(\frac{r}{r_{core}}\right) - \frac{r^2}{2{r_{core}}^2} + \frac{1}{2}\right] \tag{3.11}$$

As seen in Figure 19 (b) the potential at $r = R_{total}$ is V_d. The potential drop V_d is the difference between the neutral level φ_0 at the surface and the Fermi level (E_F) inside the bulk which is 40 mV as stated in [64]. Solving for R_{total} by substituting the value of dielectric constant is 8.7 and $N_d = 2\times10^{17}$ cm^{-3} [64] we get R_{total} as 20.44 nm and we know r_{core} is 5.23 nm which is calculated above in Section 3.3.2 after solving equation (3.5). The depletion region width w due to surface states can be calculated as

$w = R_{total} - r_{core} = 20.44 - 5.23 = 15.21$ nm. (3.12)

Also, as seen in Figs. 6 (a) and 6 (b), the radii of the nanowire were 20-30 nm, which is in accordance with the calculated total radius R_{total}.

3.4 PL characterization of the VLS grown CdS nanowires on ITO coated glass

CdS nanowires were also grown using VLS technique with sputtered Au nanoclusters as catalyst. For VLS growth of nanowires, the ITO coated glass substrate were cleaned by soapy water and then ultrasonicating them in acetone for 30 min followed by another 30 min ultrasonication in isopropanol and dried in nitrogen. Gold of 5 nm thickness was sputtered on these cleaned ITO glass substrate to catalyze the growth of nanowires. The CdS nanowires were synthesized in a quartz tube furnace with dual zone furnace heating instrument. CdS powder (~ 0.8 g, 99.999% pure, purchased from Sigma Aldrich) was placed in one heating zone and the ITO glass substrate with the sputtered gold nanoclusters in the second heating zone. 5% hydrogen was used as the transport gas with a flow rate of 100 sccm. The source and sample were heated to 900 and 580 °C, respectively for 1 hour.

The photoluminescence characteristics of the grown CdS nanowires were investigated using a He–Cd laser of wavelength 325 nm and Acton 2500 spectrometer for excitation at room temperature. The PL for the VLS grown nanowires is shown in Figure 20. The PL emission peak for VLS grown nanowires was observed at 510 nm (2.43 eV) as shown in Figure 20, which is close to the band gap of CdS (2.42 eV).

3.5 Polarization studies of CdS nanowires

3.5.1 Introduction

Some nanowire devices use free-standing nanowires and these free-standing nanowires have several attractive properties, including a large variation in the dielectric constant of the surrounding media and a cylindrical, strongly confining potential for both electrons and holes which leads to polarization anisotropy. This property of polarization anisotropy is employed here to demonstrate a possibility of creating polarization sensitive nanoscale photo detectors that can be useful in optical switches, polarizers, and high resolution detectors [26]. InP nanowires are mostly being used as polarizers due to its high dielectric constant of 12.4. Also, CdS has a high dielectric constant of 8.7-9.25, which can also be used as a polarizer. Polarizing properties of CdS nanowires were investigated and studied.

The polarization anisotropy in PL measurements between the free standing nanowires and its surrounding environment may be modeled by treating the nanowire as an infinitely long dielectric cylinder in a vacuum, since the wavelength of the exciting light is much greater than the wire diameter. When the incident field is polarized parallel to the cylinder, the electric field inside the cylinder is not reduced. But, when polarized perpendicular to the cylinder, the electric field amplitude is attenuated [26, 65] according to (3.13)

$$E_i = \frac{2\varepsilon_0}{\varepsilon+\varepsilon_0} E_e \tag{3.13}$$

where E_i is the electric field inside the cylinder, E_e the excitation field, and ε is the dielectric constant of the cylinder and ε_0 is the dielectric constant of the surrounding. For $\varepsilon > \varepsilon_0$, the probability of optical transitions in a nanowire varies with light polarization,

resulting in greater values for light with polarization parallel to the nanowire axis whereas the incident light creates an electric field of high frequency in the nanowire in the direction of polarization parallel to the nanowire axis. These polarizations have a strong dependence on the absorption coefficient *k* on the light polarization for a system of parallel wires.

Due to the dielectric constant difference between the nanowires and it's surrounding, it demonstrates polarization anisotropy in photoluminescence (PL) measurements. The PL spectra can be recorded from a number of individual wires as a function of excitation or emission polarization [66]. The polarization ratio is given by equation (3.15):

$$\rho = \frac{I_{||} - I_{\perp}}{I_{||} + I_{\perp}} \tag{3.15}$$

where the intensities parallel ($I_{||}$) and perpendicular ($I_{\perp}$) to the wire can be measured with PL measurements at different angles of orientation. The anisotropy in the photoluminescence when a nanowire array is excited with a beam polarized parallel and perpendicular to its long axis has been explained theoretically by Ruda and Shik [65]. They considered an array of dipoles randomly oriented in a dielectric cylinder and computed the Poynting vector outside the cylinder resulting from the incoherent dipole emission. Ruda and Shik [65] found that under this assumption the anisotropy contrast of the emission is given by

$$\frac{I_{||}}{I_{\perp}} = \frac{(\varepsilon+\varepsilon_0)^2+2\varepsilon_0{}^2}{6\varepsilon_0{}^2} \tag{3.16}$$

The mixing of valence bands due to quantum confinement causes polarization anisotropy in quantum wires. This quantum mechanical effect results in smaller polarization ratios ($\rho < 0.60$), which are reported in [67-69]. The large polarization response is because of the large dielectric contrast mainly between the nanowire and its air or vacuum surroundings.

To summarize, the nanowire is modeled as an infinite dielectric cylinder in a vacuum with the light polarizations causing the electric fields. Electric field intensities calculated using Maxwell's equations implies that the field is strongly attenuated inside the nanowire for the perpendicular polarization, $E_{\perp}$ whereas the field inside the nanowire is unaffected for the parallel polarization, $E_{||}$.

3.5.2 Experimental Set up

To study the polarization anisotropy, PL studies were performed with the continuous wave He-Cd laser of wavelength 441 nm laser for parallel and perpendicular polarization with two orientations of the sample having light propagating parallel to the nanowire axis in one orientation as shown in Figure 21 and light propagating perpendicular to the nanowire axis in other orientation as shown in Figure 22. The PL was recorded at room temperature using He-Cd laser of wavelength 441 nm and Acton 2500i spectrometer. The polarization filter used was LPVISE100 purchased from Thor labs Inc.

PL intensity was recorded for parallel and perpendicular polarization with two orientations of the sample having light propagating parallel to the nanowire axis in one orientation and light propagating perpendicular to the nanowire axis in other orientation.

3.5.3 Polarization experiment results

CdS nanowires were grown in anodized aluminum sheet metal of thickness of 500 µm. The nanopores in the Al metal sheet were prepared using two-step anodization process as explained in Section 2.3.1. PL intensities were recorded for parallel and perpendicular polarization with two orientations of the sample as shown in Figures 21

and 22. The PL with and without the polarization filter for parallel and perpendicular polarization is shown in Figure 23. Therefore, the measured polarization ratio ρ given by equation (3.15) by taking the intensity values from Figure 23 is 0.80.

The calculated PL ratio using equation (3.16) is 0.78 by taking dielectric constant of CdS as 8.7 [70]. The measured PL ratio, which is 0.80 - 0.85 is in agreement with our calculated PL ratio 0.78.

These CdS nanowires array which was grown in AAO template for its use in polarizing devices and photodetectors. Nanowire photodetectors can be used as optical switches using its polarization anisotropy properties. The polarization properties of the CdS nanowires were investigated for its use in polarization sensitive optoelectronic devices. Polarization-sensitive measurements reveal a striking anisotropy in the PL intensity recorded parallel and perpendicular to the long axis of a nanowire. The measured PL ratio ρ is around 0.80-0.85 that shows very good polarization anisotropy for CdS nanowires.

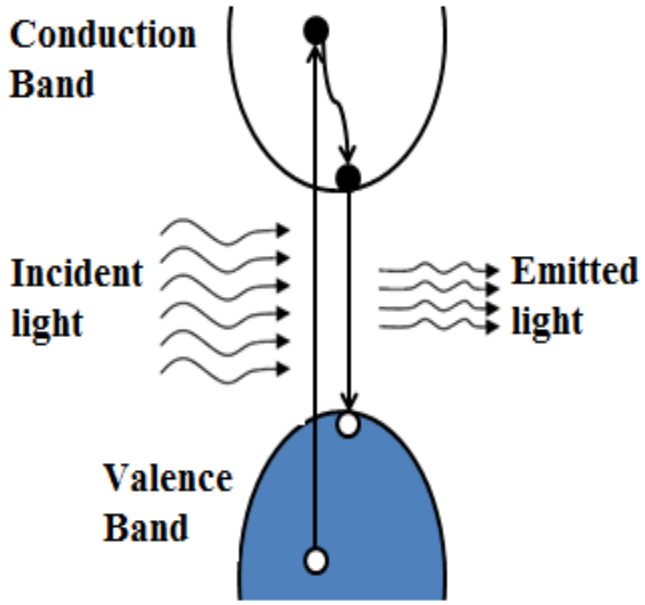

Figure 15: Schematic explaining PL process.

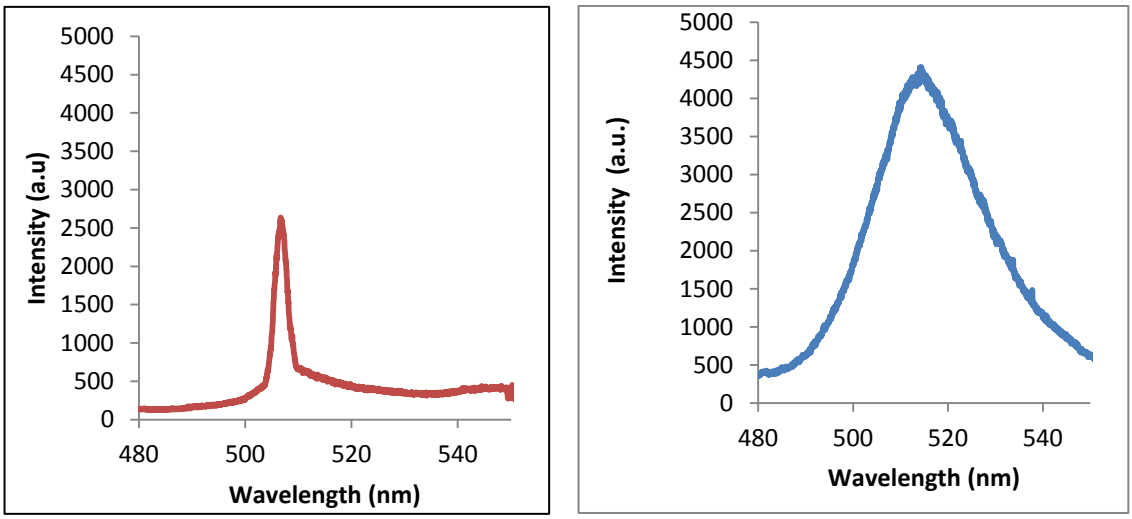

(a) (b)

Figure 16: PL spectra of (a) as grown and (b) annealed CdS nanowires with peak at 506 nm (2.44 eV) and 514 nm (2.41 eV), respectively.

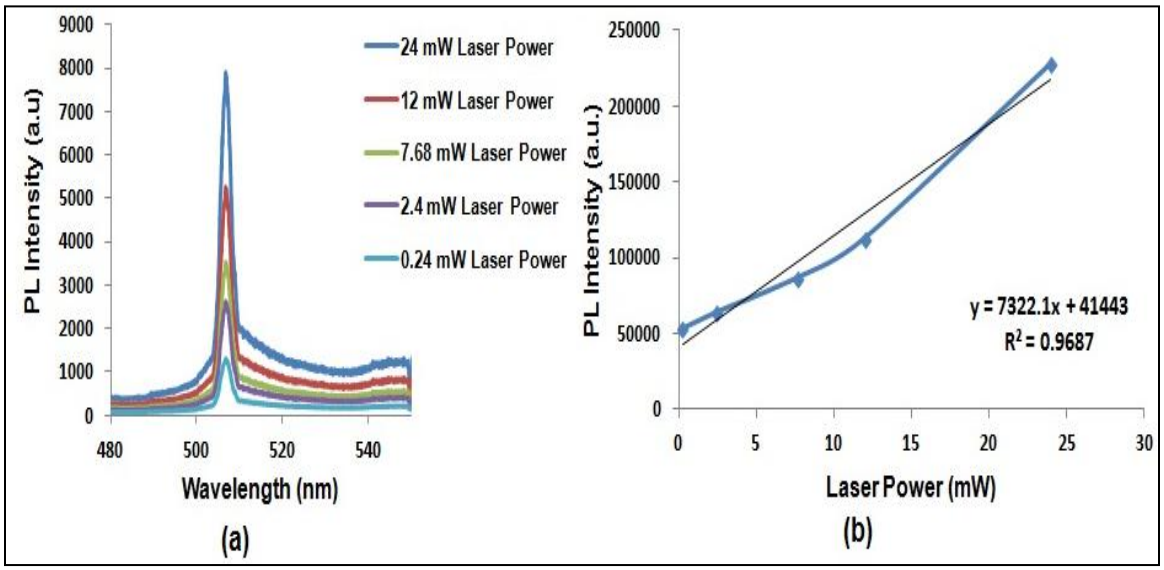

Figure 17: (a) PL spectra of CdS nanowires with different laser excitation power using neutral density filters before annealing (b) PL intensity area variation vs. different laser excitation power using neutral density filters before annealing.

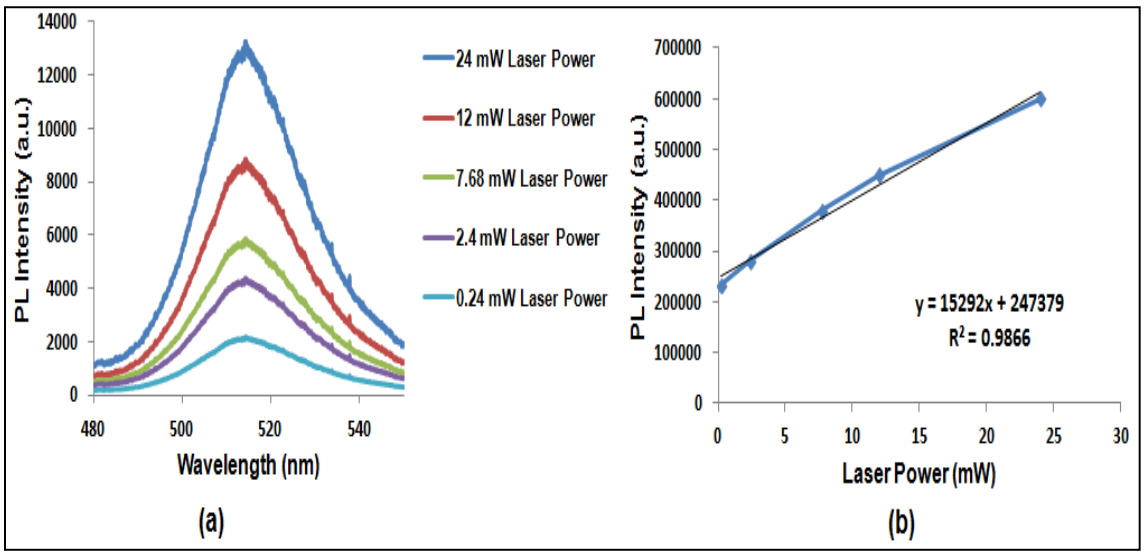

Figure 18: (a) PL spectra of CdS nanowires with different laser excitation power using neutral density filters after annealing (b) PL intensity area variation vs. different laser excitation power using neutral density filters after annealing.

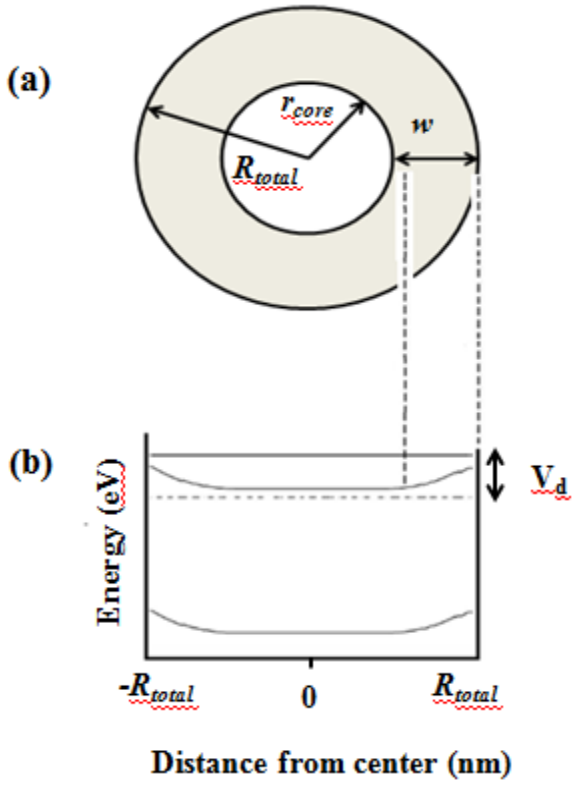

Figure 19: (a) Cross section of nanowire (b) band diagram of CdS nanowire with depletion region of width w due to surface states.

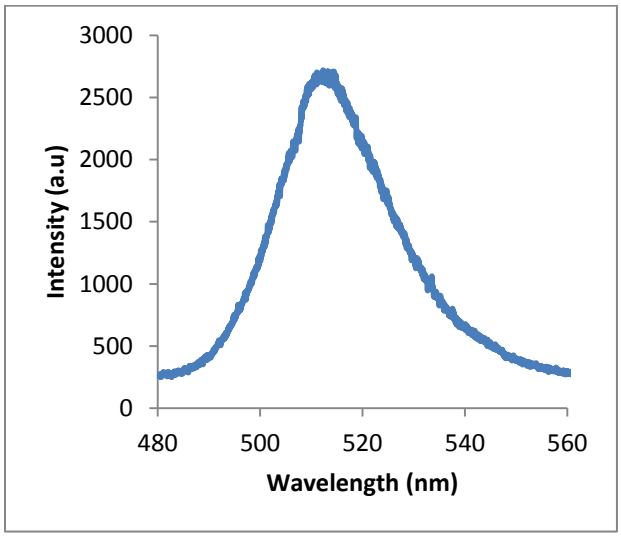

Figure 20: PL spectra of VLS grown nanowires on ITO coated glass substrate at room temperature.

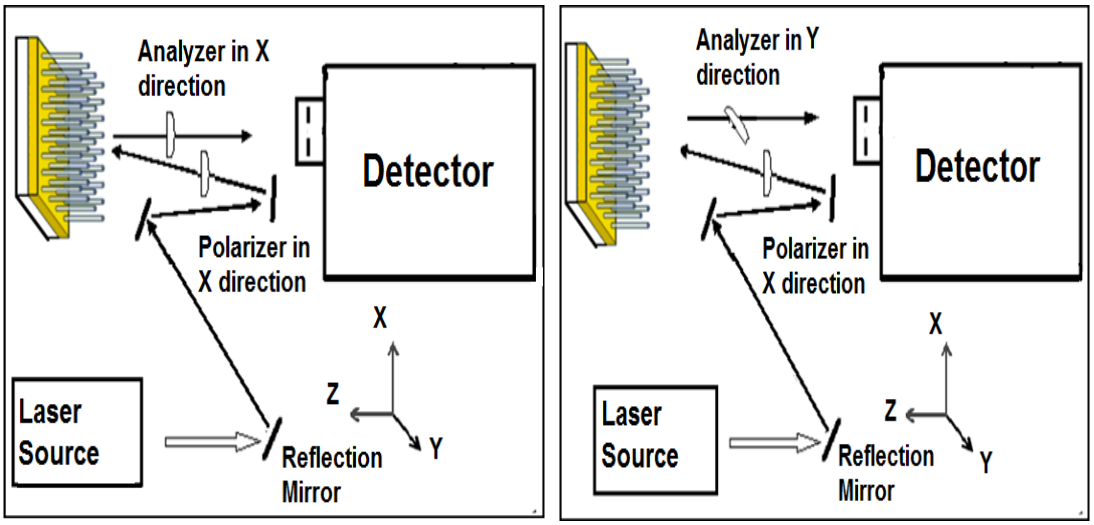

Figure 21: Parallel and perpendicular polarization with light propagating parallel to the nanowire axis.

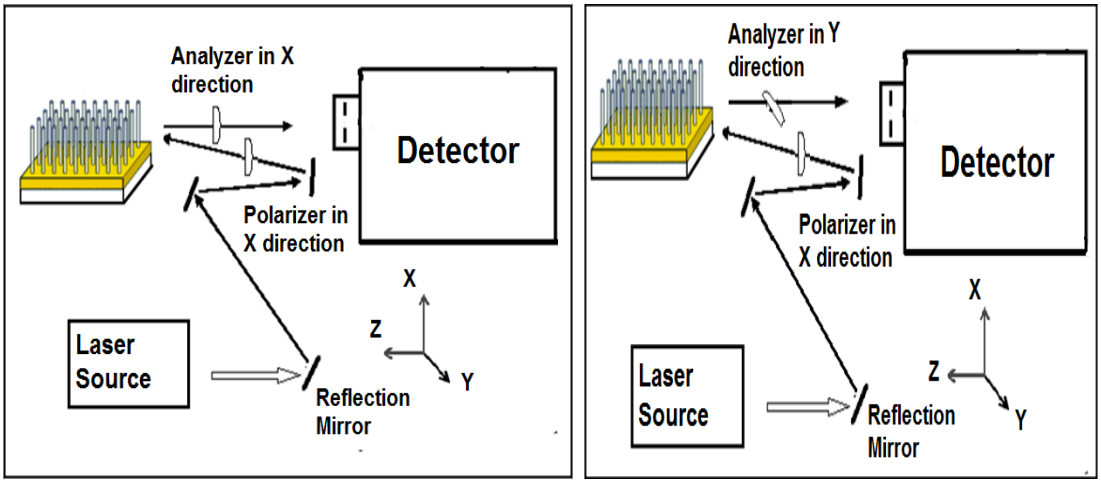

Figure 22: Parallel and perpendicular polarization with light propagating perpendicular to the nanowire axis.

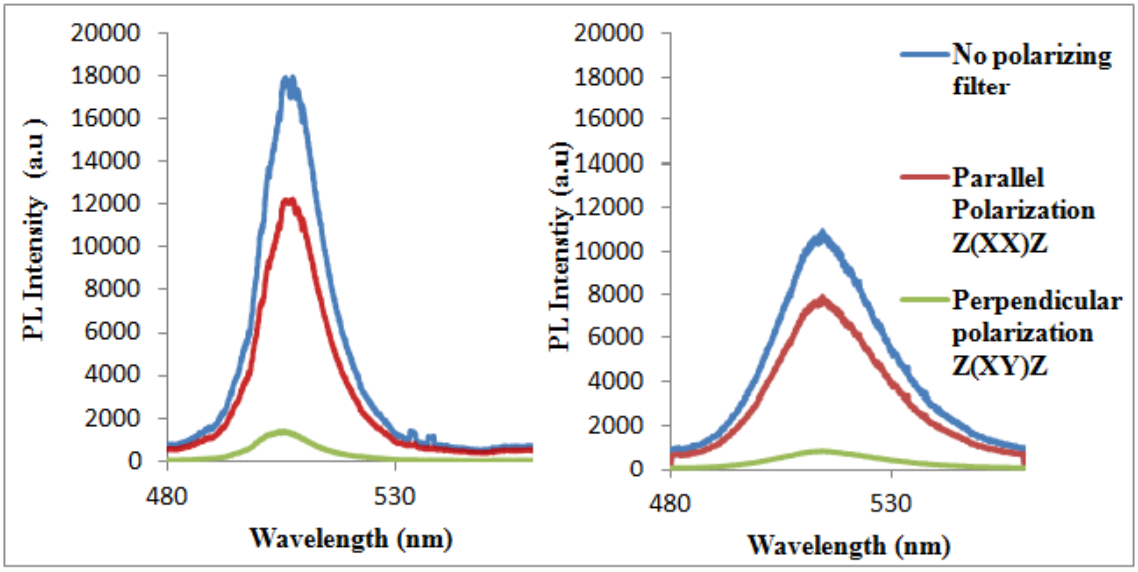

Figure 23: (a) PL peak intensity variation measured when light is propagating along Z but perpendicular to the length of the nanowire. (b) PL peak intensity variation measured when light is propagating along the length of the nanowire along Z. The measured PL ratio is 0.80.

Chapter 4 Raman spectral studies of CdS nanowires

Raman spectroscopy was performed to probe the vibrational and phononic structure of the grown CdS nanowires. In this chapter, Raman spectral results of electrodeposited grown nanowires on ITO coated glass and alumina template are discussed in Section 4.2 and 4.3 respectively. Raman spectroscopy results were explained for the VLS grown nanowires in Section 4.4 and the two different growth mechanisms for VLS grown and electrodeposited growth was compared. Depending upon the quality of nanowires, generally the second and third harmonics of longitudinal optical phonon modes are not observed. The electrodeposited and VLS grown nanowires were of better quality and the 2 LO and 3 LO peaks were visible in the Raman spectrum and these experimental details are all explained in Section 4.5. Optical properties such as phonon modes of CdS nanowires are strongly affected by crystallinity, size confinement, strain, and exciton longitudinal optical (LO) phonon interaction. It's important to investigate the polarization anisotropy and the changes incurred in all the phonon modes due to strain, LO phonon interaction and optical phonon frequencies of crystal structure. These CdS nanowires belong to the hexagonal wurtzite structured of the space group C_6v^4 [70, 71]. If N is the number of atoms in a unit cell then for wurtzite structure, N is 4 and the total modes which can be observed will be 3N, i.e. 12: one longitudinal acoustic (LA) mode, two transverse acoustic (TA) mode, three LO and six transverse optical (TO) modes. But for this space group of C_6v^4, the Raman active modes are $1A_1 + 1E_1 + 2E_2$ (E_2^H and E_2^L), while $2B_2$ modes are silent [70]. Because of the noncentrosymmetric wurtzite structure, both A1 and E1 modes split into longitudinal optical (LO) and transverse optical (TO) components. The Raman characteristics of these CdS nanowires are discussed for

different polarization and orientations in Section 4.5. The electron phonon coupling constant was computed for the CdS nanowires and discussed in Section 4.6.

4.1 Introduction to Raman spectroscopy

Raman spectroscopy was named after Sir C. V. Raman in 1928, who discovered the phenomenon of Raman scattering effect by means of sunlight. It is a spectroscopic technique, which can be used to investigate vibrational, rotational, and other frequency modes of a material [72, 73]. The Raman effect occurs when the incident laser radiation interacts with the bonds of the molecule vibrations and its polarizable electron density. The laser light interacts with molecular vibrations of the lattice resulting in creation or annihilation of phonons, causing the energy of the laser photons to decrease or increase. The shift or change in the energy gives information about the vibrational modes of the material. This spectroscopy is a very useful technique, which is used to probe the structure of the material and its vibrational properties and study its phonon frequency modes. In a Raman scattering experiment, light of a known wavelength and polarization is scattered from the sample. Raman scattered light gets shifted with respect to the excitation frequency, due to the molecular vibrations in the sample. Therefore, the "Raman shift" is caused due to the intrinsic properties of the sample like vibration and frequency modes of the crystal.

In spontaneous Raman scattering, which is a form of inelastic light scattering, a photon of a specific wavelength excites the molecule in either the ground state or an excited state as shown in Figure 24. This excitation results in the emission or scattering of a photon inelastically. The resulting inelastically scattered photon, which is emitted, can be either of higher or lower energy than the incoming photon energy of frequency ν_0. The

inelastic scattering in which the energy is higher is referred to as Anti-Stokes scattering having frequency of $\nu_0 + \nu_m$ where ν_m is the frequency with which the molecules are vibrating. On the other hand, the inelastic scattering in which the energy is lower having frequency of $\nu_0 - \nu_m$ is referred to as Stokes scattering. Therefore, when phonons are emitted, it is called Stokes scattering; when phonons are absorbed, it is called Anti-Stokes scattering as shown in Figure 24.

The rotational and vibrational energy states of the molecule change after the interaction of the incoming photon with the molecule, causing a shift in the emitted photon's frequency away from the excitation wavelength of laser in Raman scattering. This Raman shift is measured in wave number, which is the inverse of wavelength. The relationship between the wavelength and the shift in wave number $\Delta\omega$ in the Raman spectrum is given by the following formula:

$$\Delta\omega = \frac{1}{\lambda_i} - \frac{1}{\lambda_f} \tag{4.1}$$

where $\Delta\omega$ is the Raman shift usually expressed in wave number cm^{-1}, λ_i is the initial excitation wavelength, and λ_f is the final Raman spectrum wavelength.

In Raman scattering experiment, a sample is illuminated with a laser beam of known wavelength. The incident laser is scattered from the sample. Elastic scattered radiation at the wavelength is called elastic Rayleigh scattering (in which, the scattered light has the same frequency ν_0 as that of the incident light photon). Either a notch filter or a band pass filter filters out Rayleigh scattering and the detector collects rest of the light for analysis. Spontaneous Raman scattering is very weak as compared to the elastic Rayleigh scattered laser light due to which it is difficult to separate the weak inelastically Raman scattered light from the strong Rayleigh scattered laser light. Also, since the scattered light

frequency is very close to the frequency of the incident light, therefore the bandwidth of the laser source should be very narrow and one has to use notch or edge filters to filter out the laser light from the scattered signal.

4.2 Raman spectral studies of CdS nanowires grown using electrodeposition on ITO coated glass substrate

The Raman spectrum was recorded using Ar^+ ion laser of 514 nm wavelength of the electrodeposited grown CdS nanowires on ITO coated glass substrate using Renishaw Ramascope 2000 Raman instrument. The Raman characteristics of these nanowires before and after annealing are in Figure 25. Raman peaks were observed at 302 cm^{-1}, 603 cm^{-1} and 906 cm^{-1} corresponding to the longitudinal optical phonon (LO) modes 1 LO, 2 LO and 3 LO, respectively, analogous to the peaks of pure CdS crystalline structure [23, 74]. The 1 LO, 2 LO and 3 LO peaks for bulk CdS are usually at 300 cm^{-1}, 600 cm^{-1} and 900 cm^{-1} as reported in [23].

Strong 1 LO, 2 LO and 3 LO peaks were observed within 35 meV making it slightly similar to the electronics and phononic structure of the CdS material. The second and third harmonics of LO order modes are not observed usually in bulk material. However, the optical properties of nanostructures are highly affected by crystallinity of the structure, confinement, strain, and also the exciton longitudinal optical (LO) phonon interaction [49, 75, 76]. There are no quantum confinement effects in the LO phonon energies of CdS NWs with diameters greater than 50 nm. The phonon energies of CdS nanowires are mostly affected by lattice strain [77, 78]. Surface tension during the growth of CdS NWs causes lattice strain which results in a significant increase of the LO phonon energy.

4.3 Raman scattering in CdS nanowires grown using electrodeposition in anodized aluminum sheet

In this section, the Raman scattering in CdS nanowires grown via DC electrodeposition in anodized alumina sheet is explained. The Raman characteristics of these CdS nanowires are shown in Figure 26.

Strong peaks of 1 LO, 2 LO and 3 LO frequencies for CdS nanowires grown in anodized alumina sheet were observed at 305, 606, 909 cm^{-1}. However, the 1 LO, 2 LO and 3 LO peaks for bulk CdS are usually at 300 cm^{-1}, 600 cm^{-1} and 900 cm^{-1} as reported in [23]. It has been reported that the 1 LO phonon energy of CdS NWs was shifted upward by 5 cm^{-1} compared to that of bulk CdS, suggesting that the lattice compressive strain of the *c* axis is induced during the NW growth in the anodized alumina matrix [77, 78]. Also, as seen in Figure 10, the diameters of the CdS NWs were about 20-25 nm where quantum confinement can be observed. Also, strain can be induced during the growth of CdS nanowires which influences the phonon energies of CdS nanowires [79]. However, the energy separation was 34 meV between the peaks of the 1 LO and 2 LO peak, which is in good agreement to the electronics and phononic structure of CdS but there is a slight shift in the phonon modes as compared to the bulk material. The phonon energies of the CdS NWs have been shifted a little from the bulk values due to the lattice compressive strain, electron phonon coupling interaction effects in the grown CdS nanowires.

4.4 Raman scattering in CdS nanowires grown via VLS growth and its comparison with electrodeposited growth of CdS nanowires

To study the vibrational and crystalline properties of the VLS grown CdS nanowires were performed. The Raman characteristics of these nanowires for VLS grown nanowires is shown in Figure 27. Raman peaks were observed at 302 cm^{-1}, 603 cm^{-1} and 906 cm^{-1} corresponding to the longitudinal optical phonon (LO) modes 1 LO, 2 LO and 3 LO, respectively, analogous to the peaks of pure CdS crystalline structure.

As compared to the electrodeposited growth of CdS nanowires on ITO coated glass substrate, VLS grown CdS nanowires were of better quality since the Raman response for VLS grown was superior as seen in Figure 28. The electrodeposited nanowires on ITO coated glass substrates were not as good because of the incomplete removal of barrier layer of the AAO template growth which reduces the filling of nanopores in the AAO template and also some traces of aluminum template were present even after the removal of AAO template in NaOH solution.

4.5 Raman characteristics of CdS nanowire array grown in anodized alumina sheet in different orientations and polarizations

To study the polarization and anisotropy present in the CdS nanowires, Raman characteristics were recorded for two orientations of the sample with light propagating parallel (||) to the nanowire axis in one orientation as shown in Figure 21 and light propagating perpendicular (⊥) to the nanowire axis in other orientation as shown in Figure 22. Raman intensities were recorded for both parallel Z(XX)Z and perpendicular polarization Z(XY)Z of the laser. All the notations described in the thesis are of the type" Z(XY)Z, where the directions inside the parentheses signify the polarizations of the

incident and scattered beams, respectively. The directions preceding and following outside the parentheses indicate the respective directions of the incident beam and scattered beams [80].

The reported phonon frequencies observed for CdS wurtzite crystal in [80] are given in Table II. Figure 29 shows the Raman spectra of CdS nanowires using the polarization filter when light is propagating along the length of the wire along Z. Peaks in intensity were observed at A1 (TO) at 235 cm^{-1} for parallel polarization and at E2 at 258 cm^{-1} for perpendicular polarization along with 1 LO, 2 LO at 309 and 607 cm^{-1} respectively. These peaks are in accordance with the CdS values of transverse and longitudinal mode peaks [70]. Also, Raman spectral studies were performed with the polarization filter when light was propagating perpendicular to the length of the wire. The peaks were found at peak at E1 (transverse) at 247 cm^{-1} for parallel polarization of incident light as shown Figure 30 (a) and at quasi A1 (transverse) at 240 cm^{-1} for perpendicular polarization as shown in Figure 30 (b) along with 1 LO, 2 LO at 310 and 604 cm^{-1} respectively. The observed peaks were slightly different for CdS NWs than the reported frequencies of CdS bulk crystals given in Table II. The 1 LO phonon energy has been observed more for CdS NWs as compared to CdS bulk. The same behavior with the increase in 1 LO phonon energy was also reported in Refs. [77, 78]. Also, good crystallinity enhances multiphonon responses due to well-defined phonons in the material. The optical properties of CdS nanowires are also influenced greatly by exciton longitudinal optical (LO) phonon interaction. The exciton optical phonon interaction for these nanowires is also studied in details and is explained in the following section 4.6.

Table II: Optical phonon modes of wurtzite CdS crystal. All the modes are expressed in cm^{-1}.

Optical mode	CdS
E_2	43
E_2	256
A_1	234
Quasi- A_1 (transverse)	240
Quasi- E_1 (transverse)	239
E_1 (transverse)	243
A_1 (longitudinal)	305
Quasi- A_1 (longitudinal)	306
Quasi- E_1 (longitudinal)	306
E_1 (longitudinal)	307

.

4.6 Exciton longitudinal optical (LO) phonon interaction in CdS nanowires

In this section, we explore the electron phonon interaction in the CdS wurtzite nanowire. As seen in the previous discussion, the phonon energies of the grown CdS nanowires are quite dependent on the strain, lattice contraction and also the electron-phonon interactions. The electron phonon interactions of the grown CdS nanowires were studied. Since the grown CdS nanowires belong to wurtzite crystals, which have a different unit-cell structure and lower symmetry as compared to zinc-blende crystals, phonon dynamics and carrier-phonon interactions in this material system are quite different.

The lattice vibrations can be described in terms of orientation with respect to the *c* axis, the phonon wave vector **q**, the electric field **E**, and the polarization **P** due to the optical anisotropy and lower symmetry of uniaxial crystals [71]. The lattice vibrations are divided into two groups of phonons: ordinary phonons for which **E** and **P** are both perpendicular to **q** and the *c* axis and extraordinary phonons for which the frequency of

the phonon is dependent upon the angle between the phonon wave vector and the *c* axis given by θ.

Loudon in Ref [71] has explained the macroscopic equations of uniaxial crystals by describing the dielectric constant with the direction parallel to the *c* axis, as $\varepsilon_{||}$ and another dielectric constant associated with the direction perpendicular to the *c* axis, as $\varepsilon_{\perp}$, and the phonon frequencies of the extraordinary phonons satisfy the following relation [81] given by

$$\varepsilon_{\perp} sin^2\theta + \varepsilon_{||}\ cos^2\theta = 0 \tag{4.2}$$

The direction-dependent dielectric functions are given by the following equations (4.3) and (4.4)

$$\varepsilon_{\perp}(\omega) = \varepsilon_{\perp}{}^{\infty} \frac{\omega^2 - \omega_{\perp L}^2}{\omega^2 - \omega_{\perp}^2} \tag{4.3}$$

$$\varepsilon_{||}(\omega) = \varepsilon_{||}{}^{\infty} \frac{\omega^2 - \omega_{||L}^2}{\omega^2 - \omega_{||}^2} \tag{4.4}$$

Therefore, the static direction-dependent dielectric functions after substituting $\omega = 0$ in (4.3) and (4.4) gives the following equations

$$\varepsilon_{\perp}(0) = \varepsilon_{\perp}{}^{\infty} \frac{\omega_{\perp L}^2}{\omega_{\perp}^2} \tag{4.5}$$

$$\varepsilon_{||}(0) = \varepsilon_{||}{}^{\infty} \frac{\omega_{||L}^2}{\omega_{||}^2} \tag{4.6}$$

For wurtzite-based crystals such as GaN, ZnO, CdS, and CdSe materials, the equations according to Loudon's model for longitudinal and transverse modes satisfy the following equations (4.7) and (4.8) respectively:

$$\omega_{\perp L}^2 sin^2\theta + \omega_{||L}^2\ cos^2\theta = \omega_{LO}^2 \tag{4.7}$$

$$\omega_{\perp}^{2} cos^{2}\theta + \omega_{||}^{2}\ sin^{2}\theta = \omega_{\mathrm{TO}}^{2} \quad (4.8)$$

Two of the optical modes *A*1 and *E*1 modes at split into LO and TO components for wurtzite crystals. These phonons exhibit mixed polarization for an arbitrary θ. For θ =0, in pure *A*1 (LO) mode, two positive ions of the unit cell of wurtzite structure are displaced along the *c* axis, and the two negative ions are displaced along the *c* axis in the opposite direction. Therefore, a polarization **P** directed along the *c* axis is caused in *A*1 (LO) mode. However, for pure *E*1 (TO) mode, two positive ions are displaced perpendicular to the *c* axis, and the two negative ions are displaced in the opposite direction, perpendicular to the *c* axis. Therefore, the *E*1 (TO) mode causes a polarization **P** in the direction perpendicular to *c* axis. For θ = 0, both E1 and A1 modes are infrared active and have Frohlich interactions. The modes are *A*1 (TO) and the *E*1 (LO) modes for 0° and 90°, respectively. The optical modes are mixed and do not have purely LO or TO character for values of θ between 0° and 90° and these associated Frohlich interactions for different modes causes strong carrier-polar-optical-phonon interactions.

An electrical field is produced by a long wavelength LO phonon in a polar semiconductor which is given by E(r) [82].

$$E(r) = -4\pi F \sum_{q} \boldsymbol{P}\ a_{q}\, e^{i\boldsymbol{q}.\boldsymbol{r}} +\ {a_{q}}^{+} e^{-i\boldsymbol{q}.\boldsymbol{r}}] \quad (4.9)$$

where q is the phonon vector, a_q and ${a_q}^{+}$ are the phonon annihilation and creation operators, respectively, P the polarization vector, and Frohlich constant F is given by [82]

$$\mathrm{F} = \frac{\hbar\omega_{LO}}{8\pi \mathrm{V}} \left(\frac{1}{\varepsilon_{\infty}} - \frac{1}{\varepsilon_{0}}\right)]^{1/2} \frac{(\mathrm{m_e^*}+\mathrm{m_h^*})}{2\hbar^{3}\omega_{LO}}]^{1/4}\ ] \quad (4.10)$$

The larger size of an exciton makes the phonon highly polarizable, so the LO phonons couple strongly to the excitons. The exciton–LO phonon coupling Hamiltonian *H* is given by the following equation [83]

$$H = \sum_q - e\phi(q)\, exp(i\, q.r)\, (a_q\ +\ a^*_{-q}) \tag{4.11}$$

where $\phi(\mathrm{q})$ is the Fourier transform of $\phi(\mathrm{r})$, a_q and $a_q{}^+$ are the phonon annihilation and creation operators, respectively.

Therefore, the normalized Hamiltonian function is given as follows [81]:

$$H = \sum_q \left[\frac{4\pi e^2 \hbar V^{-1}}{\frac{\partial}{\partial\omega}\left[\varepsilon_\perp(\omega) sin^2\theta + \varepsilon_{||}(\omega) cos^2\theta\right]}\right]^{\frac{1}{2}} \frac{1}{\mathrm{q}} \exp(i\ \mathrm{q}.\mathrm{r})\left(\mathrm{a_q}\ +\ \mathrm{a^*_{-q}}\right)$$

$$= \sum_q \sqrt{\frac{2\pi e^2 \hbar}{V\omega}} \frac{(\omega_\perp^2 - \omega^2)\left(\omega_{||}^2 - \omega^2\right)}{\left[\left(\varepsilon_\perp^0 - \varepsilon_\perp^\infty\right)\omega_\perp^2(\omega_{||}^2-\omega^2)^2 sin^2(\theta) + \left(\varepsilon_{||}^0 - \varepsilon_{||}^\infty\right)\omega_{||}^2(\omega_\perp^2-\omega^2)^2 cos^2(\theta)\right]^{1/2}} e^{iqr}\left(\mathrm{a_q}\ +\ \mathrm{a^*_{-q}}\right) \tag{4.12}$$

After solving the equation (4.12) the electron phonon coupling constant for the grown CdS nanowires were calculated using MATLAB and the MATLAB program is given in Appendix A. The electron-phonon coupling constant with respect to various angles θ was computed using equation (4.12) in MATLAB, which is shown in Figure 31. All the values for phonon frequencies were taken from Table II. The crystal volume was calculated by taking the lattice constant from Table I.

It was observed experimentally that the magnitude of Huang Rhys factor, which signifies the electron phonon coupling strength, decreases with the increasing angles of laser polarization. The Huang Rhys factor is the ratio of 2 LO peak with respect to 1 LO peak and is computed from the experimental data of Raman spectrum shown in Figure

34. The electron phonon coupling strength S is estimated by measuring the Raman intensity of the 2 LO phonon with respect to that of the LO phonon [83] where S is the Huang Rhys factor.

According to Franck Condon approximation, the ratio of the second-order and the first-order Raman scattering cross sections approximately equates to where S is the displacement of the harmonic oscillator in the exited state, which can be used to express the coupling strength of the electron to the LO phonon in polar semiconductor materials. The calculation of Huang Rhys factor for the experimental data shown in Figure 34 is given in Table III.

Table III: Huang Rhys factor values computed from experimental data given in Figure 34.

Angle θ in degrees	**Huang Rhys parameter, S**
0	1.1
30	0.88
60	0.78
90	0.67

It has been seen that in the MATLAB calculation results in Figure 32 of electron phonon coupling constant that the decreases with the increasing angle θ which denotes the angle between the long axis of nanowire (**z** axis) and the laser polarization. Experimentally, it was observed as seen in Figure 33 that the Raman response was the best for 0 degree lower angles than the higher angles. It's observed that the Raman intensity is dependent on the angle of laser polarization, the orientation of the nanowires and also the electron phonon interaction in the nanowires.

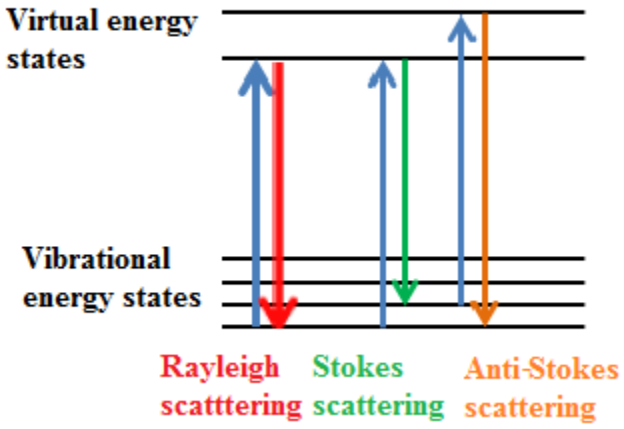

Figure 24: Types of Raman scattering.

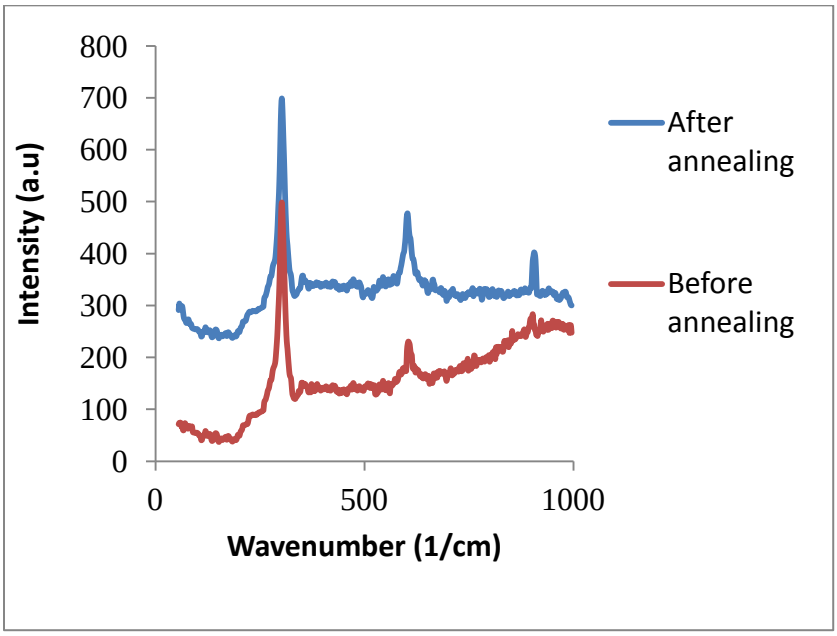

Figure 25: Raman peaks observed at 302, 603, 906 cm^{-1} corresponding to 1 LO, 2 LO and 3 LO respectively of CdS nanowires grown in AAO templates fabricated on ITO coated glass substrate.

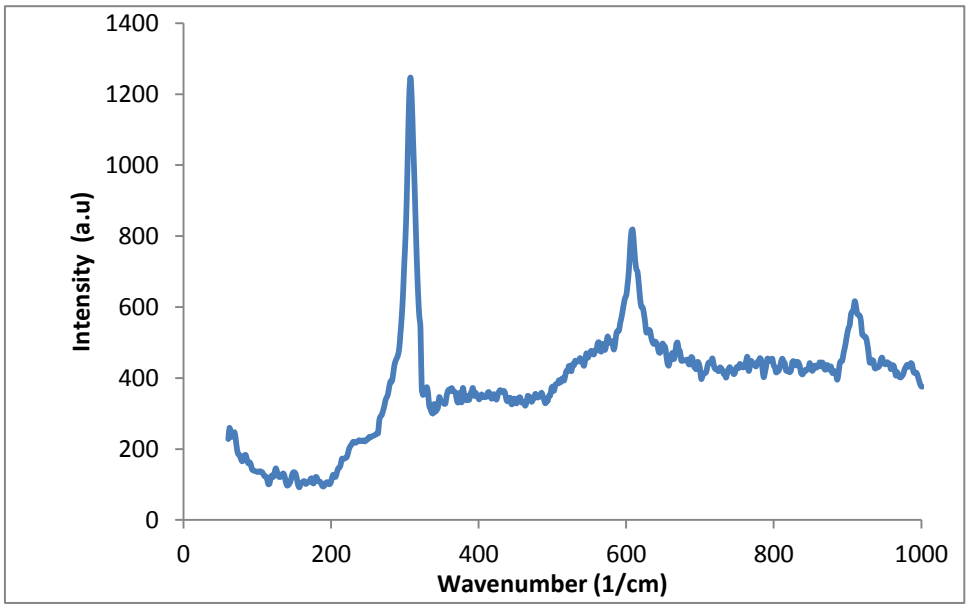

Figure 26: Raman peaks observed at 305, 606, 909 cm^{-1} corresponding to 1 LO, 2 LO and 3 LO of CdS nanowires respectively grown in anodized alumina sheet.

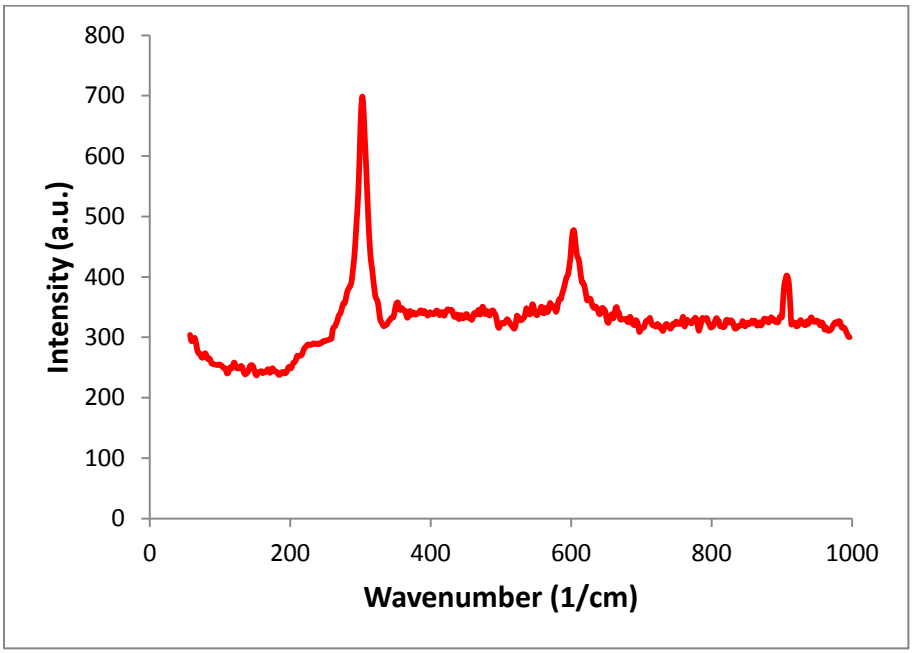

Figure 27: Raman spectra of VLS grown CdS nanowires with peaks at 302 cm^{-1}, 603 cm^{-1} and 906 cm^{-1} corresponding to the longitudinal optical phonon (LO) modes 1 LO, 2 LO and 3 LO, respectively.

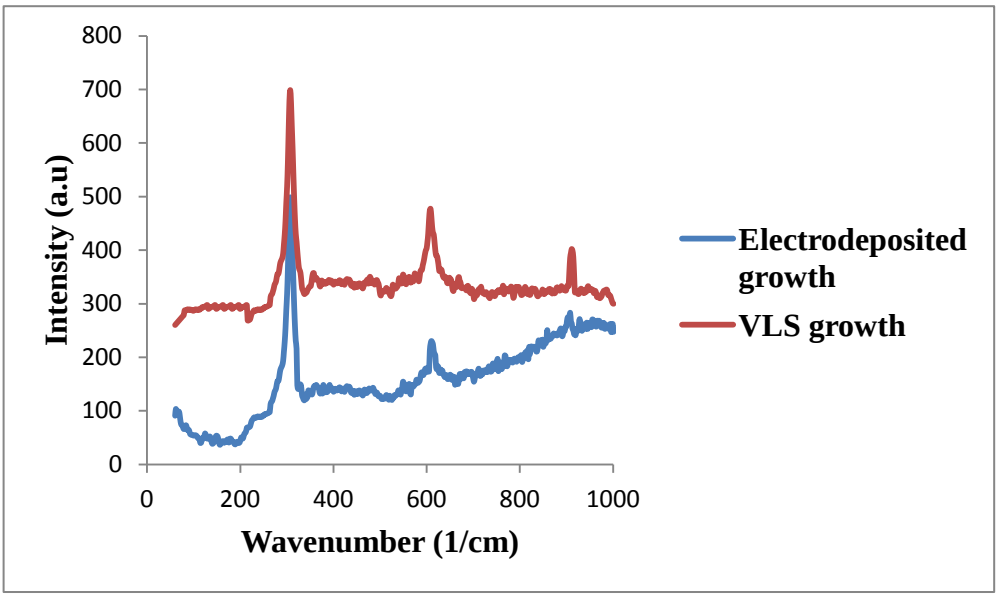

Figure 28: Comparison of Raman spectra of VLS grown and electrodeposited growth of CdS nanowires.

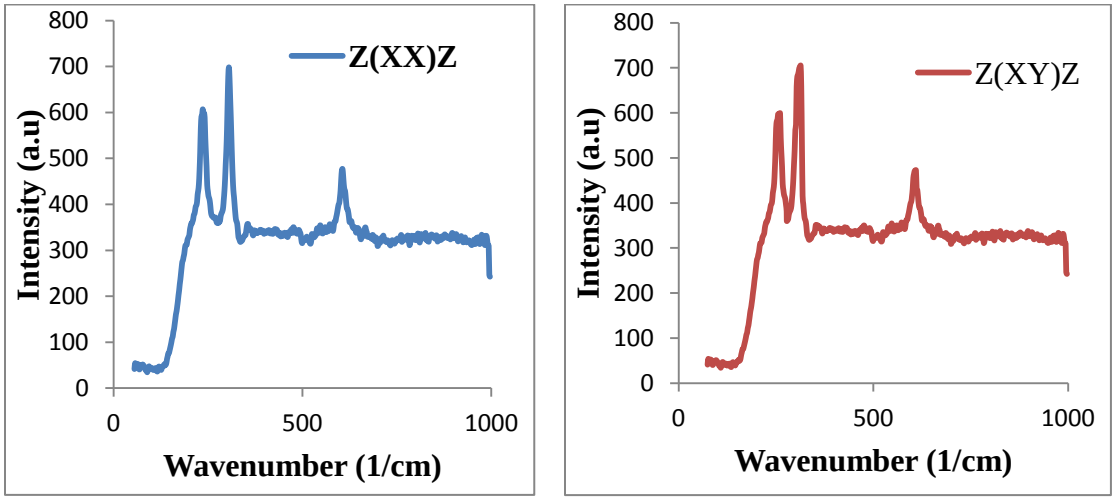

(a) (b)

Figure 29: Raman using the polarization filter with peak at A1 (TO) at 235 cm^{-1} for parallel polarization in (a) and at E2 at 258 cm^{-1} for perpendicular polarization in (b) along with 1 LO, 2 LO at 309 and 607 cm^{-1} respectively when light is propagating along the length of the wire along Z.

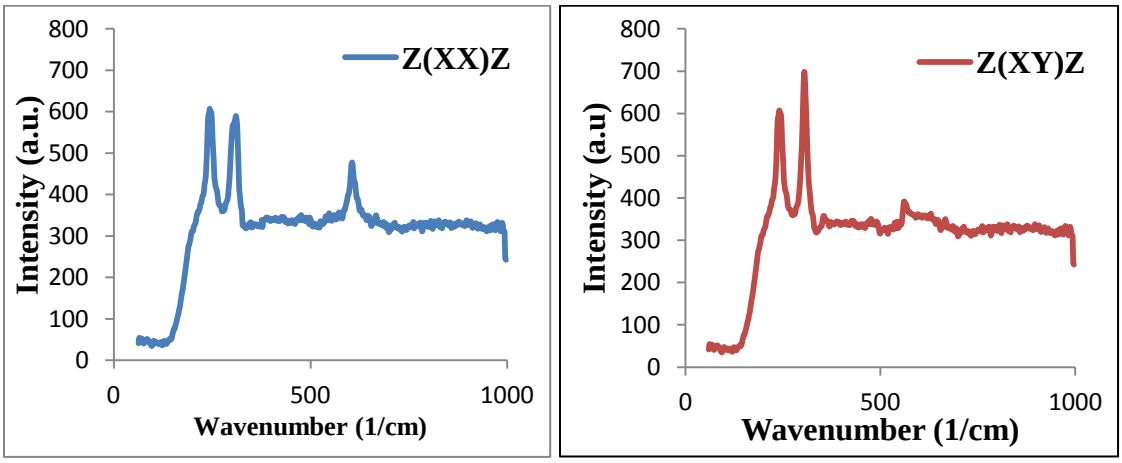

(a) (b)

Figure 30: Raman using the polarization filter with peak at E1 (transverse) at 247 cm^{-1} for parallel polarization in (a) and at quasi A1 (transverse) at 240 cm^{-1} for perpendicular polarization in (b) along with 1 LO, 2 LO at 309 and 607 cm^{-1} respectively when light is propagating along Z but perpendicular to the length of the wire.

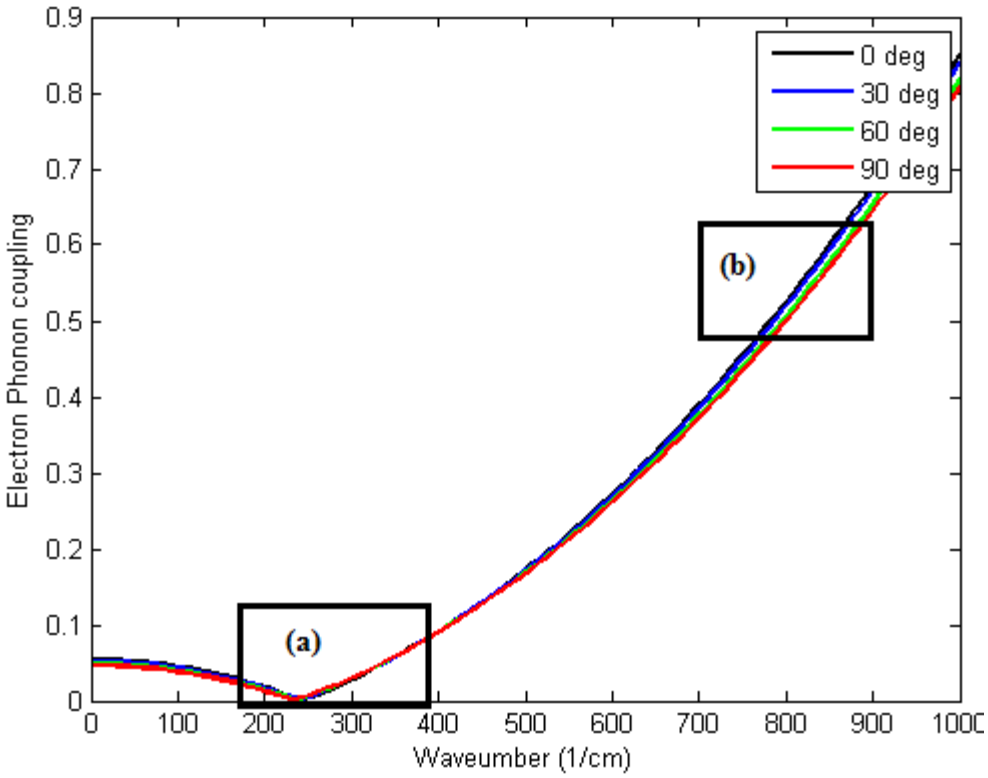

Figure 31: Plot of electron phonon coupling constant for CdS nanowires for different laser polarization angles $\boldsymbol{\theta}$ against wavenumber. Highlighted regions (a) and (b) are zoomed out in Figures 32 and 33 respectively as shown below.

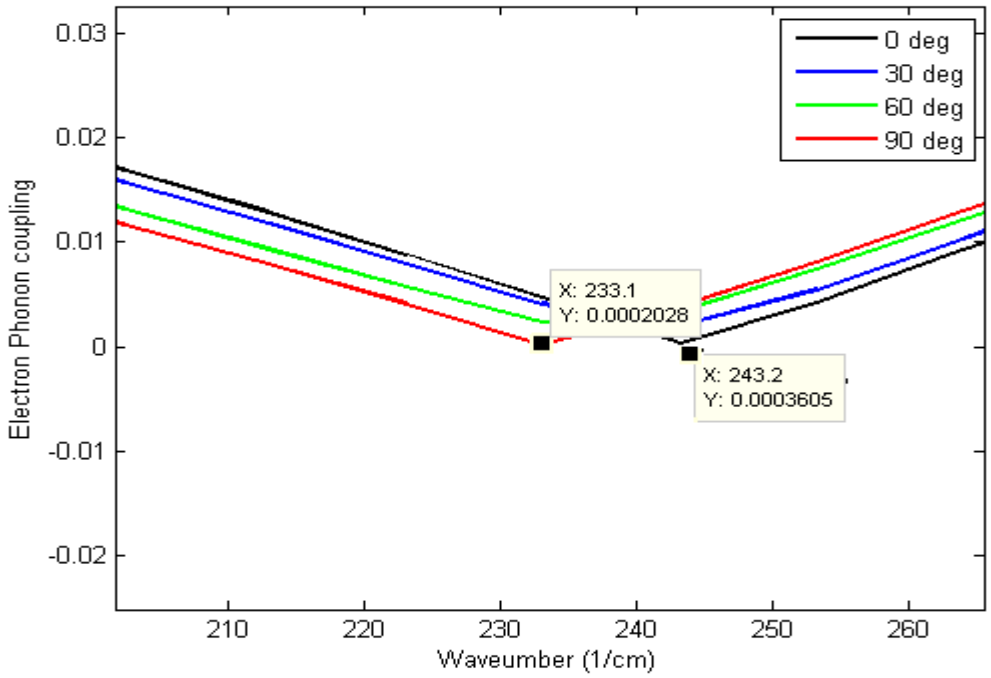

Figure 32: Zoomed version of highlighted region (b) of Figure 31 shows the minima at 233 and 243 cm^{-1}.

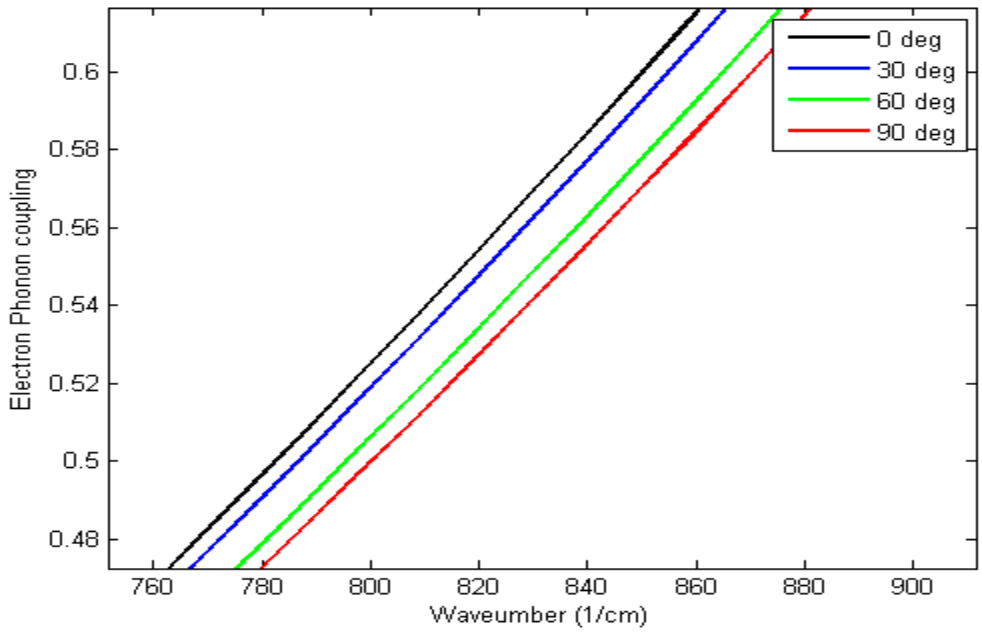

Figure 33: Zoomed version of highlighted region (b) of Figure 31 shows the magnitudes of electron coupling constant decreasing with increasing angle $\boldsymbol{\theta}$.

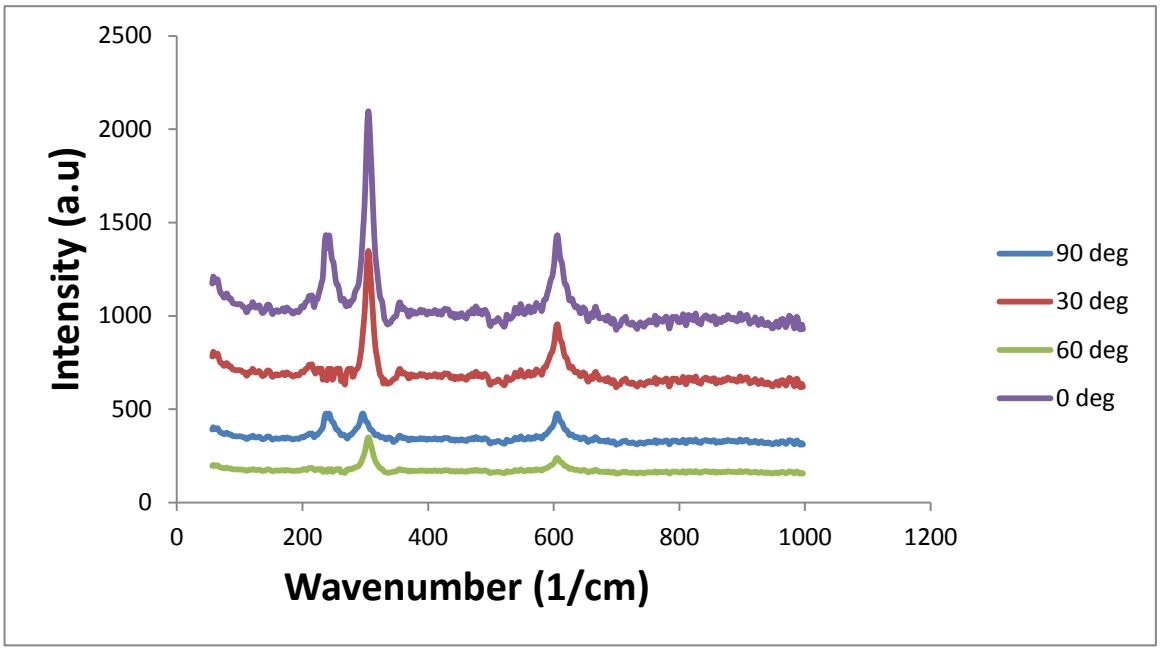

Figure 34: Experimental data of Raman spectrum with different angles. $\boldsymbol{\theta}$ denotes the angle between the long axis of nanowire (z axis) and the laser polarization.

Chapter 5 Investigation of CdS/P3HT Heterojunction

In this chapter, the heterojunction formed between conductive polymer poly (3-hexylthiophene-2, 5-diyl) (P3HT) and CdS nanowires array is investigated for its potential use in photovoltaic applications. Conductive polymer P3HT polymer chemical structure and its electrical transport properties such as mobility for polymer inter-chain and intra-chain conduction is discussed in Section 5.1. The Section 5.2 gives the experimental details about the formation of heterojunction between the CdS nanowire and P3HT. Optical and current voltage characteristics of CdS/P3HT heterojunction are explained in the Section 5.3.

5.1 Introduction

Polymers consist of chains that have repeating units of carbon, hydrogen and other atoms. These repeating units are called as monomers. Typically, these polymers are insulators but in some polymers are conductive due to the charge carrier transport in conjugated polymers. The charge carrier transport is mainly possible due to the presence of π bonds. The p orbitals of carbon atoms in two neighboring repeating units in a conjugated polymer may overlap each other resulting in the formation of two split energy levels as π bonding orbital and a π^* anti-bonding orbital. In a complete chain of polymer these energy levels produce π energy band, which is called the highest occupied molecular orbital (HOMO) and π^* energy band is formed which is called as the lowest unoccupied molecular orbital (LUMO) in an energy band diagram of polymer. HOMO and LUMO orbitals are considered similar to the valence and conduction bands of inorganic semiconductors, respectively [84, 85]. In an intra-chain conduction, the charge

carriers move in the same polymer chain via π bonds. High charge carrier mobility is usually observed in the case of intra-chain conduction when the chain stays as a straight nanowire for high conduction and favorable results for some electronic applications. On other hand, in an inter-chain conduction, the carriers are moving between different chains, and the mobility highly reduces and is very less as compared to the mobility of the intra-chain case [86]. The obtained mobility values tend to be lower in inter-chain conduction than the potential intra-chain mobility if the dominant conduction mechanism in bulk and disordered polymers is inter-chain hopping. Therefore, the conductive polymer takes the shape of nanowires when its spin coated in an array of standing CdS nanowires. CdS nanowires grown on ITO coated glass substrate is used to form a hybrid junction with the conductive polymer poly (3-hexylthiophene-2, 5-diyl) (P3HT).

In these experiments, regioregular poly (3-hexylthiophene-2, 5-diyl) (P3HT): chloroform solution was used as the semiconductor between the n-type CdS nanowire array grown on ITO coated glass substrate. The monomer unit of P3HT is shown in Figure 35.

These CdS NW/P3HT hybrid junctions were characterized optically and electrically to investigate the electronic transport properties for optoelectronic applications.

5.2 Experimental Details

Firstly, the polymer P3HT was dissolved in the chloroform solution with a w/v ratio of 10 mg/ml. The solution was heated to 100 °C to dissolve the polymer completely and then the solution was drop cast on the grown CdS nanowire sample on ITO coated glass substrate to form the hybrid structure. These samples were optically characterized by performing photoluminescence experiments. Also, the top contact (Ag) was formed

using silver paint to study the current voltage properties of ITO/CdS/P3HT/Ag heterojunction.

5.3 Photoluminescence and Current Voltage Characterization of CdS/P3HT

Optical characterization was performed on CdS/P3HT samples to investigate the effects of charge transport on the photoluminescence properties of the polymers. PL studies were performed on these samples to study charge transport in these heterojunctions and also the properties of electronic states. The HOMO and LUMO levels for P3HT are at -5.0 eV and -3.0 eV as seen in Figure 36. Also, the E_c and E_v bands of CdS are also shown in Figure 36. The conduction band minimum and the valence band maximum values for CdS are: E_c -4.3 eV and E_v -6.6 eV [87]. Therefore, after band alignment of the Fermi level of CdS and P3HT gives the following band diagram with $\Delta E_c = -E_{LUMO,P3HT} - E_{c,CdS}$ = - 0.8 eV and $\Delta E_v = E_{HOMO,P3HT} - E_{v,CdS}$ = -1.3 eV where ΔE_c and ΔE_v are the discontinuities in the conduction and valence band edges. Energy band for the CdS/P3HT heterojunction is given in Figure 37.

PL was performed only on the P3HT dissolved in chloroform solution alone to find the peak intensity of the conductive polymer P3HT. Figure 38 (a) shows the PL spectra of the P3HT solution on an ITO coated glass substrate.

The peak for P3HT was observed at 650 nm (1.9 eV) around its band gap of 1.9 eV. The PL peaks for the CdS/P3HT sample was observed for the both CdS at 510 nm and P3HT peak was observed at 650 nm with a lower intensity due to the charge transport between CdS and P3HT heterojunction. Figure 38 (b) shows the PL peaks for both CdS NWs along with the P3HT peak. The peak for CdS and P3HT was observed at 510 nm and 650 nm respectively.

The top contact was the silver (Ag) formed using silver paint to study the current voltage properties of ITO/CdS/P3HT/Ag heterojunction. However, the top contact Ag and back contact ITO are at - 4.7 eV and - 4.8 eV respectively which is not shown in the band diagram in Figure 37.

Current voltage (I-V) characteristics were measured on the CdS/P3HT sample using HP4156B semiconductor parameter analyzer and a probe station at room temperature. The I-V measurement for ITO/CdS NWs/P3HT/Ag is shown in Figure 39 (a) and the schematic for the circuits is shown in Figure 39 (b).

Charge transport in conductive polymers propagates through the extended π-bonded system through the transfer of either electrons or holes, but there can be a reduction in mobility of charge carriers due to localization of charge carriers at the semiconductor-polymer contact arising from structural defect related traps, variations in interchain distances in the coated P3HT polymer and scattering sites. But the sharp PL peak at 650 nm near its band gap denotes the structure of P3HT layer was of good quality.

The I-V characteristics of the n-CdS: P3HT junction are those of a Schottky rectifying barrier as mostly conductive polymers can exist in either metallic or semiconductor-like state, therefore rectifying junctions are formed when a junction is formed between the polymer and a metal or polymer and semiconductor [88]. In forward bias, the current increases exponentially at potential of 1 V. In applied reverse bias, very little current of around -0.1 mA was observed as seen in zoomed Figure 40 (b).

For Schottky barrier like n-CdS/P3HT, the current density J with respect to applied bias V_a is given by (5.1) equation

$$J = J_0 e^{qV_{a/\eta kT}} \quad (5.1)$$

where J_0, is the saturation current, η is the quality factor, q is the electronic charge, $\boldsymbol{k}$ is the Boltzmann constant, and $\boldsymbol{T}$ is the absolute temperature. The barrier height ϕ_b can be derived from the equation J, by using the Richardson equation [88]:

$$J_0 = R^* \exp\left(\frac{\phi_b}{kT}\right) \quad (5.2)$$

where $R^* = R\,(m^*/m_e)$, $m^* = 0.21m_e$ for n-CdS using Table I values and Richardson constant R = 120 A cm^2 K^2 is the Richardson constant for free electrons [88].

By analyzing, the experimental I-V curve we get saturation current J_s equal to 3.45×10^{-17} A/cm^2 and diode quality factor η was found to be 1.8, and a barrier height ϕ_b of 0.95 V. The barrier height and the quality factor of the n-CdS: P3HT junction were calculated theoretically and fitted with the experimental I-V curve of CdS/P3HT in MATLAB as shown in Figure 40 (a). Its seen that there is a deviation in the experimental curve than the simulated curve which can be because of the reduction of mobility due to interchain conduction and some defects present in the heterojunction.

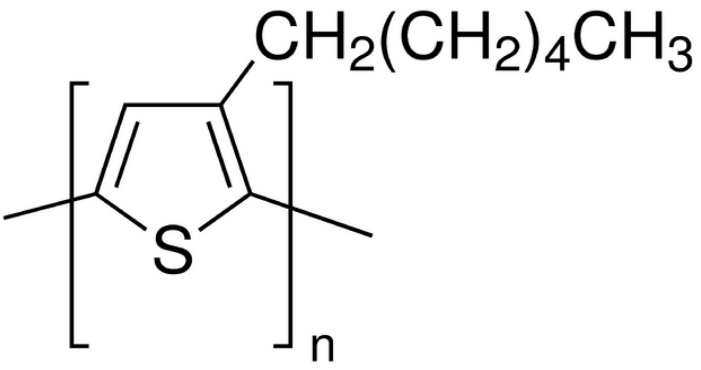

Figure 35: Monomer unit of conductive polymer P3HT [89].

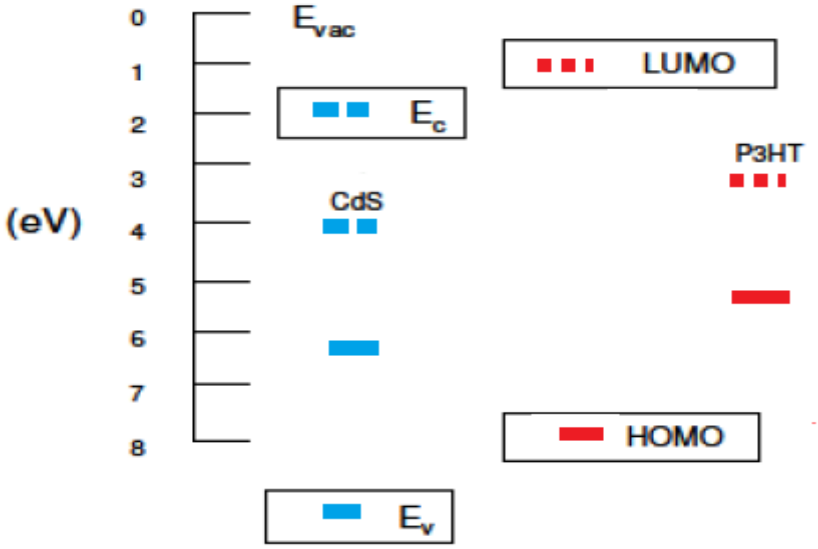

Figure 36: HOMO and LUMO level of P3HT along with E_c and E_v level of CdS.

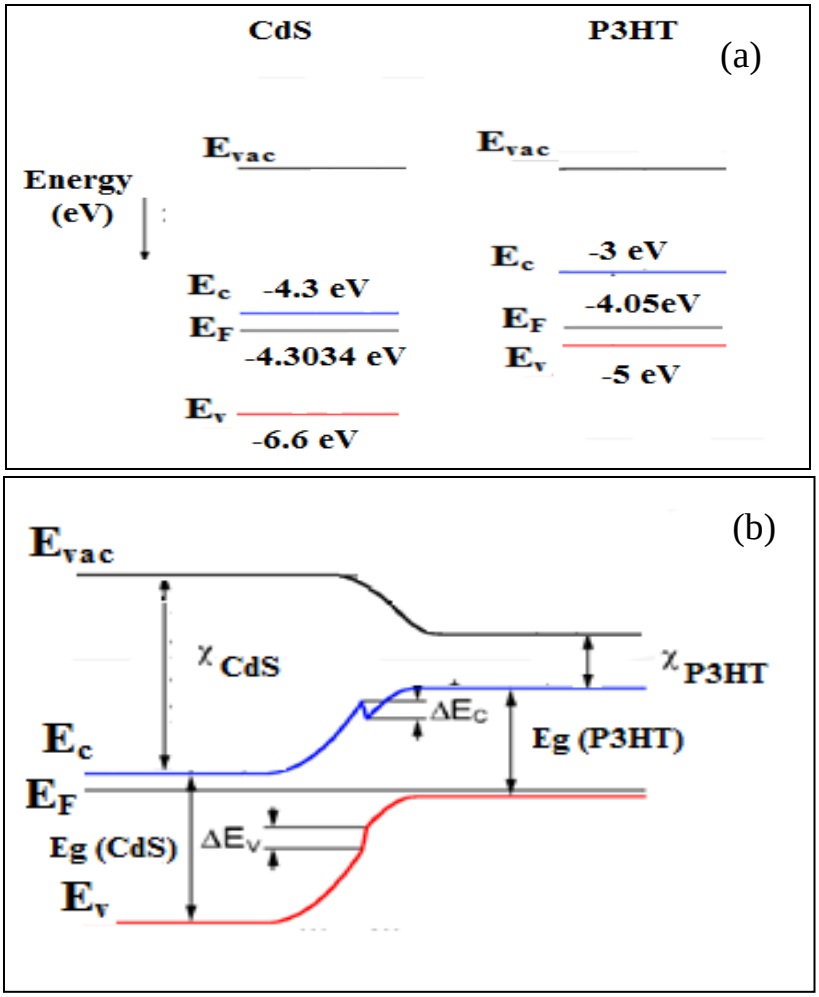

Figure 37: (a) Before contact, energy levels expressed with respect to E_{vac}. (b) Band diagram of CdS/P3HT heterojunction

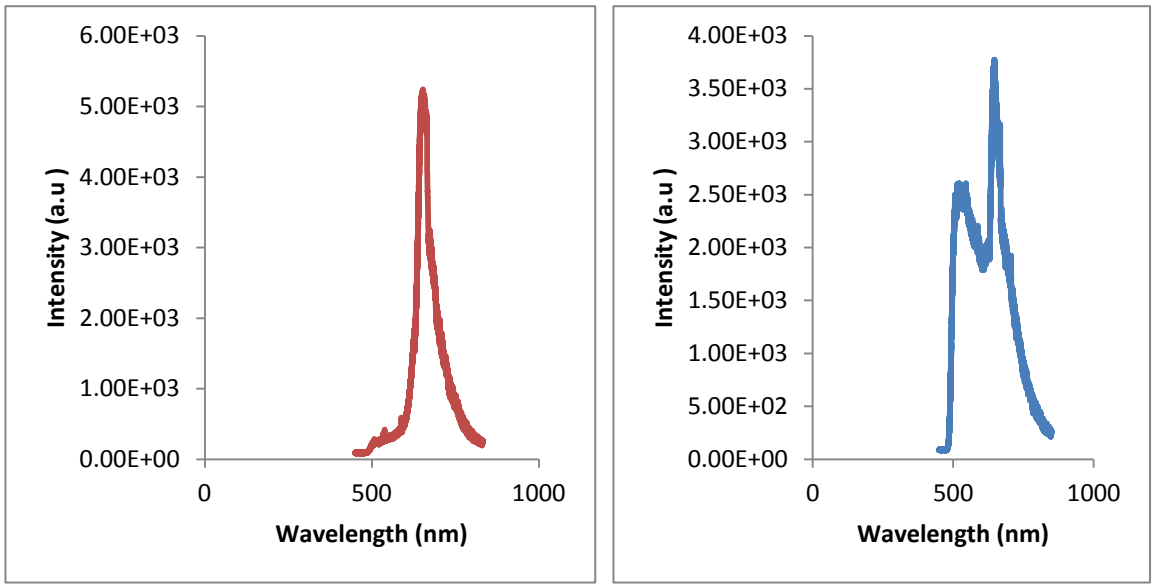

(a) (b)

Figure 38: (a) PL spectrum of P3HT solution with peak at 650 nm (b) PL spectra of CdS/P3HT heterojunction with CdS peak at 510 nm and P3HT peak at 650 nm.

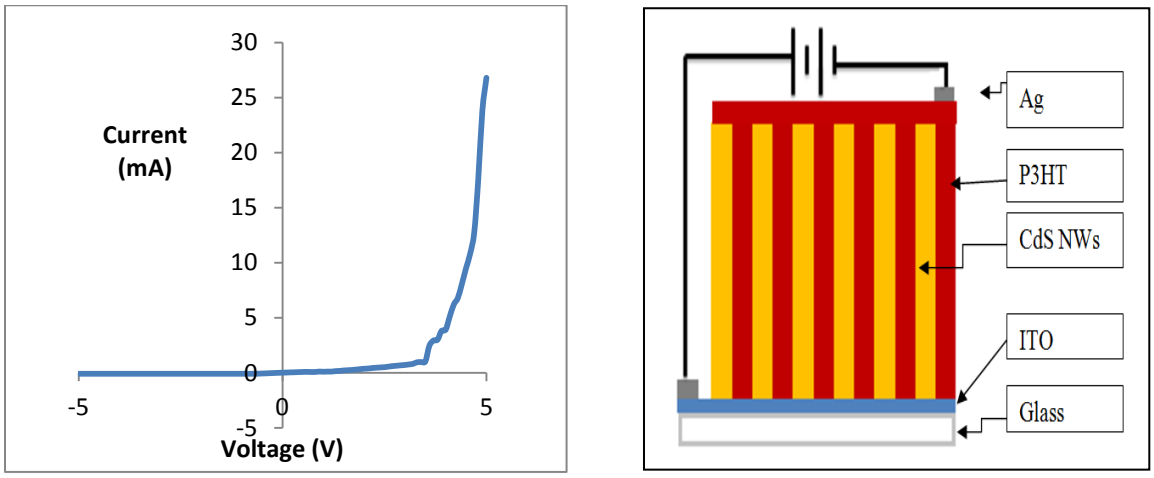

(a) (b)

Figure 39: (a) I-V curve of CdS/P3HT. (b) Schematic of CdS/P3HT measurement circuit.

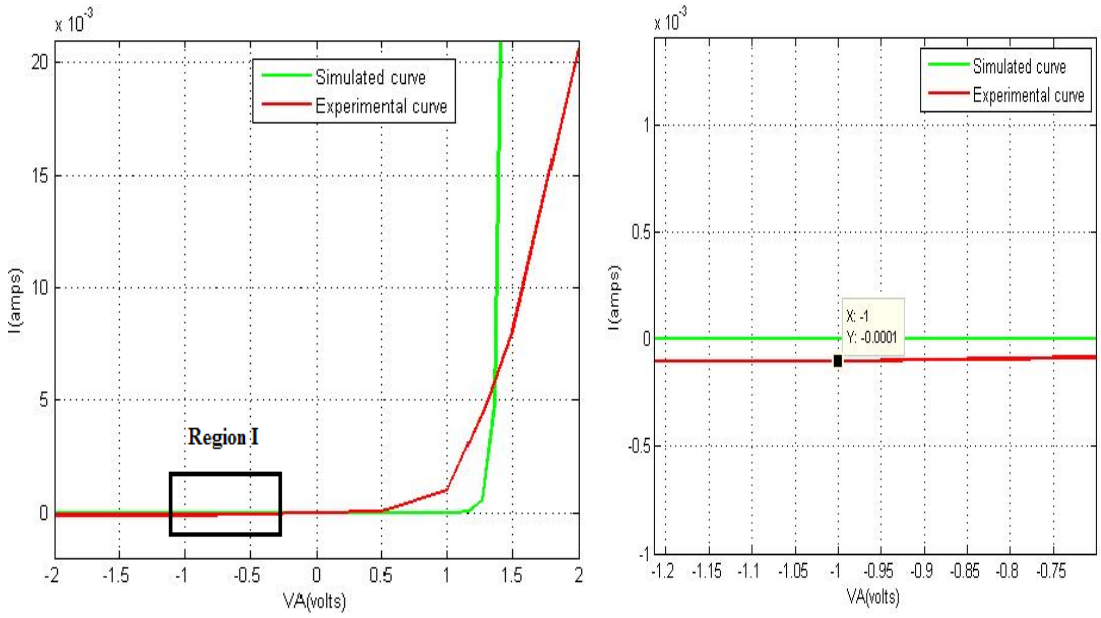

(a) (b)

Figure 40: (a) Comparison of simulated and experimental I-V curve, (b) Region I zoomed to show the experimental current value.

Chapter 6 Uses of CdSe/ZnS Quantum Dots

In this chapter, a novel method to detect voids on the copper surface is discussed. This method of detection can be useful in detecting voids in copper interconnects and contacts for system reliability. Quantum dots (QD) properties were employed to detect the nanocavities on the copper surface since it's easy to detect the presence of a QD with its emission and excitation properties at a particular wavelength. The nanopores of copper undergo crevice corrosion and behave like an anode, which binds with a negatively charged carboxyl functionalized QDs and repels the positively charged amine QDs. Section 6.1 gives the introduction to the detection method. Section 6.2 discusses the experimental details of binding QDs to the copper surface. Positively charged amine functionalized CdSe/ZnS QDs and negatively charged carboxyl functionalized QDs were used for binding to determine the cathodic or anodic nature of the copper nanopores undergoing crevice corrosion. Section 6.3 discusses the results after the drop cast and washing of amine and carboxyl QDs on copper surfaces. Section 6.4 discusses the partial masking of copper surfaces and its results.

6.1 Introduction

Semiconducting quantum dots (QDs) have generated lot of interest due to their properties in the field of research [90, 91]. The electronic structure in quantum dots is dependent on quantum confinement effects in all three spatial dimensions. As a result, the optical properties are quite different than the bulk material. In addition, quantum dots are of technological interest as the active material in optoelectronic devices such as light emitting diodes (LED), photo detectors, transistors, solar cells, and diode lasers [92, 93].

They have higher absorption coefficients compared to the bulk material [94]. They have electronic characteristics, which are closely related and tunable by their size and shape.

It is desirable to detect voids of nanoscale dimensions on copper surfaces; indeed such a capability may be of use in detecting voids in copper interconnects and contacts for system reliability [95]. QD properties were employed to detect the nanocavities on a copper surface since it's easy to detect the presence of a QD with its emission and excitation properties at a particular wavelength. These QDs have band gap energies that depend on size and have highly tunable excitation frequencies and unique surface chemistry creating dangling bonds, or adsorbents at the surface [96]. The binding of QDs due to the dangling bonds created by the negatively charged functionalized groups of QDs with the anodic like nanopores structures of copper surface aids in finding the location of the nanopore on the copper surface.

The copper nanopores behave like surfaces exhibiting crevice corrosion where metal behaves like an anode undergoing reaction with cathode like species such as here the negatively charged carboxyl functionalized group of the QD [97]. These bound QDs were easy to examine with fluorescence microscope under 655 nm filter around its characteristic wavelength of 650 nm that will detect in the fluorescence of bound QDs on the copper nanopores.

6.2 Experimental details

Firstly, copper surface purchased from Sigma Aldrich of 0.5 mm thickness was anodized to produce nanopores to test if the QDs bind to the holes on the copper. The copper surface was anodized in 3.5 M NaOH solution to produce nanopores in the copper surface at 10 °C with anode as copper of size 1 cm by 1 cm and cathode as platinum

electrode by applying a voltage of 40 V for 5 mins, 10 mins, 15 mins and 20 mins [98]. A barrier layer of oxide is usually formed after the anodization of copper, which should be removed before binding the QDs to the nanopores. After the anodization of the copper, CdSe/ZnS core shell QDs 650 NC (purchased from eBioscience Inc.) were drop cast on to the copper surface and left for overnight for drying. Positively charged amine and negatively charged carboxyl CdSe/ZnS QDs were used to determine the anodic or cathodic nature of copper nanopores. These anodized copper surfaces with QDs were studied under fluorescence microscope to determine if the QDs were binding to the nanopores on the copper surface. Following this, these copper surfaces with QDs were washed with deionized (DI) water four times and examined after each wash under fluorescence microscope to determine if the QDs actually bind to the nanopores on the copper surface. After each wash, the QDs were observed under the fluorescence microscope proving that these QDs bind to the nanopores on the copper surface. The barrier layer formed after the anodization of copper was removed by immersing the sample in 0.1 M sulfuric acid for 1 hour at room temperature. However, after the removal of the barrier layer these QDs were drop cast and examined under fluorescence microscope to check if the QDs bind to the nanopores on the copper surface. These QDs can be only removed from the copper surface only if we heat the surface at 100 °C for 30 minutes. The results are discussed in the next section.

6.3 Results and Discussion

6.3.1 Carboxyl functionalized QDs on copper surface

The copper surfaces were anodized in 3.5 M NaOH solution at 40 V for 5, 10, 15 and 20 minutes and were examined under JEOL 6320 Field Emission Scanning Electron

microscope (FESEM) after the removal of barrier layer. The SEM micrographs are shown in the Figure 41.

The CdSe/ZnS 650 NC quantum dots were drop cast on the copper surface and were looked under fluorescence microscope to see if these QDs bind to the nanopores of copper surface after washing it 4 times in DI water to determine the binding of the nanopores of the QDs. The images of the copper surface with the drop cast QDs before the wash are shown in Figure 42.

Since the left and right images above are correlated by one to one basis, nanopores location can be correlated to the QDs location in its right image and it can be said that the QDs bind to the nanopores of the copper surface. The sample with QDs was washed with DI water and was examined under fluorescence microscope and images are shown in Figure 43.

Looking from the images above, we can say that the QDs bind to the nanopores of the copper surface. The AFM images of the copper surface are shown in Figure 44 to see the binding of the QDs to the surface.

These anodized copper surfaces were heated to 100 °C for 30 minutes and these surfaces were allowed to cool down. The surfaces were then wiped off with a Kimwipe. The bound QDs were removed from the copper surface and were found on the Kimwipe when examined under fluorescence microscope. The copper surface and the Kimwipe were both examined under fluorescence microscope. The QDs were seen only on the Kimwipe and not on the copper surface showing that the QDs were removed from the copper surface. The images of the Kimwipe with QDs are shown in Figure 45.

The images of the copper surface after heating it to 100°C for 30 minutes and then wiping it off with Kimwipe are shown in Figure 46. There were no QDs seen on the copper surface, which confirms the removal of the QDs from the copper surface after heating.

6.3.2 Amine QDs on copper nanocavities

To further investigate the nature of binding of these negatively charged carboxyl functionalized CdSe/ZnS QDs with the nanopores of copper surface, positively charged amine functionalized CdSe/ZnS QDs 650 NC were purchased from Life Technologies Inc., and similarly the amino functionalized CdS/ZnS 650 QDs were dropcast on the anodized copper surfaces to determine the binding nature of copper nanopores. The copper nanopores may be understood in a manner analogous to surfaces exhibiting crevice corrosion where metal behaves like an anode undergoing reaction with cathode like species such as here the negatively charged carboxyl functionalized group of the QD [97]. Therefore, these positively charged amino functionalized QDs were not seen on the anodized copper surface under fluorescence microscope after washing this surface as shown in Figure 47 which confirms that the nanoporous copper surface behaves like an anode and does not bind with positively charged amine groups of the QD.

Figure 47 (c) and (d) shows the negatively charged carboxyl functionalized QDs binding to the copper nanopores for comparison proving that the copper nanopores binds to negatively charged functionalized QDs and not the positively charged functionalized QDs.

6.4 Partial anodization of copper surface with a mask

The copper was anodized in NaOH solution only in half of the region by masking half of the copper surface with an insulation tape and scotch tape to grow nanopores only in half of the region of the copper surface. These negatively charged carboxyl group QDs were seen to bind only in anodized region of the copper surface confirming that only the nanoporous surface of copper behaves like an anode and binds with the negatively charged carboxyl groups of QDs. The copper surface was masked for half of the region of the sample and then anodized to form nanopores only in half of the region as shown in Figure 48.

The sample was anodized for different times to grow different sizes of nanopores to determine if binding of QDs to nanopores is a function of size of pores. The SEM images for four different anodization times of 5, 10, 15 and 20 minutes were shown in Figure 41 and these samples were called as sample A, B, C and D with respect to increasing time of anodization.

The negatively charged carboxyl functionalized CdSe/ZnS 650 NC were drop cast all over the partially anodized sample and rinsed with DI water four times. After rinsing with DI water the four samples were examined under fluorescence microscope and the images are all shown in Figures 49, 50, 51 and 52.

In all the samples the QDs were observed only on the nanoporous side under red fluorescence with using 655 nm filter to observe the fluorescence of the carboxylic group. It was observed that negatively charged carboxyl functionalized QDs bound to the nanopores since the QDs on the non-porous side were washed away by DI water rinse.

This is a novel strategy of detecting nanocavities on metallic surfaces like copper by using QDs since QDs are of the size of only 5-10 nm which can have chances in binding with the voids of the metallic surfaces if present. This method of the detecting nanocavities on metallic surfaces can be employed in many industrial applications.

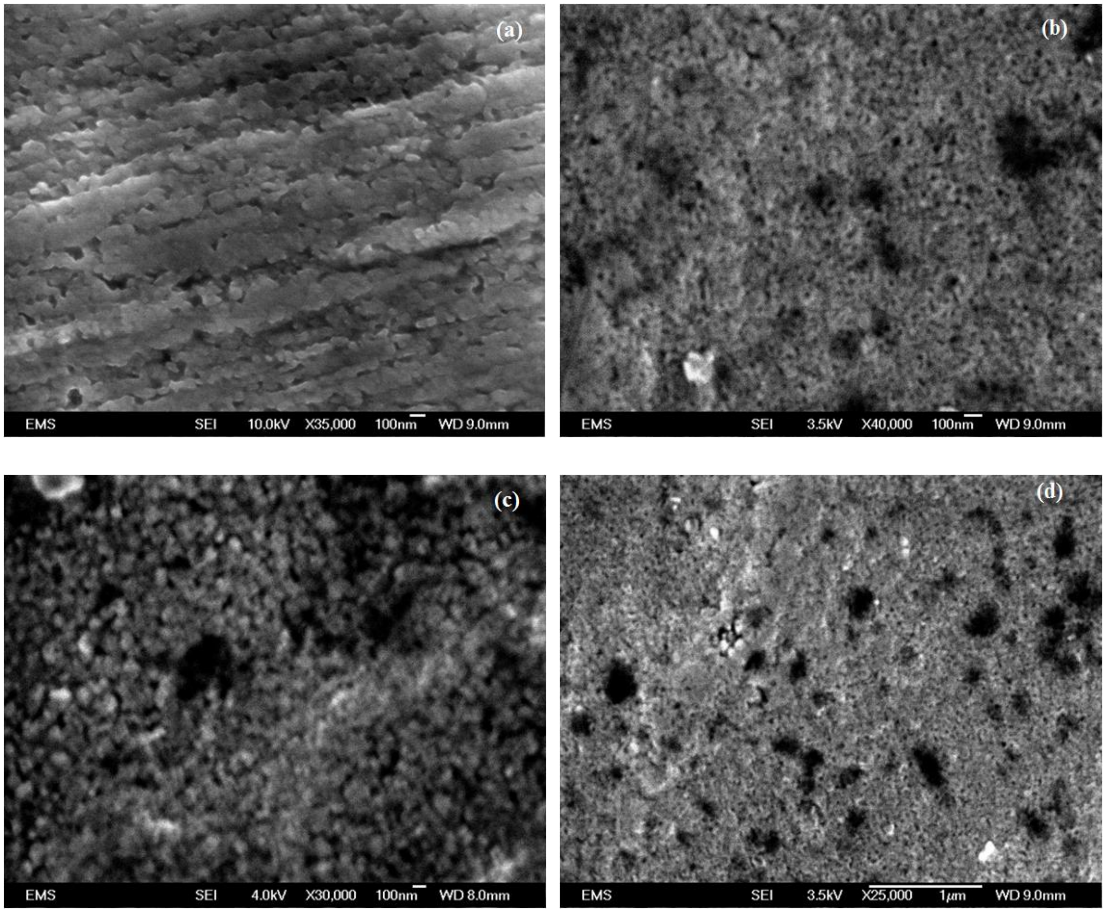

Figure 41: (a) 5 minute anodization, sample A (b) 10 minute anodization, sample B (c) 15 minute anodization, sample C (d) 20 minute anodization time, sample D.

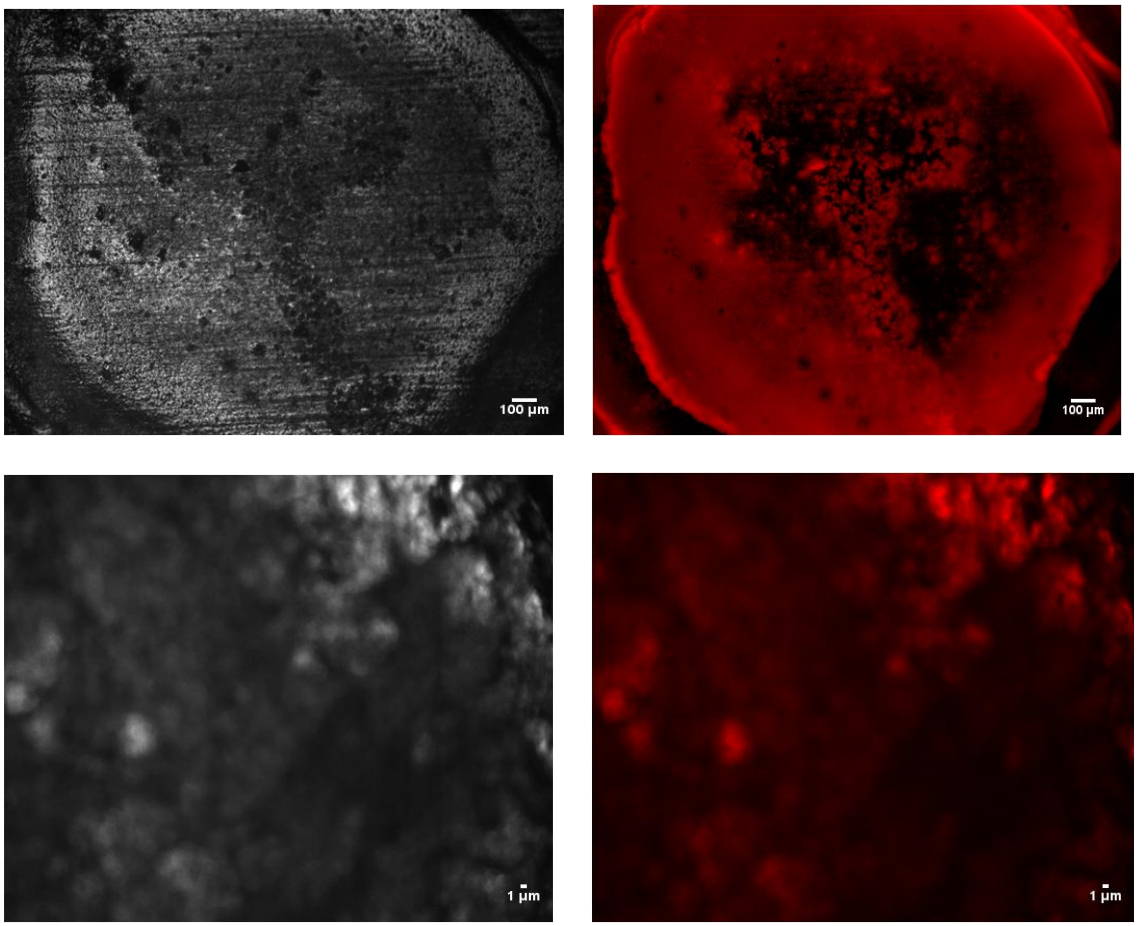

Figure 42: (Clockwise from left): (a) White light image of 2 mm drop of 650 NC QDs under 4X Magnification. (b) Red fluorescence image of the same area under 4X magnification with 655 nm filter. (c) 50 X magnification of the same area in red fluorescence using 655 nm filter. (d) 50 X magnification of the same area in white light.

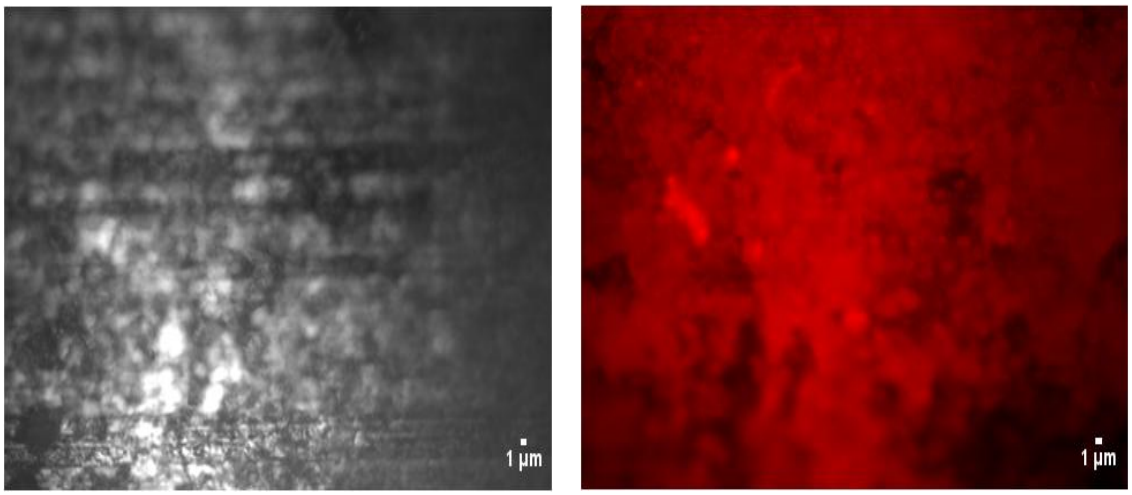

(a) (b)

Figure 43: 50 X magnification image after the fourth wash with DI water (a) under white light (b) red fluorescence under 655 nm filter.

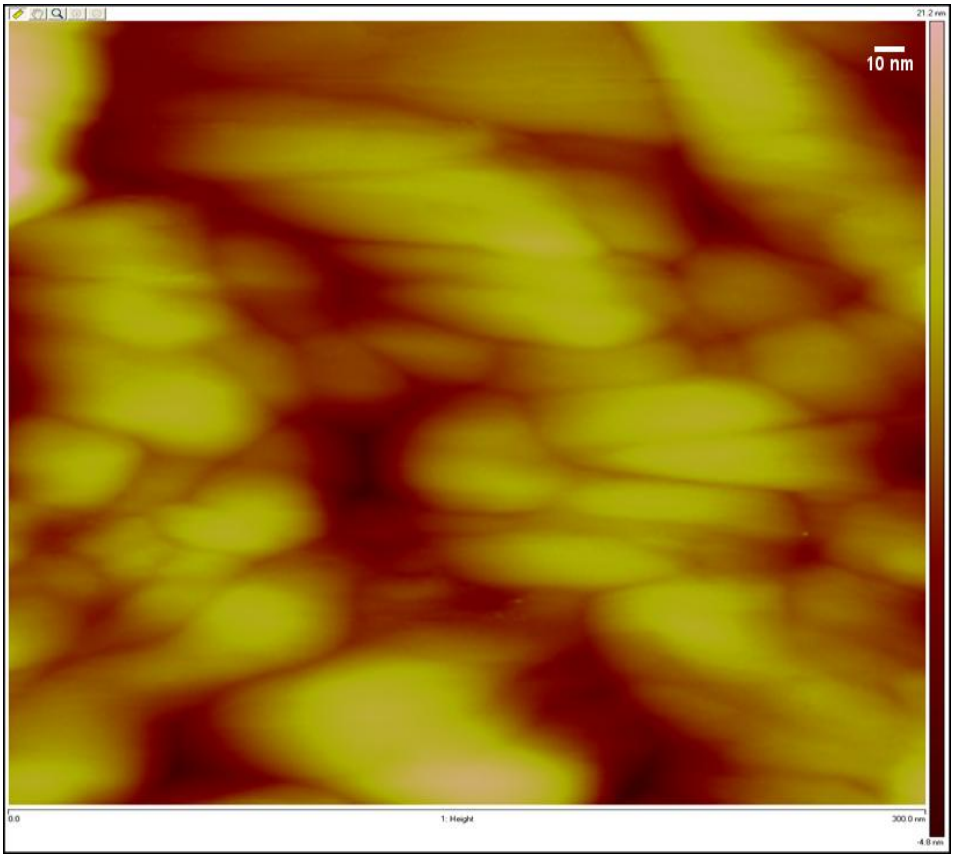

Figure 44: AFM micrograph of the copper surface with the QDs on it.

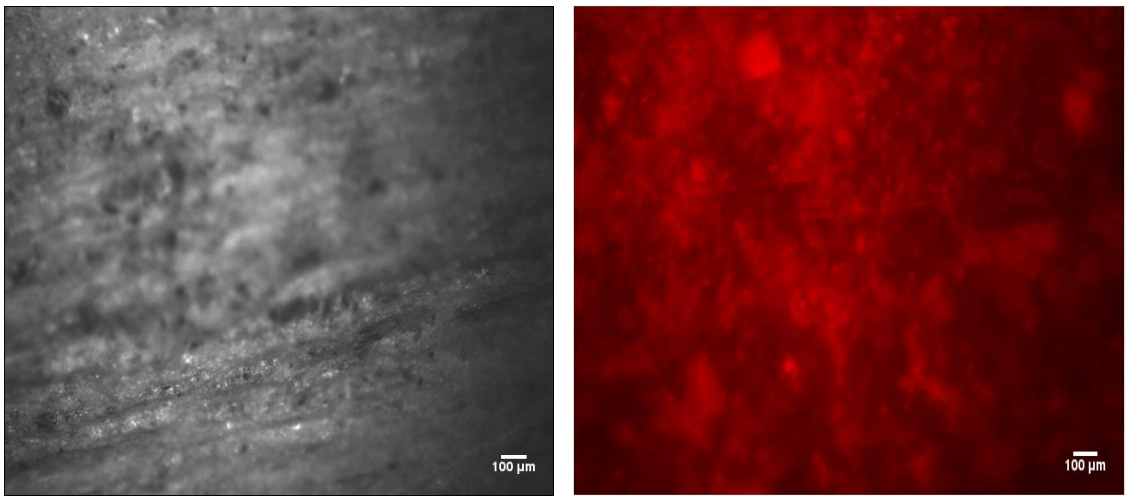

(a) (b)

Figure 45: 4X magnification image of the Kimwipe (a) under white light (b) red fluorescence with 655 nm filter.

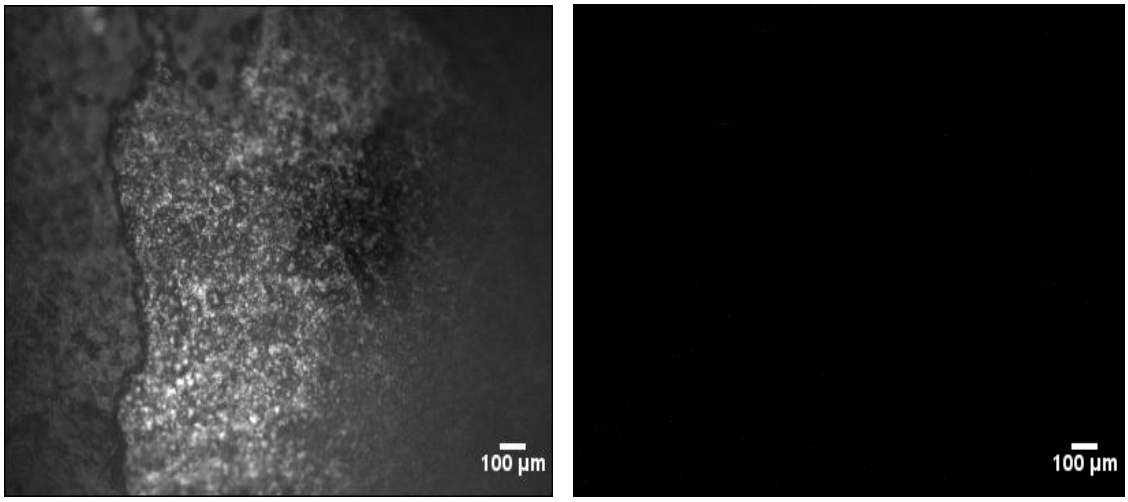

(a) (b)

Figure 46: 50 X magnification image after heating the copper surface (a) under white light (b) red fluorescence under 655 nm filter.

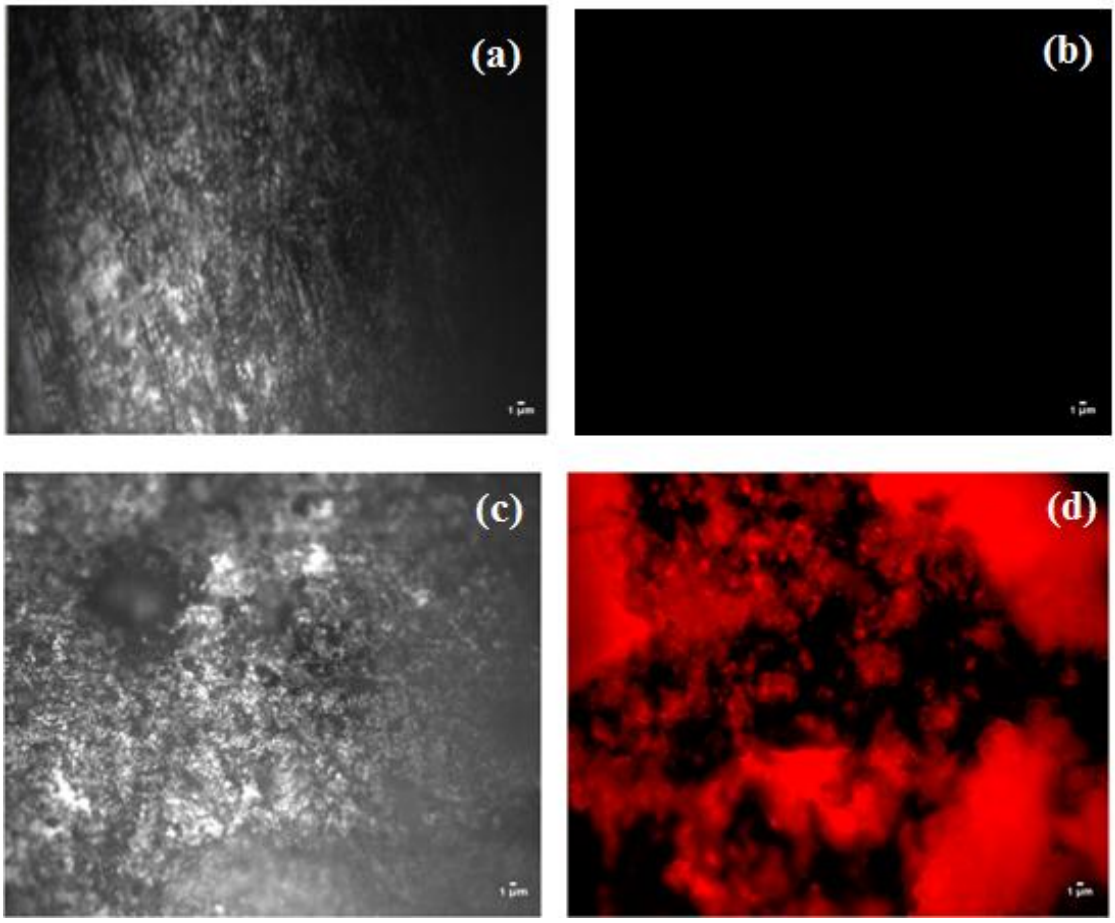

Figure 47: a) White light image of anodized copper surface with drop cast amine functionalized CdSe/ZnS QDs after washing four times. b) Red fluorescence image of the same area under 50X magnification with 655 nm filter. Positively charged amino QDs were not seen under fluorescence microscope, therefore these QDs did not bind to the anodic like nanopores of copper surface (c) 50 X magnification image of carboxyl functionalized binding after the fourth wash with DI water under white light (d) red fluorescence under 655 nm filter.

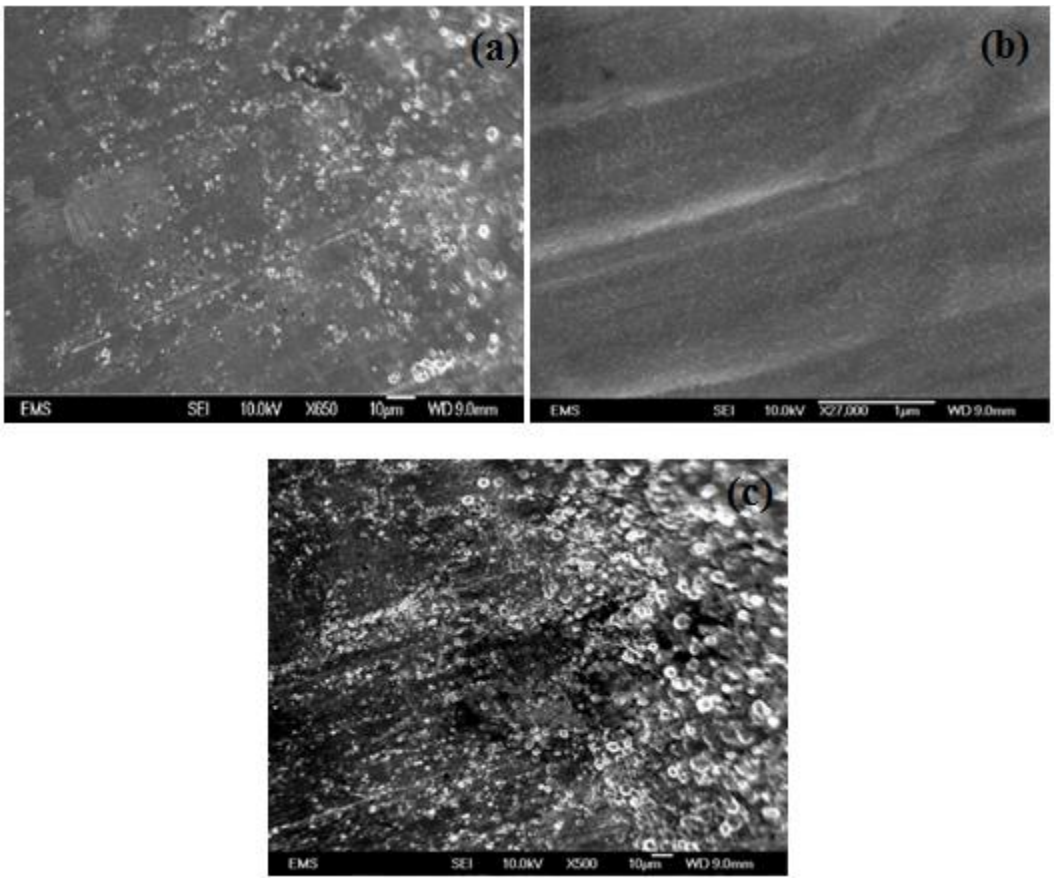

Figure 48: (a) SEM image showing both the regions where the right side region of the sample which was anodized and left hand side region of the sample was masked with scotch tape and was not anodized. (b) Higher magnification of unanodized left side region image where we could see only the copper surface without pores since it was not anodized. (c) SEM image showing the right region of anodized area of copper.

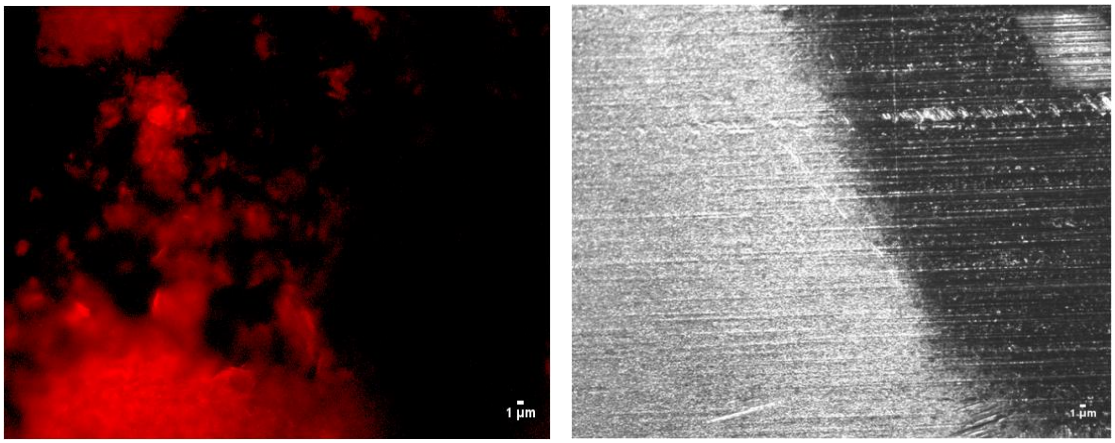

Figure 49: Left hand side region of sample was anodized for 5 minutes and right hand side region of the sample was masked with scotch tape resulting in 20 nm pores as seen in sample A. Quantum dots were observed only in nanoporous side

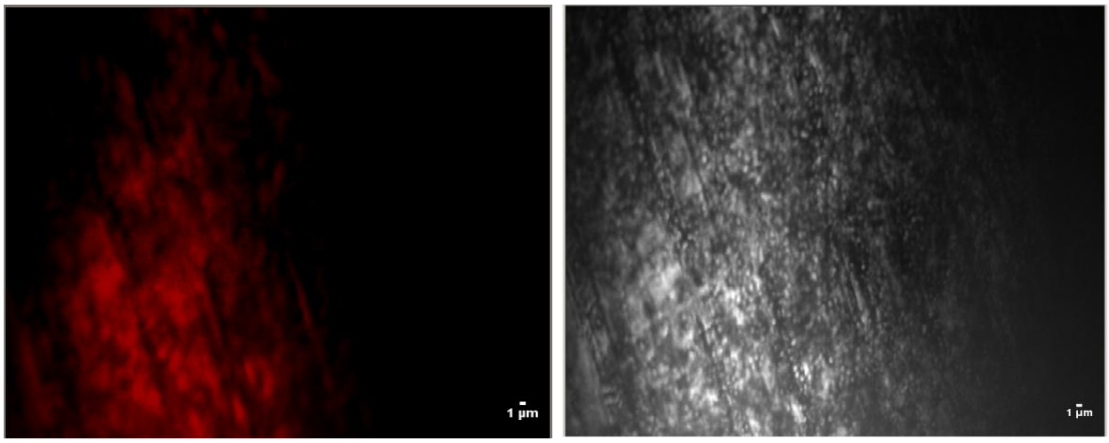

Figure 50: Left hand side region of the sample was anodized for 10 minutes and right hand side region of the sample was masked with scotch tape resulting in 40 nm pores as seen in sample B. Quantum dots were observed only in nanoporous side.

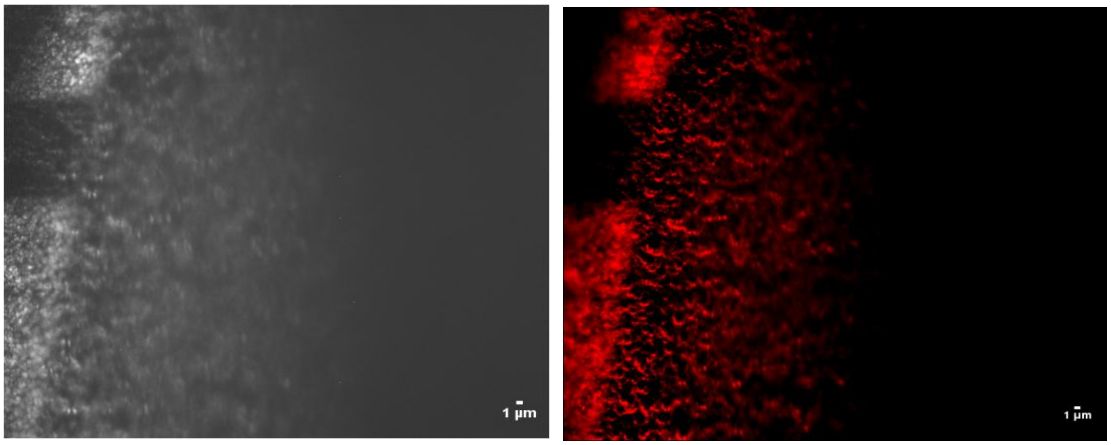

Figure 51: Left hand side is anodized for 15 minutes and right hand side of the sample was masked with scotch tape resulting in 100 nm pores as seen in sample C. Quantum dots were observed only in nanoporous side.

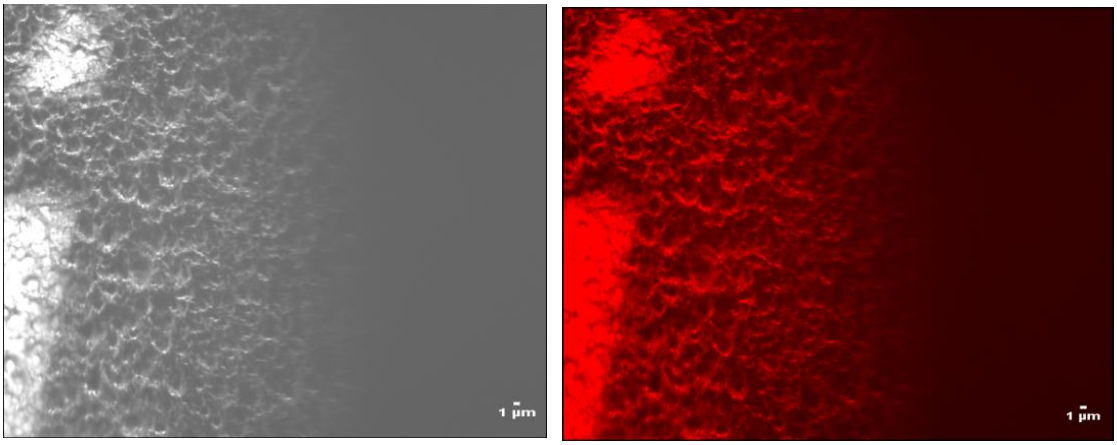

Figure 52: Left hand side region of the sample was anodized for 20 minutes and right hand side region of the sample was masked with scotch tape resulting in 400 nm pores as seen in sample D. Quantum dots were observed only in nanoporous side.

Chapter 7 Conclusion and Future Work

7.1 Conclusion

This thesis can be summarized into three main parts. The first part focuses on the growth of CdS nanowires in nanoporous templates. The surface morphologies of these CdS nanowires were studied and characterization was performed using photoluminescence and Raman spectroscopy including the calculation of surface depletion region width of the grown nanowires. Polarization anisotropy properties were investigated for its possible use in nanoscale based polarization sensitive devices. Also, the electron phonon interaction in these CdS nanowires was studied with respect to polarization. The second part involves the study of the heterojunction of CdS nanowires and conductive polymer, Poly (3-hexylthiophene-2, 5-diyl) (P3HT). These heterojunctions were optically and electrically characterized for its use in photovoltaic cells. The third part emphasized on the novel detection of nanopores on copper surfaces using optical properties of functionalized CdSe/ZnS QDs, such as fluorescence and its unique surface chemistry.

There are some serious bottlenecks or fabrication issues in growing nanowires in nanoporous AAO thin template of 200 nm because of its susceptibility to crack and poor connectivity to the substrate and these bottlenecks or fabrication issues have been discussed in detail in Chapter 2. It's a highly advantageous procedure to grow nanowires in AAO template because of its ability to withstand high temperature, high reproducibility and easy to fabricate large arrays of nanowires of high aspect ratios. We have employed a simple DC electrodeposition procedure to self-assemble CdS nanowires in a thin AAO template and briefly describing the fabrication issues at each fabrication

step. Firstly, the AAO templates were grown here at UIC by us in 200 nm deposited aluminum on ITO coated glass substrate. Secondly, the AAO templates were also grown in 500 μm Al sheet at Brown University by us with an appended step of electropolishing which resulted in better template growth with a stable structure and had less susceptibility to crack. Also, high quality CdS nanowires of thin diameter of about 40 -50 nm were grown successfully by DC electrodeposition in both the templates grown at UIC and Brown University. Furthermore, VLS technique growth was used to fabricate CdS nanowires since the nanowires were hard to grow sometimes because of the incomplete removal of barrier layer. Raman spectral and PL studies were performed on these nanowires to study the electronic structures of the nanowires, which were consistent with the previously published CdS nanowires peak values demonstrating good quality of CdS nanowires. These CdS nanowire arrays were used to form heterojunctions with conductive polymer P3HT for its possible use in solar cells. These ITO/CdS NWs/P3HT/Ag heterojuctions were optically and electrically characterized.

The PL measurements on these grown CdS nanowires were discussed in Chapter 3. The PL peaks were observed near to the band gap 510 nm of CdS nanowires. Furthermore, to analyze the underlying recombination processes in PL, intensity dependent PL measurements were performed with different intensity filters before and after annealing to investigate the defect states if present in the grown CdS nanowires. It was observed that the linearity improved after annealing showing that the underlying recombination were mostly band to band showing that the crystallinity improved after annealing. The surface depletion region in CdS nanowires were theoretically analyzed and computed. The diameter of the cylindrical nanowires was computed using

Schrodinger equation in cylindrical coordinates, which was in accordance with the actual diameter of the CdS nanowires.

The polarization anisotropy of these nanowires was also studied. A polarization ratio of 0.85 shows good polarization anisotropy in these nanowires. Only a polarization ratio of 0.67 has been observed till now with CdS nanowires [87].

Chapter 4 discusses about the Raman spectroscopy studies of CdS nanowires grown on ITO coated glass substrate in an anodized alumina template and in an anodized alumina sheet. The Raman spectroscopy studies were performed on VLS grown CdS nanowires for comparison with the DC electrodeposited growth. Strong 1 LO, 2 LO and 3 LO peaks were observed for these grown CdS nanowires 302 cm^{-1}, 603 cm^{-1} and 906 cm^{-1} corresponding to the longitudinal optical phonon (LO) modes 1 LO, 2 LO and 3 LO, respectively, analogous to the peaks of pure CdS crystalline structure. Electron phonon coupling constants were computed theoretically to study the electron phonon interaction in these CdS nanowires. The optical properties of CdS nanowires are strongly influenced by strain, crystallinity, size confinement, and electron phonon phonon interaction. This influence was seen in these grown CdS nanowires and we observed a slight shift in the LO phonon frequencies of CdS nanowires from its bulk values. Also, all the phonon modes corresponding to wurtzite crystal were observed for CdS nanowires to study the polarization effect for Raman spectral studies.

Also, these CdS nanowires can be used for photovoltaic applications by fabricating a polymer based CdS heterojunction, which is discussed in detail Chapter 5. Optical and electrical characterizations for CdS NWs/P3HT polymers were performed for its use in photovoltaic applications and study its electronic transport properties. These I-V

characteristics of CdS/P3HT were theoretically simulated in MATLAB to compute the characteristics in Chapter 5.

Quantum dots were used to detect nanocavities on copper surface. The CdSe/ZnS 650 NC quantum dots bound to the copper surface since the QDs remained on to the copper surfaces even after washing these surfaces four times with DI water. Also, these QDs can be removed from the copper surface by heating the surface for 30 minutes to 100 °C and then wiping it off after when it's cooled down. It was observed negatively charged functionalized carboxyl QDs were binding to the nanopores of copper surfaces but positively charged amino QDs were not binding to copper nanopores. Therefore, it was inferred that the copper nanopores undergo crevice corrosion and behave more like an anode. The detection of nanocavities on copper surfaces by using the binding properties of QDs will be useful in many industrial applications.

7.2 Future work

Also, other metallic or direct band gap semiconductors can be self-assembled in anodized alumina templates for its use in optoelectronic applications. The only drawback with the anodized alumina template is the incomplete removal of the barrier layer of oxide which prevents the growth of nanowires. But, these templates have been widely used to grow nanowires since it's easy to grow with an added advantage of flexibility to change the size of nanopores and it's highly reproducible. Other best feature of these anodized templates is that it can withstand high temperatures of 1000 °C. Hence, these templates can be used to grow long nanowires using VLS mechanism too. Not only this, these nanoporous templates can also be used to grow nanowires for its use in other applications such as energy harvesting devices and energy storage devices. Other

methods of nanoporous template growth can also be implemented such as using nanoimprint lithography/dip pen lithography/block copolymer lithography to fabricate the nanowires of less than 30 nm in diameter. However, it's possible to grow nanowires of less than 30 nm in AAO templates but it requires very low temperature of the order of -5 to -20 °C. Therefore, fabrication of solar cells using the anodized alumina template growth and these above mentioned ways of lithography for the growth of the template could be a possible future work.

The optimization of the properties of these CdS NWs/P3HT heterojunctions for its possible use in solar cells is still underway. The performance characterization of these CdS NWs/P3HT as solar cells with or without light is still under investigation. Also, more of conductive polymers with CdS nanowires can be investigated other than P3HT for its use in solar cells. The theoretical model for the I-V characteristics of CdS NWs/P3HT needs to be analyzed further for its comparison with experimental curve. Also, other factors such as mobililty reduction due to interchain conduction, molecular dynamics, scattering centers and interfacial defects needs to be studied and optimized further.

CITED LITERATURE

1. Heath, J.R., Kuekes, P.J., Snider, G.S., and Williams, R.S.: A defect-tolerant computer architecture: Opportunities for nanotechnology, *Science*, 280:1716-1721, 1998.

2. Hu, J.T., Odom, T.W., and Lieber, C.M.: Chemistry and physics in one dimension: Synthesis and properties of nanowires and nanotubes. *Accounts Chem Res.*, 32: 435-445, 1999.

3. Morales, A.M., and Lieber, C.M.: A laser ablation method for the synthesis of crystalline semiconductor nanowires. *Science*, 279: 208-211,1998.

4. Gu, Y., Kwak, E.S., Lensch, J.L., Allen, J.E., Odom, T.W., and Lauhon, L.J.: Near-field scanning photocurrent microscopy of a nanowire photodetector. *Appl Phys Lett.*, 2005, 87, 2005.

5. Qian, F., Gradecak, S., Li, Y., Wen, C.Y., and Lieber, C.M.: Core/multishell nanowire heterostructures as multicolor, high-efficiency light-emitting diodes. *Nano. Lett*., 5: 2287-2291, 2005.

6. Patolsky, F., Zheng, G.F., and Lieber, C.M.: Nanowire-based biosensors. *Anal. Chem*., 78: 4260-4269, 2006.

7. Duan, X.F., Huang, Y., Agarwal, R., and Lieber, C.M.: Single-nanowire electrically driven lasers. *Nature*, 421: 241-245, 2003.

8. Agarwal, R., Barrelet, C.J., and Lieber, C.M.: Lasing in single cadmium sulfide nanowire optical cavities. *Nano.Lett.*, 5: 917-920, 2005.

9. Xiang, J., Lu, W., Hu, Y., Wu, Y., Yan, H., and Lieber, C.M.: Single-nanowire electrically driven lasers. *Nature*, 421: 241-245, 2003.

10. Samuelson, L., Bjork, M.T., Deppert, K., Larsson, M., Ohlsson, B.J., Panev, N., Persson, A.I., Skold, N., Thelander, C., and Wallenberg, L.R.: Semiconductor nanowires for novel one-dimensional devices. *Physica E*, 21: 560-567, 2004.

11. Kind, H., Yan, H.Q., Messer, B., Law, M., and Yang, P.D.: Nanowire ultraviolet photodetectors and optical switches. *Adv. Mater*., 14: 158, 2002.

12. Fan, Z.Y., Chang, P.C., Lu, J.G., Walter, E.C., Penner, R.M., Lin, C.H., and Lee, H.P.: Photoluminescence and polarized photodetection of single ZnO nanowires. *Appl. Phys. Lett.*, 85: 6128-6130, 2004.

CITED LITERATURE (continued)

13. Hoang, T.B., Titova, L.V., Yarrison-Rice, J.M., Jackson, H.E., Govorov, A.O., Kim, Y., Joyce, H.J., Tan, H.H., Jagadish, C., and Smith, L.M.: Resonant excitation and imaging of nonequilibrium exciton spins in single core-shell GaAs-AlGaAs nanowires. *Nano. Lett.*, 7: 588-595, 2007.

14. Shan, C.X., Liu, Z., and Hark, S.K.: Photoluminescence polarization in individual CdSe nanowires. *Phys. Rev. B*, 74: 2006.

15. Skold, N., Karlsson, L.S., Larsson, M.W., Pistol, M.E., Seifert, W., Tragardh, J., and Samuelson, L.: Growth and optical properties of strained GaAs-GaxIn1-xP core-shell nanowires. *Nano. Lett*., 5: 1943-1947, 2005.

16. Gudiksen, M.S., Wang, J.F., and Lieber, C.M.: Size-dependent photoluminescence from single indium phosphide nanowires. *J. Phys. Chem. B*, 106: 4036-4039, 2002.

17. Borgstrom, M.T., Zwiller, V., Muller, E., and Imamoglu, A.: Optically bright quantum dots in single nanowires. *Nano. Lett.*, 5: 1439-1443, 2005.

18. Sarkar, J., Khan, G.G., and Basumallick, A.: Nanowires: properties, applications and synthesis via porous aluminium oxide template. *B. Mater. Sci.*, 30: 271-290, 2007.

19. Friedman, A.L., and Menon, L.: Optimal parameters for synthesis of magnetic nanowires in porous alumina templates - Electrodeposition study. *J. Electrochem. Soc*., 154: E68-E70, 2007.

20. Kong, J., Franklin, N.R., Zhou, C.W., Chapline, M.G., Peng, S., Cho, K.J., and Dai, H.J.: Nanotube molecular wires as chemical sensors. *Science*, 287: 622-625, 2000.

21. Challa, S.S., and Kumar, R. Nanomaterials for Biosciences. Wiley-VCH: Weinheim, 2007.

22. Menon, L., Bandyopadhyay, S., and Nalwa, H. Chapter: Synthesis of Nanowires using Porous Alumina. American Scientific Publishers: Stevens Ranch, California: 142- 191, 2003.

23. Abdi, A., Titova, L.V., Smith, L.M., Jackson, H.E., Yarrison-Rice, J.M., Lensch, J.L., and Lauhon, L.J.: Resonant Raman scattering from CdS nanowires. *Appl. Phys. Lett.*, 88: 2006.

CITED LITERATURE (continued)

24. Kar, S., and Chaudhuri, S.: Shape selective growth of CdS one-dimensional nanostructures by a thermal evaporation process. *J. Phys. Chem. B*, 110: 4542-4547, 2006.

25. Alivisatos, A.P.: Perspectives on the physical chemistry of semiconductor nanocrystals. *J. Phys. Chem.*, 100: 13226-13239,1996.

26. Wang, J.F., Gudiksen, M.S., Duan, X.F., Cui, Y., and Lieber, C.M.: Highly polarized photoluminescence and photodetection from single indium phosphide nanowires. *Science*, 293:1455-1457, 2001.

27. Heeger, A.J.: Nobel Lecture: Semiconducting and metallic polymers: The fourth generation of polymeric materials. *Rev. Mod. Phys.*, 73: 681-700, 2001.

28. Voss, D.: Organic electronics: cheap and cheerful circuits. *Nature*, 407:442-444, 2000.

29. Padinger, F., Rittberger, R.S., and Sariciftci, N.S.: Effects of postproduction treatment on plastic solar cells. A*dv. Funct. Mater*., 13: 85-88, 2003.

30. Wojciechowski, J.R., Shriver-Lake, L.C., Yamaguchi, M.Y., Fureder, E., Pieler, R., Schamesberger, M., Winder, C., Prall, H.J., Sonnleitner, M., and Ligler, F.S.: Organic Photodiodes for Biosensor Miniaturization. *Anal. Chem*., 81: 3455-3461, 2009.

31. Webster, J.R., Burns, M.A., Burke, D.T., and Mastrangelo, C.H.: Monolithic capillary electrophoresis device with integrated fluorescence detector. *Anal. Chem.*, 73: 1622-1626, 2001.

32. Pais, A., Banerjee, A., Klotzkin, D., and Papautsky, I.: High-sensitivity, disposable lab-on-a-chip with thin-film organic electronics for fluorescence detection. *Lab. Chip*, 8: 794-800, 2008.

33. Cappel, U.B., Dowland, S.A., Reynolds, L.X., Dimitrov, S., and Haque, S.A.: Charge Generation Dynamics in CdS:P3HT Blends for Hybrid Solar Cells. *J Phys Chem Lett.*, 4: 4253-4257, 2013.

34. Rössler, ed., Landolt-Börnstein Group III: Condensed Matter, B: II-VI and I-VII Compounds; Semimagnetic Compounds (Springer-Verlag Berlin Heidelberg New York).

35. Hoang, B.T.: Investigation of Single Semiconductor Nanowire Heterostructures Using Polarized Imaging Spectroscopy. PhD Thesis, University of Cincinnati, Cincinnati, 2008.

CITED LITERATURE (continued)

36. Reiss, P., Protiere, M., and Li, L.: Core/Shell Semiconductor Nanocrystals. *Small*, 5: 154-168, 2009.

37. Peng, X.G., Schlamp, M.C., Kadavanich, A.V., and Alivisatos, A.P.: Epitaxial growth of highly luminescent CdSe/CdS core/shell nanocrystals with photostability and electronic accessibility. *J. Am. Chem. Soc.*, 1997, 119: 7019-7029, 1997.

38. Norris, D.J., Efros, A.L., and Erwin, S.C.: Doped nanocrystals. *Science*, 319: 1776-1779, 2008.

39. Wang, S., Jarrett, B.R., Kauzlarich, S.M., and Louie, A.Y.: Core/shell quantum dots with high relaxivity and photoluminescence for multimodality imaging. *J. Am. Chem. Soc*., 129: 3848-3856, 2007.

40. Van Zeghbroeck, B: Principles of Semiconductor, Chapter 4, Figure 4.6.1, 2011.

41. http://en.wikipedia.org/wiki/Wurtzite_crystal_structure

42. Kapadia, R., Fan, Z.Y., Takei, K., and Javey, A.: Nanopillar photovoltaics: Materials, processes, and devices. *Nano Energy*, 1: 132-144, 2012.

43. Poduri, S., Dutta, M., and Stroscio, M.: Characterization of CdS Nanowires Self-Assembled in a Nanoporous Alumina Template. *J Electron Mater.*, 43: 3979-3983, 2014.

44. Liu, P.A., Singh, V.P., Jarro, C.A., and Rajaputra, S.: Cadmium sulfide nanowires for the window semiconductor layer in thin film CdS-CdTe solar cells. *Nanotechnology*, 22, 2011.

45. Foong, T.R.B., Sellinger, A., and Hu, X.: Origin of the Bottlenecks in Preparing Anodized Aluminum Oxide (AAO) Templates on ITO Glass. *ACS Nano*, 2: 2250-2256, 2008.

46. Yin, A., Tzolov, M., Cardimona, D.A., and Xu, J.: Template-growth of highly ordered carbon nanotube arrays on silicon. *Ieee T. Nanotechnol.*, 5: 564-567, 2006.

47. Routkevitch, D., Bigioni, T., Moskovits, M., and Xu, J.M.: Electrochemical fabrication of CdS nanowire arrays in porous anodic aluminum oxide templates. *J. Phys. Chem.*, 100: 14037-14047, 1996.

CITED LITERATURE (continued)

48. Liu, P.A., Singh, V.P., and Rajaputra, S.: Barrier layer non-uniformity effects in anodized aluminum oxide nanopores on ITO substrates. *Nanotechnology*, 21, 2012.

49. Routkevitch, D., Haslett, T.L., Ryan, L., Bigioni, T., Douketis, C., and Moskovits, M.: Synthesis and resonance Raman spectroscopy of CdS nano-wire arrays. *Chem. Phys.*, 210: 343-352, 1996.

50. Hutchison, J.L., Routkevitch, D., Albu-Yaron, A., Moskovitz, M., and Nayak, R.R.: TEM and HREM structural studies of non-lithographically-produced CdS nanowires. *Microsco Semicond. Mater.*, 157: 389-392, 1997.

51. Xu, D.S., Xu, Y.J., Chen, D.P., Guo, G.L., Gui, L.L., and Tang, Y.Q.: Preparation and characterization of CdS nanowire arrays by dc electrodeposit in porous anodic aluminum oxide templates. *Chem. Phys. Lett.*, 325: 340-344, 2000.

52. Yang, Y., Chen, H.L., Mei, Y.F., Chen, J.B., Wu, X.L., and Bao, X.M.: Anodic alumina template on Au/Si substrate and preparation of CdS nanowires. *Solid State Commun.*, 123: 279-282, 2002.

53. Klein, J.D., Herrick, R.D., Palmer, D., Sailor, M.J., Brumlik, C.J., and Martin, C.R.: Electrochemical Fabrication of Cadmium Chalcogenide Microdiode Arrays. *Chem. Mater.*, 5: 902-904, 1993.

54. Chakarvarti, S.K., Vetter, J.: Microfabrication of metal-semiconductor heterostructures and tubules using nuclear track filters. *J. Micromech. Microeng*., 3: 1993.

55. Mondal, S.P., Das, K., Dhar, A., and Ray, S.K.: Characteristics of CdS nanowires grown in a porous alumina template using a two-cell method. *Nanotechnology*, 18: 2007.

56. Li, Y.D., Li, X.L., He, R.R., Zhu, J., and Deng, Z.X.: Artificial lamellar mesostructures to WS(2) nanotubes. *J. Am. Chem. Soc.*, 124: 1411-1416, 2002.

57. Wagner, R.S., and Ellis, W.C.: Vapor-Liquid-Solid Mechanism of Single Crystal Growth (New Method Growth Catalysis from Impurity Whisker Epitaxial + Large Crystals Si E). *Appl .Phys. Lett.*, 4: 89, 1964.

58. Givargizov, E.I.: Fundamental Aspects of Vls Growth. *J. Cryst. Growth*, 31: 20-30, 1975.

59. Schmidt, T., Lischka, K., and Zulehner, W.: Excitation-Power Dependence of the near-Band-Edge Photoluminescence of Semiconductors. *Phys. Rev. B*, 45: 8989-8994, 1992.

CITED LITERATURE (continued)

60. Robinett, R.W.: Visualizing the solutions for the circular infinite well in quantum and classical mechanics. *Am. J. Phys*., 64:440-446, 1996.

61. Kostic, R., and Stojanovic, D.: Electron and Hole States in Closed Spherical Quantum Dot with Linearly Graded Composition. *Acta Phys. Pol. A.* 115: 768-770, 2009.

62. Jackson, J.D.: Classical Electrodynamics. New York, John Wiley and Sons, 1999.

63. Simpkins, B.S., Mastro, M.A., Eddy, C.R., and Pehrsson, P.E.: Surface depletion effects in semiconducting nanowires. *J. Appl. Phys.* 103: 2008.

64. Li, D.H., Zhang, J., and Xiong, Q.H.: Surface Depletion Induced Quantum Confinement in CdS Nanobelts. *ACS Nano*, 6: 5283-5290, 2012.

65. Ruda, H.E., and Shik, A.: Scanning capacitance microscopy of nanostructures - art. no. 075315. *Phys. Rev. B,* 71: 2005.

66. Empedocles, S.A., Norris, D.J., and Bawendi, M.G.: Photoluminescence spectroscopy of single CdSe nanocrystallite quantum dots. *Phys. Rev. Lett.*, 77: 3873-3876, 1996.

67. Vouilloz, F., Oberli, D.Y., Dupertuis, M.A., Gustafsson, A., Reinhardt, F., and Kapon, E.: Effect of lateral confinement on valence-band mixing and polarization anisotropy in quantum wires. *Phys. Rev. B*, 57: 12378-12387, 1998.

68. Akiyama, H., Someya, T., and Sakaki, H.: Optical anisotropy in 5-nm-scale T-shaped quantum wires fabricated by the cleaved-edge overgrowth method', Phys Rev B, 1996, 53, (8), pp. R4229-R4232

69. Ils, P., Greus, C., Forchel, A., Kulakovskii, V.D., Gippius, N.A., and Tikhodeev, S.G.: Linear-Polarization of Photoluminescence Emission and Absorption in Quantum-Well Wire Structures - Experiment and Theory. *Phys. Rev. B*, 51: 4272-4277, 1995.

70. Fan, H.M., Fan, X.F., Ni, Z.H., Shen, Z.X., Feng, Y.P., and Zou, B.S.: Orientation-dependent Raman spectroscopy of single wurtzite CdS nanowires. *J. Phys. Chem. C*, 112: 1865-1870, 2008.

71. Loudon, R.: The Raman effect in crystals. *Adv. Phys.*, 13: 42382, 1964.

72. Anderson, A. The Raman Effect. Vol. 1 Principles, New York, Marcel Dekker Inc.,1971.

CITED LITERATURE (continued)

73. Ferraro, J.R., Nakamoto, K., and Brown, C.W. Introduction Raman Spectroscopy. 2nd Edition., Academic Press, 2003.

74. Lee, K.Y., Lim, J.R., Rho, H., Choi, Y.J., Choi, K.J., and Park, J.G.: Evolution of optical phonons in CdS nanowires, nanobelts, and nanosheets. *Appl. Phys. Lett.*, 91: 2007.

75. Venugopal, R., Lin, P.I., Liu, C.C., and Chen, Y.T.: Surface-enhanced Raman scattering and polarized photoluminescence from catalytically grown CdSe nanobelts and sheets. *J. Am. Chem. Soc.*, 127:11262-11268, 2005.

76. Zhang, J.Y., Wang, X.Y., Xiao, M., Qu, L., and Peng, X.: Lattice contraction in free-standing CdSe nanocrystals. *Appl. Phys. Lett.*, 81: 2076-2078, 2002.

77. Pan, A.L., Liu, R.B., Yang, Q., Zhu, Y.C., Yang, G.Z., Zou, B.S., and Chen, K.Q.: Stimulated emissions in aligned CdS nanowires at room temperature. *J. Phys. Chem. B*, 109: 24268-24272, 2005.

78. Fu, X.L., Li, L.H., and Tang, W.H.: Electron-optical-phonon scattering in wurtzite crystals. *Phys. Rev. B*, 56: 997-1000, 1997.

79. Scamarcio, G., Lugara, M., and Manno, D.: Size-Dependent Lattice Contraction in Cds1-Xsex Nanocrystals Embedded in Glass Observed by Raman-Scattering. *Phys. Rev. B*, 45: 13792-13795, 1992.

80. Arguello, C.A., Rousseau, D.L., and Porto, S.P.S.: First-Order Raman Effect in Wurtzite-Type Crystals. *Phys. Rev.*, 181: 1351, 1969.

81. Lee, B.C., Kim, K.W., Dutta, M., and Stroscio, M.A.: Electron-optical-phonon scattering in wurtzite crystals. *Phys. Rev. B*, 56: 997-1000, 1997.

82. Shen, W.Z.: Study of exciton-longitudinal optical phonon coupling in quantum wells for optoelectronic applications. *Appl. Phys. Lett.*, 79: 1285-1287, 2001.

83. Fan, H.M., Ni, Z.H., Feng, Y.P., Fan, X.F., Kuo, J.L., Shen, Z.X., and Zou, B.S.: Anisotropy of electron-phonon coupling in single wurtzite CdS nanowires. *Appl. Phys. Lett.*, 2007, 91: 2007.

84. Coropceanu, V., Cornil, J., da Silva, D.A., Olivier, Y., Silbey, R., and Bredas, J.L.: Charge transport in organic semiconductors. *Chem. Rev.*, 107: 926-952, 2007.

85. Heeger, A.J., Kivelson, S., Schrieffer, J.R., and Su, W.P.: Solitons in Conducting Polymers. *Rev. Mod Phys.*, 60: 781-850, 1988.

CITED LITERATURE (continued)

86. Kline, R.J., and McGehee, M.D.: Morphology and charge transport in conjugated polymer. *Polym. Rev.*, 46: 27-45, 2006.

87. Zhong, M., Yang, D., Zhang, J., Shi, J.Y., Wang, X.L., and Li, C.: Improving the performance of CdS/P3HT hybrid inverted solar cells by interfacial modification. *Sol. Energ. Mat. Sol. C*, 96: 160-165, 2012.

88. Frank, A.J., Glenis, S., and Nelson, A.J.: Conductive Polymer Semiconductor Junction - Characterization of Poly(3-Methylthiophene)-Cadmium Sulfide Based Photoelectrochemical and Photovoltaic Cells. *J. Phys. Chem.*, 93: 3818-3825, 1989.

89. http://www.sigmaaldrich.com/catalog/product/aldrich/698997?lang=en&region

90. Pientka, M., Dyakonov, V., Meissner, D., Rogach, A., Vanderzande, D., Weller, H., Lutsen, L., and Vanderzande, D.: Photoinduced charge transfer in composites of conjugated polymers and semiconductor nanocrystals. *Nanotechnology*, 15: 163-170, 2004.

91. Ginger, D.S., and Greenham, N.C.: Photoinduced electron transfer from conjugated polymers to CdSe nanocrystals. *Phys. Rev. B*, 59: 10622-10629, 1999.

92. Snee, P.T., Somers, R.C., Nair, G., Zimmer, J.P., Bawendi, M.G., and Nocera, D.G.: A ratiometric CdSe/ZnS nanocrystal pH sensor. *J. Am. Chem. Soc.*, 128: 13320-13321, 2006.

93. Scholes, G.D.: Long-range resonance energy transfer in molecular systems. *Annu. Rev. Phys. Chem.*, 54: 57-87, 2003.

94. Banyai, L., and Koch, S.W.: Semiconductor Quantum Dots. Singapore, World Scientific Publishing, 1993.

95. Zhang, Z., Suo, Z.G., and He, J.: Saturated voids in interconnect lines due to thermal strains and electromigration. *J. Appl. Phys.*, 98, 2005.

96. Murphy, C.J.: Optical sensing with quantum dots. *Anal. Chem.*, 74: 520A-526A, 2002.

97. Temenoff, S.J., and Mikos, A.G.: Biomaterials: The Intersection of Biology and Materials Science. Pearson, Prentice Hall, ISBN 0-13-009710-1, 978-0-13-009710-1, 2008.

98. Wu, X.F., Bai, H., Zhang, J.X., Chen, F.E., and Shi, G.Q.: Copper hydroxide nanoneedle and nanotube arrays fabricated by anodization of copper. *J. Phys. Chem. B*, 109: 22836-22842, 2005.

APPENDICES

APPENDIX A

Program to calculate the electron phonon coupling constant in MATLAB.

```
clc;

close all;

clear all;

w= linspace(1,1000)

colorstring = 'kbgry';

deg1=0

deg2=30*pi/180;

deg3=60*pi/180;

deg4=90*pi/180;

deg5=120*pi/180;

w_parl = 247;

w_perp = 235;

E1=(3.2*59536*((w_parl^2)-

(w.*w)).^2*sin(deg1)*sin(deg1))+((3.92*5.4569e+004)*((w_perp^2)-

(w.*w)).^2*cos(deg1)*cos(deg1));

Q1=E1.^0.5;

P1=((4*3.14*exp(2)*1.0546 * 10^-27)^0.5).*Q1 /(1.6*10^-4)

plot(w,P1,'Color',colorstring(1))

hold on
```

APPENDIX A (continued)

```
E2=(3.2*59536*((w_parl^2)-
(w.*w)).^2*sin(deg2)*sin(deg2))+((3.92*5.4569e+004)*((w_perp^2)-
(w.*w)).^2*cos(deg2)*cos(deg2));
Q2=E2.^0.5;
P2=((4*3.14*exp(2)*1.0546 * 10^-27)^0.5).*Q2 /(1.6*10^-4)
plot(w,P2,'Color',colorstring(2))
hold on
E3=(3.2*59536*((w_parl^2)-
(w.*w)).^2*sin(deg3)*sin(deg3))+((3.92*5.4569e+004)*((w_perp^2)-
(w.*w)).^2*cos(deg3)*cos(deg3));
Q3=E3.^0.5;
P3=((4*3.14*exp(2)*1.0546 * 10^-27)^0.5).*Q3 /(1.6*10^-4)
plot(w,P3,'Color',colorstring(3))
hold on
E4=(3.2*59536*((w_parl^2)-
(w.*w)).^2*sin(deg4)*sin(deg4))+((3.92*5.4569e+004)*((w_perp^2)-
(w.*w)).^2*cos(deg4)*cos(deg4));
Q4=E4.^0.5;
P4=((4*3.14*exp(2)*1.0546 * 10^-27)^0.5).*Q4 /(1.6*10^-4)
plot(w,P4,'Color',colorstring(4))
hold on
```

APPENDIX A (continued)

```
xlabel('Waveumber (1/cm)')

ylabel('Electron Phonon coupling')

legend('0 deg','30 deg','60 deg','90 deg');
```

APPENDIX B

MATLAB PROGRAM TO COMPUTE I-V CURVE OF CdS/P3HT heterojunction.

```
clc;
close all;
k=8.617e-5;
colorstring = 'gr';
q=1.6e-19;
T=300;
A=0.21*120*10^-4;
phi=0.95;
n=1.8;
Js= q*A*T^2*exp(q*phi/k*T)
VA=linspace(-5,5);
Ar = 0.25;
I=Js*Ar*(exp(VA/(n*k*T))-1)
close
plot(VA,I,'Color',colorstring(1));grid;
hold on;
grid on;
plot([-2,-1.5,-1,-0.5,0,0.5,1,1.5,2],[-0.099999e-3,-0.099997e-3,-0.099996e-3,-0.075228e-
3,0,0.064388e-3,1.902e-3,5.135e-3,20.61e-3],'Color', colorstring(2));
ymin=-1e-3; ymax=21e-3;
axis([-2,2,ymin,ymax]);
```

APPENDIX B (continued)

```
xlabel('VA(volts)'); ylabel('I(amps)');

legend('Simulated curve','Experimental curve');
```

APPENDIX C

11/18/2014 RightsLink Printable License

https://s100.copyright.com/MyAccount/web/jsp/viewprintablelicensefrommyorders.jsp?ref=35b7bb20-3370-42d0-9124-a1b6522b60df&email= 1/3

SPRINGER LICENSE TERMS AND CONDITIONS

Nov 18, 2014

This is a License Agreement between Shripriya D Poduri ("You") and Springer ("Springer") provided by Copyright Clearance Center ("CCC"). The license consists of your order details, the terms and conditions provided by Springer, and the payment terms and conditions.

All payments must be made in full to CCC. For payment instructions, please see information listed at the bottom of this form.

License Number 3510891217793 & 3510890615927

License date Nov 16, 2014

Order Content Publisher Springer

Order Content

Publication Journal of Electronic Materials

Order Content Title Characterization of CdS Nanowires Self-Assembled in a Nanoporous Alumina Template

Order Content Author Shripriya Poduri

Order Content Date Jan 1, 2014

APPENDIX C (continued)

Volume number 43

Issue number 11

Type of Use Thesis/Dissertation

Portion Full text & Figures 1-6

Number of copies 1

Author of this Springer

article Yes and you are a contributor of the new work

Order reference number None

Original figure numbers Figures 1-6.

Title of your thesis /

dissertation CdS Nanowires and CdSe/ZnS Quantum Dots Properties and Applications

Expected completion

date Dec 2014

Estimated size(pages) 140

Total 0.00 USD

Terms and Conditions

Introduction

The publisher for this copyrighted material is Springer Science + Business Media. By clicking "accept" in connection with completing this licensing transaction, you agree that the following terms and conditions apply to this transaction (along with the Billing and Payment terms and conditions established by Copyright Clearance Center, Inc. ("CCC"),

APPENDIX C (continued)

at the time that you opened your Rightslink account and that are available at any time at http://myaccount.copyright.com).

Limited License

With reference to your request to reprint in your thesis material on which Springer Science and Business Media control the copyright, permission is granted, free of charge, for the use indicated in your enquiry.

Licenses are for one-time use only with a maximum distribution equal to the number that you identified in the licensing process.

This License includes use in an electronic form, provided its password protected or on the university's intranet or repository, including UMI (according to the definition at the Sherpa website: http://www.sherpa.ac.uk/romeo/). For any other electronic use, please contact Springer at (permissions.dordrecht@springer.com or

11/18/2014 RightsLink Printable License

https://s100.copyright.com/MyAccount/web/jsp/viewprintablelicensefrommyorders.jsp?ref=35b7bb20-3370-42d0-9124-a1b6522b60df&email= 2/3

permissions.heidelberg@springer.com).

The material can only be used for the purpose of defending your thesis limited to university-use only. If the thesis is going to be published, permission needs to be re-obtained (selecting "book/textbook" as the type of use).

Although Springer holds copyright to the material and is entitled to negotiate on rights, this license is only valid, subject to a courtesy information to the author (address is given with the article/chapter) and provided it concerns original material which does not carry

APPENDIX C (continued)

references to other sources (if material in question appears with credit to another source, authorization from that source is required as well).

Permission free of charge on this occasion does not prejudice any rights we might have to charge for reproduction of our copyrighted material in the future.

Altering/Modifying Material: Not Permitted

You may not alter or modify the material in any manner. Abbreviations, additions, deletions and/or any other alterations shall be made only with prior written authorization of the author(s) and/or Springer Science + Business Media. (Please contact Springer at (permissions.dordrecht@springer.com or permissions.heidelberg@springer.com)

Reservation of Rights

Springer Science + Business Media reserves all rights not specifically granted in the combination of (i) the license details provided by you and accepted in the course of this licensing transaction, (ii) these terms and conditions and (iii) CCC's

Billing and Payment terms and conditions.

Copyright Notice:Disclaimer

You must include the following copyright and permission notice in connection with any reproduction of the licensed material: "Springer and the original publisher /journal title, volume, year of publication, page, chapter/article title, name(s) of author(s), figure number(s), original copyright notice) is given to the publication in which the material was originally

published, by adding; with kind permission from Springer Science and Business Media"

Warranties: None

APPENDIX C (continued)

Example 1: Springer Science + Business Media makes no representations or warranties with respect to the licensed material.

Example 2: Springer Science + Business Media makes no representations or warranties with respect to the licensed material and adopts on its own behalf the limitations and disclaimers established by CCC on its behalf in its Billing and Payment terms and conditions for this licensing transaction.

Indemnity

You hereby indemnify and agree to hold harmless Springer Science + Business Media and CCC, and their respective officers, directors, employees and agents, from and against any and all claims arising out of your use of the licensed material other than as specifically authorized pursuant to this license.

No Transfer of License

This license is personal to you and may not be sublicensed, assigned, or transferred by you to any other person without Springer Science + Business Media's written permission.

No Amendment Except in Writing

This license may not be amended except in a writing signed by both parties (or, in the case of Springer Science + Business Media, by CCC on Springer Science + Business Media's behalf).

Objection to Contrary Terms

Springer Science + Business Media hereby objects to any terms contained in any purchase order, acknowledgment, check endorsement or other writing prepared by you, which terms are inconsistent with these terms and conditions or CCC's Billing and

APPENDIX C (continued)

Payment terms and conditions. These terms and conditions, together with CCC's Billing and Payment terms and conditions (which are incorporated herein), comprise the entire agreement between you and Springer Science + Business Media (and CCC) concerning this licensing transaction. In the event of any conflict between your obligations established by these terms and conditions and those established by CCC's Billing and Payment terms and conditions, these terms and conditions shall control.

Jurisdiction

All disputes that may arise in connection with this present License, or the breach thereof, shall be settled exclusively by arbitration, to be held in The Netherlands, in accordance with Dutch law, and to be conducted under the Rules of the 'Netherlands Arbitrage Instituut' (Netherlands Institute of Arbitration).*OR:* All disputes that may arise in connection with this present License, or the breach thereof, shall be settled exclusively by arbitration, to be held in the Federal Republic of Germany, in accordance with German law.

Other terms and conditions: v1.3

Questions? customercare@copyright.com or +1-855-239-3415 (toll free in the US) or +1-978-646-2777.

11/18/2014 RightsLink Printable License

https://s100.copyright.com/MyAccount/web/jsp/viewprintablelicensefrommyorders.jsp?ref=35b7bb20-3370-42d0-9124-a1b6522b60df&email= 3/3

Gratis licenses (referencing $0 in the Total field) are free. Please retain this printable license for your reference. No payment is required.

VITA

NAME	SHRIPRIYA PODURI
EDUCATION	PhD in Electrical and Computer Engineering, University of Illinois at Chicago, 2015
	MS in Electrical Engineering, University of Kentucky, 2010
	B.E. in Electronics Electrical and Communications, Panjab University, India, 2008.
EXPERIENCE	Research Assistant in Nanoengineering Laboratory, UIC 2010-2014
	Teaching Assistant in Electrical and Computer Engineering Department 2010-2014
	Research Assistant at Argonne National Laboratory, IL, USA. 2012-2014
	Graduate Technical Intern, Intel Corporation, Oregon May 2012-Aug 2012
	Research Assistant at Centre for Nanoscale Engineering, (CENSE) Laboratory, University of Kentucky 2008- 2010
	Research Intern, Central Scientific Instrumentation Organisation (CSIO), Microelectronics Division 2004-2008.
HONORS	Kentucky Graduate Scholarship Award 2008-2010.
PUBLICATIONS	**Shripriya Poduri**, Mitra Dutta, and M. Stroscio, "Characterization of CdS Nanowires Self-Assembled in a Nanoporous Alumina Template", *J Electron Mater.*, 43: 3979-3983, 2014.
	Shripriya Poduri, Mitra Dutta and M.Stroscio, "Growth and Characterization of CdS nanowires on ITO coated glass substrate", International conference of Materials Science and Materials Engineering 2014.

VITA (continued)

Shripriya Poduri, Mitra Dutta and M.Stroscio, “Polarization studies of Cadmium Sulphide (CdS) nanowires for polarization sensitive nanoscale devices” in preparation.

Shripriya Poduri, Mitra Dutta and M.Stroscio, “Analysis and computation of surface induced depletion region of CdS nanowires” in preparation.

Kimber L. Brenneman, **Shripriya Poduri**, Michael A. Stroscio, Fellow IEEE, and Mitra Dutta, Fellow IEEE,“ Optical Detection of Lead(II) Ions Using DNA-based Nanosensor” IEEE Sensor Journal, Issue 99 2013.

Mojgan Mazouchi, **Shripriya Poduri** and Mitra Dutta, “Growth and characterization of Indium Oxide, ZnO and CdS nanowires by vapor solid liquid growth technique” in preparation.

Ke Xu, Mohsen Purahmed, Kimber Brenneman, Xenia Meshik, **Shripriya Poduri**, Preeti Pratap, Michael Stroscio, and Mitra Dutta, “Design, Fabrication and Applications of Nanomaterial-based and Biomolecule-based Nanodevices and Nanosensors" in the Springer "Challenges and Advances in computational Chemistry and Physics”.

Mitra Dutta, Michael A. Stroscio, Jun Qian, Tsai-Chin Wu, Banani Sen, Nanzhu Zhang, Kimber Brenneman, **Shripriya Poduri**, Ke Xu, Xenia Meshik, and Pitamber Shukla " Fabrication of Nanosensors Based on DNA and RNA Aptamers and

VITA (continued)

Semiconductor Quantum Dots" Dekker Encyclopedia of Nanoscience and Nanotechnology.

Presentations:

Shripriya Poduri, Mitra Dutta and M.Stroscio, "Photoluminescence Characterization for CdS NWs for polarization devices", AAAS conference Science Journal Feb 2014.

Shripriya Poduri, Kimber Brenneman, M. Stroscio, Mitra Dutta, "Design of Lead of Optical nanobiosensor", Society of Women Engineers Conference 2011. Chicago, IL: Poster Presentation.

Shripriya Poduri, Kimber Brenneman, M. Stroscio, Mitra Dutta, "Design of Lead of Optical nanobiosensor", Society of Women Engineers Conference 2011. October 14, 2011. Chicago, IL: Poster Presentation.

Kimber L. Brenneman, **Shripriya Poduri,** Michael A. Stroscio, and Mitra Dutta, "Testing Water for Contaminants with a DNA-based Optical Nanosensor", Society of Women Engineers Conference 2012. November 9, 2012. Houston, TX: Session Presentation

Kimber L. Brenneman, Banani Sen, **Shripriya Poduri**, Michael A. Stroscio, and Mitra Dutta, "Aptamer-based optical detection of heavy metal ions as a platform for a portable handheld sensing device for environmental monitoring", Society of Women Engineers Conference 2011. October 14, 2011. Chicago, IL: Poster Presentation.